UNIVERSITY OF CALIFORNIA
SANTA CRUZ

MITIGATING STELLAR ACTIVITY IN RADIAL VELOCITY ANALYSES TO DETERMINE THE PHYSICAL PARAMETERS OF SIX EXOPLANET SYSTEMS

A dissertation submitted in partial satisfaction of the
requirements for the degree of

DOCTOR OF PHILOSOPHY

in

ASTRONOMY & ASTROPHYSICS

by

Molly Rose Kosiarek

June 2021

The Dissertation of Molly Rose Kosiarek
is approved:

Professor Jonathan Fortney, Chair

Professor Ian Crossfield

Professor Natalie Batalha

Quentin Williams
Interim Vice Provost and Dean of Graduate Studies

Table of Contents

List of Figures vi

List of Tables viii

Abstract ix

Dedication xi

Acknowledgments xii

I Introduction 1

1 Super-Earth and Sub-Neptune Compositions and Formation Theories 3

2 Atmospheric Characterization through Transmission Spectroscopy 7

3 Stellar Activity Influence 10

4 Dissertation Goals 13

II Methods 17

5 Radial Velocity Data Collection 19

6 Radial Velocity Analysis Method 21

7 Stellar Activity Mitigation using a Gaussian Process 23

III Stellar Activity in Solar Data 27

8 Solar Data as a Gaussian Process Test Case 29

8.1 Abstract . . . 29
8.2 Introduction . . . 30
8.3 Solar Datasets . . . 31
8.3.1 Initial Data Comparisons . . . 34
8.3.2 EMPIRE Data Periodicities . . . 37
8.4 Solar Temporal Variations using EMPIRE . . . 37
8.5 Direct Comparison of Photometry with Radial Velocity Data . . . 43
8.6 Conclusion . . . 47

IV Individual Planetary Systems 49

9 K2-291 51
9.1 Abstract . . . 51
9.2 Introduction . . . 52
9.3 K2 Light Curve Analysis . . . 53
9.4 Stellar Characterization . . . 55
9.4.1 Data Collection . . . 55
9.4.2 Stellar Parameters . . . 56
9.4.3 Stellar Activity Analysis . . . 59
9.5 Radial Velocity Analysis . . . 62
9.5.1 Keplerian Radial Velocity Fit . . . 62
9.5.2 Gaussian Process Inclusion and Training . . . 62
9.5.3 Gaussian Process Radial Velocity Fit . . . 63
9.6 Composition and Photoevaporation Discussion . . . 64
9.7 Conclusion . . . 69

10 GJ 3470 70
10.1 Abstract . . . 70
10.2 Introduction . . . 71
10.3 Radial Velocity Analysis . . . 73
10.3.1 Data Collection . . . 73
10.3.2 Stellar Activity Analysis . . . 73
10.3.3 Radial Velocity Fit . . . 77
10.4 Conclusion . . . 81

11 K2-3 82
11.1 Abstract . . . 82
11.2 Introduction . . . 83
11.3 Radial Velocity Analysis . . . 84
11.3.1 Data Collection . . . 84
11.3.2 Stellar Activity Analysis . . . 85
11.3.3 Radial Velocity Fit . . . 89
11.4 Transmission Spectra Discussion . . . 95

11.5 Conclusion 98

12 HD 97658 **100**
12.1 Introduction 100
12.2 Radial Velocity Analysis 101
12.2.1 Data Collection 101
12.2.2 Stellar Activity Analysis 102
12.2.3 Radial Velocity Fit 102
12.3 Conclusion 105

13 GJ 9827 **108**
13.1 Abstract 108
13.2 Introduction 109
13.3 Radial Velocity Analysis 110
13.3.1 Data Collection 110
13.3.2 Stellar Activity Analysis 111
13.3.3 Radial Velocity Fit 113
13.4 Composition Discussion 118
13.5 Conclusion 122

14 HD 106315 **124**
14.1 Abstract 124
14.2 Introduction 125
14.3 Radial Velocity Analysis 126
14.3.1 Data Collection 126
14.3.2 Stellar Activity Analysis 128
14.3.3 Radial Velocity Fit 130
14.4 Composition Discussion 134
14.5 Conclusion 138

V Discussion **139**

15 Bulk Composition **141**

16 Compositions across the Radius Valley **145**

17 Gaussian Processes in Literature Radial Velocity Analyses **154**

VI Conclusion **161**

18 Conclusions **163**

List of Figures

1.1 The radius valley as shown in Fulton et al. (2017). 5

4.1 Summary of exoplanet systems in this work. 15

8.1 HARPS-N solar radial velocity data. 32
8.2 SORCE total solar insolation data. 33
8.3 EMPIRE total solar insolation data. 34
8.4 Solar photometry and radial velocity data periodogram and autocorrelation comparisons. 36
8.5 Compilation of periodogram and autocorrelation peak locations from 70 years of EMPIRE data. 38
8.6 Example Gaussian process fit to one year of EMPIRE total solar irradiance data. 39
8.7 Gaussian process hyperparameter posteriors for individual fits of each year of EMPIRE photometry. 41
8.8 Gaussian process hyperparameter posteriors for SORCE photometry, HARPS-N RVs, HARPS-N FWHM, and HARPS-N BIS. 45

9.1 K2 light curve of K2-291. 54
9.2 Stellar activity periodicity in the K2-291 photometry. 60
9.3 Activity analysis for K2-291 from Calcium II H & K (S_{HK}) and radial velocity data. 61
9.4 Best-fit one-planet Keplerian orbital model for K2-291. 65

10.1 Photometry of GJ 3470 from the Fairborn Observatory. 75
10.2 Activity analysis for GJ 3470 from Calcium II H & K (S_{HK}) and radial velocity data. 76
10.3 Best-fit one-planet Keplerian orbital model for GJ 3470 including a Gaussian process. 80

11.1 Periodograms of the K2-3 radial velocity data and Calcium II H & K (S_{HK}). 86
11.2 Evryscope photometry of K2-3. 88

11.3 Best-fit three-planet Keplerian orbital model for K2-3 including a Gaussian process. 91
11.4 Phase-folded best-fit three-planet Keplerian orbital model for K2-3 including a Gaussian process. 92
11.5 Simulated transmission spectra for the K2-3 planets. 96

12.1 Time series photometry and radial velocity data for HD 97658. 103
12.2 Activity analysis for HD 97658 from Calcium II H & K (S_{HK}) and radial velocity data. 104
12.3 Best-fit one-planet Keplerian orbital model for HD 97658 including stellar activity. 106

13.1 Activity analysis for GJ 9827 from K2 photometry and HIRES radial velocity data. 112
13.2 Best-fit three-planet Keplerian orbital model for GJ 9827 including a Gaussian process. 115
13.3 H_2/He Composition Models for GJ 9827. 120
13.4 H_2O/$MgSiO_3$/Fe Ternary diagrams for GJ 9827 121

14.1 Activity analysis for HD 106315 from K2 photometry and HIRES radial velocity data. 129
14.2 Best-fit two-planet Keplerian orbit model for HD 106315. 132
14.3 H_2/He Composition Models for HD 106315. 136
14.4 H_2O/$MgSiO_3$/Fe Ternary diagrams for HD 106315 b. 137

15.1 Mass-radius diagram for small planets. 143

16.1 Stellar insolation versus radius for small planets orbiting FGK stars. . . 146
16.2 Radius valley as a function of stellar mass. 149
16.3 Stellar insolation versus radius for small planets orbiting mid K through early M stars. 151

17.1 Temperature histogram of literature systems using Gaussian processes. . 158

List of Tables

4.1 Planetary System Information 14

9.1 K2-291 Transit Derived Parameters 55
9.2 K2-291 Stellar Parameters 57
9.3 K2-291 Radial Velocity Fit Parameters 66

10.1 GJ 3470 Stellar and Planet b Transit Properties 72
10.2 Summary of C14 AIT Photometric Observations of GJ 3470 74
10.3 GJ 3470 Radial Velocity MCMC Priors and Posteriors 79

11.1 K2-3 Stellar Properties 83
11.2 K2-3 Radial Velocity MCMC Priors and Posteriors Part 1 93
11.3 K2-3 Radial Velocity MCMC Priors and Posteriors Part 2 94

12.1 HD 97658 Radial Velocity Parameters 107

13.1 GJ 9827 Stellar Parameters 111
13.2 GJ 9827 Radial Velocity Fit Parameters Part 1 116
13.3 GJ 9827 Radial Velocity Fit Parameters Part 2 117
13.4 GJ 9827 Planets' Potential Hydrogen/Helium and Water Mass Fraction Surrounding an Earth-like Core 118

14.1 HD 106315 Stellar Parameters 127
14.2 HD 106315 Radial Velocity Fit Parameters 131
14.3 HD 106315 Planets' Potential Hydrogen/Helium and Water Mass Fraction Surrounding an Earth-like Core 134

15.1 Summary of Planet Parameters 142
15.2 Summary of Stellar Parameters 142

17.1 Literature Radial Velocity Analyses with Gaussian Processes Part 1 . . 155
17.2 Literature Radial Velocity Analyses with Gaussian Processes Part 2 . . 156

Abstract

Mitigating Stellar Activity in Radial Velocity Analyses to Determine the Physical Parameters of Six Exoplanet Systems

by

Molly Rose Kosiarek

Large transit surveys have shown that small planets are abundant. The compositions of these planets are of particular interest as they span the transition between small rocky planets (super-Earths) and intermediate-sized planets with volatile envelopes (sub-Neptunes). The limiting factor on measuring small exoplanet masses to inform composition or atmospheric models is stellar activity. Gaussian processes are one such way to mitigate stellar activity and achieve precise planet masses.

In this dissertation, we find Gaussian processes are an effective way to model solar activity and determine the solar rotation period. Our concurrent solar photometry and radial velocity analyses produce consistent results; stellar photometry may assist radial velocity activity analyses. Subsequently, we perform radial velocity analyses on six exoplanet systems hosting eleven transiting planets: K2-291, GJ 3470, K2-3, HD 97658, GJ 9827, and HD 106315. We examine the stellar activity present and use a Gaussian process where relevant. With our measured masses, we comment on the potential compositions and compare these planets with other similar exoplanet systems. The eleven planets measured in this work are consistent with the theory that planets

smaller than the radius valley are primarily rocky and those larger than the radius valley contain a volatile envelope.

To my favorite cats:

Jacobi

Mordecai

Butterscotch

Acknowledgments

I would like to extend a heartfelt thank you to all who provided support over my PhD:

my primary advisor Professor Ian Crossfield

my UC Santa Cruz advisor Professor Jonathan Fortney

Professor Andrew Howard and the California Planet Search team

dissertation committee member Professor Natalie Batalha

fellow UC Santa Cruz graduate students

my extraordinary family

The text of this dissertation includes material from the following previously published material: Kosiarek et al. (2019a,b); Kosiarek and Crossfield (2020); Guo et al. (2020); Kosiarek et al. (2021). The author of this dissertation directed and performed this research which forms the basis for the dissertation.

Part I

Introduction

Chapter 1

Super-Earth and Sub-Neptune Compositions and Formation Theories

NASA's Kepler mission revolutionized the exoplanet field through detecting thousands of transiting exoplanets. One of the most surprising results from Kepler was the prevalence of planets between 1–4 $R_\oplus$ which are absent from our solar system (Howard et al., 2012; Fressin et al., 2013; Dressing and Charbonneau, 2015, 2013; Petigura et al., 2013). The compositions of these planets are of particular interest as they span the transition between small rocky planets (super-Earths) and intermediate-sized planets with volatile rich envelopes (sub-Neptunes).

Sub-Neptune and super-Earth planets have a wide range of potential structures and compositions. The planetary diversity seen in our own solar system is only a subset of what could be present in exoplanet systems. Through measurements of the mass and radius, one can derive a bulk density; however bulk density alone is degenerate with many

compositions. Therefore additional measurements, such as atmospheric characterisation through transmission or emission spectroscopy, is necessary to examine the composition of a particular planet (Figueira et al., 2009; Rogers and Seager, 2010).

Alternatively, large statistical samples can also shed light on planet composition and formation with only basic planet properties measured for the sample, eg: precise stellar parameters, planet orbital periods, and planet radii. Fulton et al. (2017) used such an analysis to show a paucity of planets between 1.5–2 $R_\oplus$ from a sample of Kepler F,G,K stars (Figure 1.1). This radius valley is consistent with previous photoevaporation model predictions (Owen and Wu, 2013; Lopez and Fortney, 2013; Owen and Wu, 2017) and ground-based radial velocity follow up observations (Weiss and Marcy, 2014; Rogers, 2015), which suggest a composition transition across the radius valley.

There are two main theories describing the creation of this radius valley: photoevaporation and core-powered mass-loss. Photoevaporation is a process where high energy photons from the star heat and ionize the hydrogen/helium envelope causing significant portions to escape. This process is most efficient for small planets inward of 0.1 AU within the first 100 Myr of the stars' lifetime (Owen and Wu, 2013). Photoevaporation models predict two key observed features in the Kepler sample of small planets, a lack of low density planets at low orbital periods and a bimodal radius distribution (Owen and Wu, 2013; Lopez and Fortney, 2013; Jin et al., 2014; Chen and Rogers, 2016; Owen and Wu, 2017). The bimodal distribution splits the population into two subgroups: planets around 1.3 $R_\oplus$ composed entirely of a rock/iron core, and planets around 2.6 $R_\oplus$ composed of a rock/iron core with a 0.5%–1% hydrogen/helium envelope. The envelopes

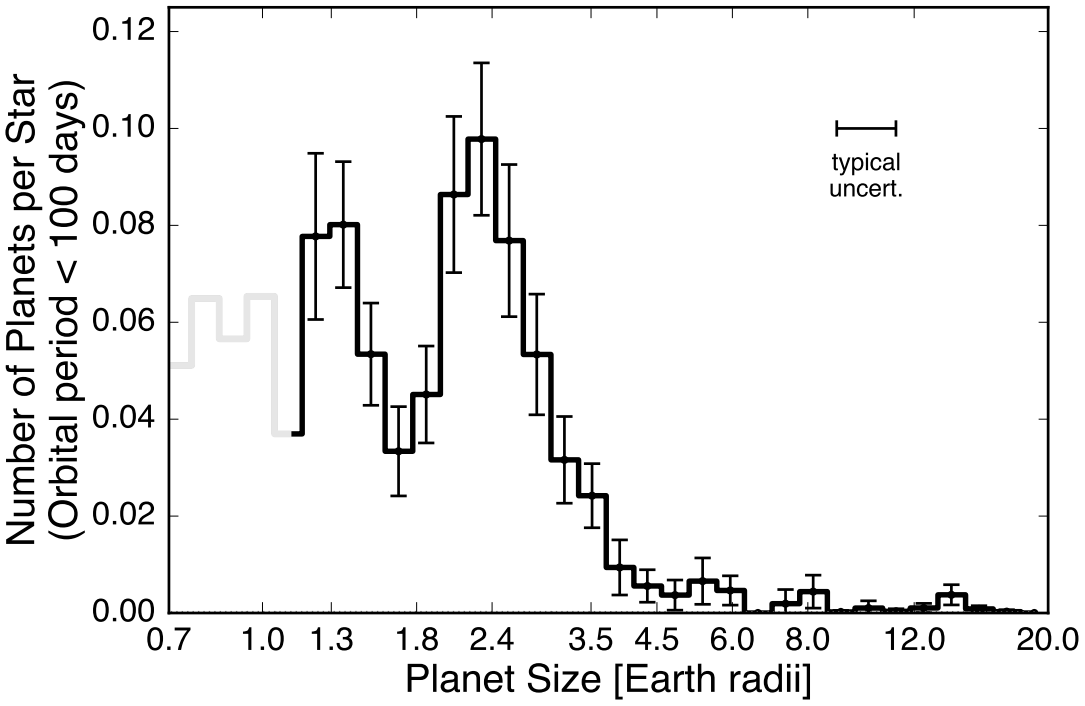

Figure 1.1: A histogram displaying the radius valley, reproduced from Fulton et al. (2017). The planet sample includes transiting Kepler planets with orbital periods shorter than 100 days; this sample has been corrected for completeness.

for the larger planets are retained because the atmospheric erosion timescale is longest for planets with a few percent hydrogen/helium which doubles the radius (Owen and Wu, 2017). Planets smaller than this are not massive enough to retain their envelope and therefore reduce down to their bare core radius around 1.3 $R_\oplus$. On the other hand, planets with more than 1% hydrogen/helium will rapidly increase in radius with small additions of hydrogen/helium; therefore, these larger planets should lose their upper envelope reducing their size down to around 2.6 $R_\oplus$.

The second theory, core-powered mass-loss, predicts that planets' heat of formation will be sufficient to cause atmospheric mass-loss and contraction (Ginzburg et al., 2018; Gupta and Schlichting, 2019, 2020). As the planetary cores form in the gas disk, heat is trapped within the planet. After the gas disk dissipates, the cooling of the planetary core causes atmospheric mass-loss and contraction. Through this process, planets either lose their entire atmospheres and become super-Earths or retain a moderate envelope as a sub-Neptune. There are two pairs of factors which control the outcome: the internal energy available vs. the atmospheric gravitational binding energy and the cooling timescale vs. the mass-loss timescale. Core-powered mass-loss models create a population of planets consistent with the observations shown in Fulton and Petigura (2018); Van Eylen et al. (2018); Martinez et al. (2019), including the relative occurrence of super-Earths and sub-Neptunes, the location of the radius valley, and the slope of the radius valley in radius-period space. It is not yet known whether photevaporation or core-powered mass-loss is the dominant mechanism. Alternatively, both may play an integral role in planet formation and evolution.

Chapter 2

Atmospheric Characterization through Transmission Spectroscopy

A robust understanding of planet compositions would enable the refinement of planet formation models. Individual atmospheric compositions can be measured through transit spectroscopy with ground-based high-resolution facilities (e.g. Birkby et al., 2013), the Hubble Space Telescope (HST; e.g. Charbonneau et al., 2002; Sing et al., 2016; Mikal-Evans et al., 2021), and soon the James Web Space Telescope (JWST; e.g. Greene et al., 2016). Thermal emission measurements also inform the understanding of planet atmospheres, however we concentrate on transmission spectroscopy throughout this work.

Preparatory measurements of potential atmospheric characterization targets are important for identifying the best targets as well as for the interpretation of the spectra. The target ephemerides must be refined in order to reduce the transit timing

uncertainty and therefore use space-based time most efficiently. Furthermore, precise mass measurements and surface gravity calculations are crucial for interpreting spectral features (Batalha et al., 2017a, 2019). The amplitude of features in a transmission spectrum depends on the planet's atmospheric scale height (H; Miller-Ricci et al., 2009);

$$H = \frac{k_B T_p}{\mu g_p}, \tag{2.1}$$

where k_B is the Boltzmann constant, T_p is the planet temperature, μ is the atmospheric mean molecular weight and g_p is the planet surface gravity. One key goal is to derive the mean molecular weight as it is a key diagnostic of atmospheric metallicity and chemistry (e.g. Benneke and Seager, 2013). The precision on the mean molecular weight (and thus on derived molecular abundances) is only as good as that on the surface gravity. The uncertainty on the surface gravity is dependent on the uncertainty on both mass and radius,

$$(\frac{\sigma_{g_p}}{g_p})^2 = (\frac{\sigma_{M_p}}{M_p})^2 + (\frac{\sigma_{R_p}}{R_p})^2. \tag{2.2}$$

The fractional precision on planetary radius is set by the precision on stellar radius and is typically $\sim$10%, therefore we must measure the planet mass to at least 20%. This 5σ requirement, arrived at by rough approximation, is confirmed Batalha et al. (2019) for small planets.

We can optimize the science yield of JWST by generating a sizable sample of well-studied atmospheric targets by the time of launch. An atmospheric study of a wide

variety of planets will shed light on the compositional diversity of super-Earths, the driving mechanisms responsible for the gap in the radius distribution, and the transition between rocky super-Earths and volatile-rich sub-Neptunes. Moreover, diversity is not limited to small planets; there is considerable spread in the mass-radius relation for Neptune to Jupiter-size planets driven by formation, evolution, and irradiation processes (Ning et al., 2018; Thorngren and Fortney, 2018). Evidence of planetary diversity comes largely from measurements of bulk properties like radius, mass, and average density. Atmospheric studies, however, offer an independent means of understanding the physical mechanisms driving the observed diversity.

The Kepler and K2 missions have discovered many cool planets orbiting bright stars amenable to atmospheric characterization through transmission spectroscopy (e.g. Crossfield et al., 2016; Montet et al., 2015; Vanderburg et al., 2016; Dressing et al., 2017; Mayo et al., 2018), and the Transiting Exoplanet Survey Satellite (TESS) is identifying systems that will make up a large sample of even brighter systems around nearby stars (Guerrero et al., 2021; Ricker et al., 2014; Sullivan et al., 2015) These bright host stars can be more precisely followed up from ground-based telescopes and are amenable to transmission spectroscopy observations. This work illustrates a follow-up program for potential JWST observations of multiple K2 systems containing small planets orbiting bright stars, much like those that are being discovered by TESS.

Chapter 3

Stellar Activity Influence

As described in Chapters 1 and 2, planet masses can inform other detailed planetary studies such as atmospheric characterization and formation scenarios. In many cases, planet masses are calculated through measuring stellar radial velocity data. Planets and stars orbit around their combined center-of-mass; therefore, orbiting planets can be detected and characterized by measuring the precise location of a star over time. The radial component of a star's orbital motion can be determined by precisely measuring the location of stellar spectral lines. Using this radial velocity method, one can derive the minimum mass of an orbiting planet. Fortunately, if the planet transits its host star, the orbital inclination can be measured from the transit curve and the mass of the planet can be calculated.

However, there are additional processes besides orbiting planets that can cause perceived radial velocity shifts in stellar spectral lines. Stars produce intrinsic radial velocity variations due to their internal and surface processes that can have amplitudes

comparable to planetary signals. The timescales of these radial velocity variations range from a few minutes or hours (pressure oscillations and granulation) to days or years (stellar rotation and large-scale magnetic cycle variations) (e.g. Schrijver and Zwaan, 2000).

Radial velocity instrument stability and calibration is rapidly approaching the ability to detect an Earth-like signal. For example, three high-precision spectrographs have recently reported sub-meter-per-second errors. NEID has an error budget of 27 cm s^{-1} (Halverson et al., 2016), ESPRESSO is achieving a 28 cm s^{-1} dispersion on sky over a single night (Pepe et al., 2014, 2019), and laser frequency comb measurements on EXPRES are showing an instrumental precision of <10 cm s^{-1} (Zhao and The EXPRES Team, 2019; Blackman et al., 2020; Petersburg et al., 2020). Yet there is much work needed to mitigate stellar activity to detect such a small signal on sky.

The HARPS-N team have been collecting disk-integrated radial velocity observations of our Sun over the last four years (Collier Cameron et al., 2019). After accounting for the radial velocity shifts from all of the solar system planets and thoroughly vetting for data quality, there remains an underlying solar variability signal of 5 m s^{-1} with a daily RMS scatter of <1 m s^{-1}. Stellar activity therefore remains the largest "noise" component in radial velocity analyses of the Sun, and will likely limit future surveys of Sun-like stars unless this noise can be mitigated.

Stellar activity associated with a star's rotation period can affect the analysis of orbiting planets or be mistaken as a planetary signal due to their overlapping timeframes of days to tens of days (e.g. Haywood et al., 2018; Robertson et al., 2014; Mortier

and Collier Cameron, 2017). Stellar surface processes cause variations in stellar line profiles and centroids (e.g. Vogt et al., 1987; Cegla et al., 2019); therefore monitoring stellar rotation with photometry may be a valuable tool for identifying and mitigating these stellar activity signals in radial velocity data. Previous works have found similar periodicities in photometry and radial velocity data and have used this correspondence to improve the precision of the planet parameters (e.g. Aigrain et al., 2012; Haywood et al., 2014; López-Morales et al., 2016; Kosiarek et al., 2019a).

Chapter 4

Dissertation Goals

In this dissertation, we aim to improve our ability to mitigate stellar noise through integrating photometry or activity indicators into the radial velocity analyses. Subsequently, we use this type of analysis to measure planet masses in six exoplanet systems. To do so, we first describe an investigation of using Gaussian processes in a radial velocity analysis using the Sun as a test case in Chapter 8. The text in this chapter is sourced from Kosiarek and Crossfield (2020).

In the following chapters, we describe radial velocity analyses of six exoplanet systems hosting eleven planets to measure the planets' masses or to improve upon previous measurements. The list of systems described in this thesis can be found in Table 4.1 and are shown in Figure 4.1. The text of these Chapters includes material from the following previously published papers: Kosiarek et al. (2019a,b); Kosiarek and Crossfield (2020); Guo et al. (2020); Kosiarek et al. (2021). In full, we include all sections (1-6) from Kosiarek et al. (2019a), sections 1, 2, 4-6 from Kosiarek et al. (2019b), all

sections (1-5) from Kosiarek and Crossfield (2020), section 4 from Guo et al. (2020), and sections 1, 3-7 from Kosiarek et al. (2021).

Name	Stellar Type	# Planets	Chapter	Source
Sun	G	8	8	Kosiarek and Crossfield (2020)
K2-291	G	1	9	Kosiarek et al. (2019a)
GJ 3470	M	1	10	Kosiarek et al. (2019b)
K2-3	M	3	11	Kosiarek et al. (2019b)
HD 97658	K	1	12	Guo et al. (2020)
GJ 9827	K	3	13	Kosiarek et al. (2021)
HD 106315	F	2	14	Kosiarek et al. (2021)

Table 4.1: Planetary System Information

The six exoplanet systems described in this work host eleven planets that span from 1–5 $R_\oplus$, with the majority of planets clustering around the radius valley (around 1.5–2 $R_\oplus$, Fulton et al., 2017). Measuring their masses and calculating their bulk densities has increased the sample size of small, well-characterized planets. A large sample of planets with measured masses and radii in this parameter space will be able to inform theoretical models on the creation and evolution of the radius valley, as discussed in Chapter 1. Additionally, six of the planets in this dissertation have been observed with HST in transmission (Tsiaras et al., 2018; Benneke et al., 2019; Kreidberg et al., 2020; Guo et al., 2020, Benneke et al. in prep; Hedges et al in prep) and many of these planets are also compelling targets for JWST. Measuring their masses makes future atmospheric characterization feasible and their atmospheric composition is valuable information for formation and evolution theories about small planets.

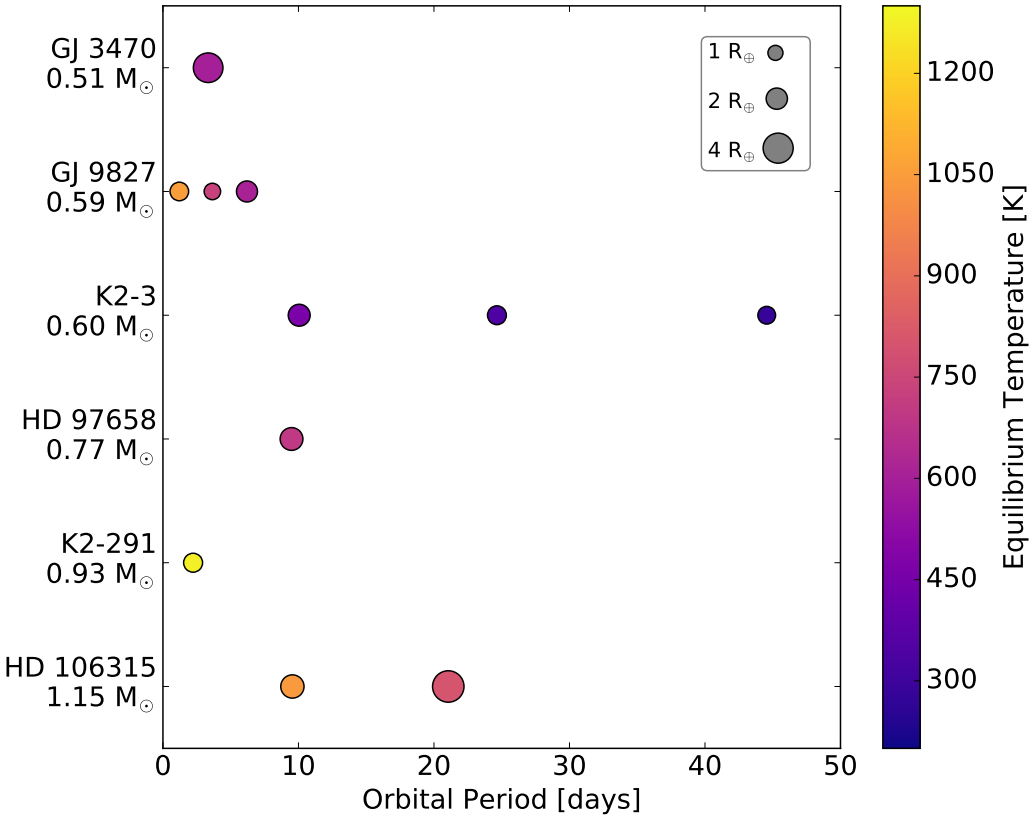

Figure 4.1: Summary of exoplanet systems in this work. Our six exoplanet systems are shown horizontally, ordered by stellar mass. Each individual planet is sized by radius and colored by equilibrium temperature.

Part II

Methods

Chapter 5

Radial Velocity Data Collection

We collected radial velocity data for each system described in this dissertation using a combination of the following four instruments: High Resolution Echelle Spectrometer (HIRES, Vogt et al., 1994) on the Keck I Telescope on Maunakea, the Levy Spectrograph on the Automated Planet Finder at Lick Observatory (APF, Radovan et al., 2014; Vogt et al., 2014), the High Accuracy Radial velocity Planet Searcher in the Northern hemisphere (HARPS-N, Cosentino et al., 2012) on the Telescopio Nazionale Galileo in La Palma and the Carnegie Planet Finder Spectrograph (PFS, Crane et al., 2006, 2008, 2010).

We additionally include literature radial velocity data from a combination of the following instruments: the High Accuracy Radial velocity Planet Searcher (HARPS, Mayor et al., 2003), the FIbrefed Echelle Spectrograph (FIES, Frandsen and Lindberg, 1999; Telting et al., 2014) at the Nordic Optical Telescope, HARPS-N, and PFS.

The HIRES exposures were taken through an iodine cell for wavelength calibra-

tion (Butler et al., 1996). The HIRES data collection, reduction, and analysis followed the California Planet Search method described in Howard et al. (2010). The HIRES data were then used to calculate updated stellar parameters for each system.

To determine the chromospheric activity measurement $\log(R'_{\rm HK})$, we followed the method described in Isaacson and Fischer (2010); we measured the flux in the Calcium H and K lines relative to the continuum. Small differences are noted as $S_{\rm HK}$ and are tracked to determine if the stellar activity is influencing the radial velocity data.

Chapter 6

Radial Velocity Analysis Method

We analyzed the radial velocity data for each system with `radvel`[1] (Fulton et al., 2018). `radvel` models Keplerian orbits and optional Gaussian processes to fit radial velocity data. The fit is performed through a maximum-likelihood function and errors are determined with an MCMC analysis. We use the default number of walkers, number of steps, and criteria for burn-in and convergence as described in Fulton et al. (2018).

We first model the radial velocity data as a combination of circular Keplerian orbits for all of the transiting planets; we include a Gaussian prior on the orbital period (P) and time of transit ($T_{\rm conj}$) from transit ephemerides measurements. The semi-amplitudes (K) reported from these analyses refer to the motion of the star induced by the orbiting planet. Afterwards, we test models including a trend ($\dot{\gamma}$), curvature ($\ddot{\gamma}$), and planet eccentricities (e, ω). The trend and curvature tests look for long term signals

[1] Available at `https://github.com/California-Planet-Search/radvel`

that have yet to undergo a full period within the time baseline, such as long-period giant planets or binary stars. We used the Bayesian information criterion (BIC) or Akaike information criterion corrected for small samples sizes (AIC) to evaluate if the fit improved sufficiently to justify the additional free parameters; a lower BIC or AIC indicates an improved fit.

Chapter 7

Stellar Activity Mitigation using a Gaussian Process

In some cases, Keplerian planet orbits and instrument noise are insufficient to describe radial velocity data variability due to the influence of stellar activity on the data. In this chapter we describe the origin of stellar activity in radial velocity data and the use of a Gaussian Process to mitigate the stellar activity.

Variability in the brightness and velocity fields across the stellar disk results in line shape variations and apparent radial velocity shifts. Stellar activity with timescales comparable to planet orbital periods is a particular problem for radial velocity analyses as these signals can appear as additional Keplerian signals or can affect the perceived amplitudes of the planet signals (e.g. Fulton et al., 2015; Robertson et al., 2013, 2015). Stellar activity from surface spots is especially problematic for M dwarfs, where the magnetic activity is not as well characterized as for solar-type stars and the stellar rotation

period is often similar to planet orbital periods at days to tens of days (McQuillan et al., 2013; Newton et al., 2016).

This stellar activity also causes absorption line variability (Cincunegui et al., 2007; Buccino et al., 2011; Gomes da Silva et al., 2012), which can be tracked in radial velocity data using certain stellar lines as activity indicators. The Calcium II H&K lines are often used for this purpose (S_{HK}, Isaacson and Fischer, 2010), whereas H-alpha may be more successful for cooler stars (Robertson et al., 2013, 2015; Newton et al., 2017). Another method is to use photometry to characterize the stellar activity and then subsequently fold the activity information into radial velocity fits (Haywood et al., 2014). For the Sun, we show that there is a connection between stellar activity information derived from photometry, activity indicators, and radial velocity data in chapter 8.

In this work, we investigate how stellar activity manifests in a combination of the following sources for each star: K2 photometry, ground based photometry, the Calcium II H&K stellar lines, H-alpha stellar lines, and our radial velocity data. The goal is to find whether there are strong periodicities in the supplemental data that match periodicities in the radial velocity data. Afterwards, if we find this evidence that the stellar activity is affecting the radial velocity data, we include an activity component in our fit through a Gaussian process.

Gaussian processes are a statistical technique for modeling correlated noise. Gaussian process regression enables the determination of physical parameter posterior distributions with uncertainties that reflect the confounding effects of stellar activity at specified timescales through a covariance matrix (e.g. Haywood et al., 2014; Grunblatt

et al., 2015; López-Morales et al., 2016). This allows us to use a Gaussian process to model stellar activity without parameterizing a specific function.

Stellar rotation activity signals are stochastic: they often match the timescale of planet orbital periods, are quasi periodic due to a combination of periodic stellar rotation and evolving active regions, and are characterized by some degree of smoothness since the active regions do not change instantaneously. These stellar signals should be well described by a Gaussian process with a periodic component for the stellar rotation, a component to allow for increasing and decreasing active regions, and a degree of smoothness (e.g. Angus et al., 2018). In some cases, radial velocity data are independently able to constrain both the stellar activity and planet parameters (Damasso and Del Sordo, 2017; Faria et al., 2016). However, radial velocity data are often too sparse to confidently determine the values of the hyper-parameters in addition to the planet parameters. To address this problem, authors in the literature use other data sources to constrain the values of the hyper-parameters, then incorporate this information into the radial velocity fit as priors on the hyper-parameters (e.g. Haywood et al., 2014; Rajpaul et al., 2015). In this work, we use either photometry or activity indicators to constrain the values of the hyper-parameters in our Gaussian process model. The choice of data is based on the strength of a coherent stellar activity signal, the time sampling, and the time separation from the radial velocity data.

We modeled the correlated noise introduced from the stellar activity using a quasi-periodic GP with a covariance kernel of the form

$$k(t,t') = \eta_1^2 \exp\left[-\frac{(\mathrm{t}-\mathrm{t}')^2}{\eta_2^2} - \frac{\sin^2(\frac{\pi(\mathrm{t}-\mathrm{t}')}{\eta_3})}{2\eta_4^2})\right], \tag{7.1}$$

where the hyper-parameter η_1 is the amplitude of the covariance function, η_2 is the active region evolutionary time scale, η_3 is the period of the correlated signal, and η_4 is the length scale of the periodic component.

This kernel allows for active region evolution through the decay term and a periodic component such as stellar rotation; therefore, it is a suitable kernel choice for fitting stellar activity (e.g. Haywood et al., 2014). We explore these hyperparameters by performing a maximum likelihood fit to the dataset exhibiting variation due to stellar activity (e.g. K2 light curve or S_{HK} data) with the quasi-periodic kernel (Equation 7.1), then determine the errors through an MCMC analysis.

We implement the Gaussian process fit using `radvel`. We first use a subset of this package to fit only a Gaussian Process to the activity data. Then we transfer the posteriors on η_2, η_3, and η_4 to our radial velocity model as priors on those same parameters and perform a fit including the Gaussian process to describe the stellar activity and Keplerian orbits to describe all of the known planets.

Part III

Stellar Activity in Solar Data

Chapter 8

Solar Data as a Gaussian Process Test Case

8.1 Abstract

Stellar activity remains a limiting factor in measuring precise planet parameters from radial velocity spectroscopy, not least in the search for Earth mass planets orbiting in the habitable zones of Sun-like stars. One approach to mitigate stellar activity is to use combined analyses of both radial velocity and time-series photometry. We present an analysis of simultaneous disk-integrated photometry and radial velocity data of the Sun in order to determine the useful limits of a combined analysis. We find that simple periodogram or autocorrelation analysis of solar photometry give the correct rotation period <50% of the time. We therefore use a Gaussian process to investigate the time variability of solar photometry and to directly compare simultaneous photometry with

radial velocity data. We find that the hyperparameter posteriors are relatively stable over 70 years of solar photometry and the amplitude tracks the solar cycle. We observe good agreement between the hyperparameter posteriors for the simultaneous photometry and radial velocity data. Our primary conclusion is a recommendation to include an additional prior in Gaussian process fits to constrain the evolutionary timescale to be greater than the recurrence timescale (ie., the rotation period) to recover more physically plausible and useful results. Our results indicate that such simultaneous monitoring may be a useful tool in enhancing the precision of radial velocity surveys.

8.2 Introduction

In this chapter, we explore the relationship between Gaussian process parameters derived from solar photometry to those derived from solar radial velocity data in order to better understand how photometry can be used for activity mitigation. We use the results to comment on the validity of using photometry to constrain the hyperparameter values in a Gaussian process radial velocity analysis. We describe the data used in this paper and look for common periodicities between the datasets in Section 8.3. We examine the time variability of solar photometry in Section 8.4, followed by a direct comparison between Gaussian process parameters derived from solar photometry and radial velocity data in Section 8.5 before concluding with advice for future observations in Section 8.6.

8.3 Solar Datasets

The Sun makes a particularly good test case due to the abundance and precision of solar monitoring. In this work, we examine 1) the time variability of solar photometry over 70 years of data and 2) the relationship between photometry and radial velocity data through comparing four years of simultaneous solar photometry and radial velocity data.

The HARPS-N team recently published a large solar radial velocity dataset taken with a solar telescope that feeds disk-integrated sunlight to the HARPS-N spectrograph (Collier Cameron et al., 2019). The radial velocity data span nearly four years, from July 2015 to March 2019 (Figure 8.1). Dozens of datapoints are taken per day, with 5 minute integrations, and result in a typical precision of 0.43 m s^{-1}. The HARPS-N data reduction package also produces two line measurements alongside the radial velocity data, the full-width half-maximum (FWHM) of the cross-correlation function (CCF) and a measurement of the asymmetry of the CCF called the bisector inverse slope (BIS). These two measurements can be used as stellar activity indicators, therefore we will compare them alongside the radial velocity data throughout our analysis.

The SOlar Radiation & Climate Experiment (SORCE) measures the total solar irradiance (TSI) with the total irradiance monitor (Lawrence et al., 2000). The TSI dataproducts[1] include daily and 6-hour average irradiances normalized to a distance of 1 AU and the data have a typical precision of 0.5 W m^{-2} (Figure 8.2).

The EMPirical Irradiance REconstruction (EMPIRE) is a solar irradiance

[1] `http://lasp.colorado.edu/home/sorce/data/tsi-data/`

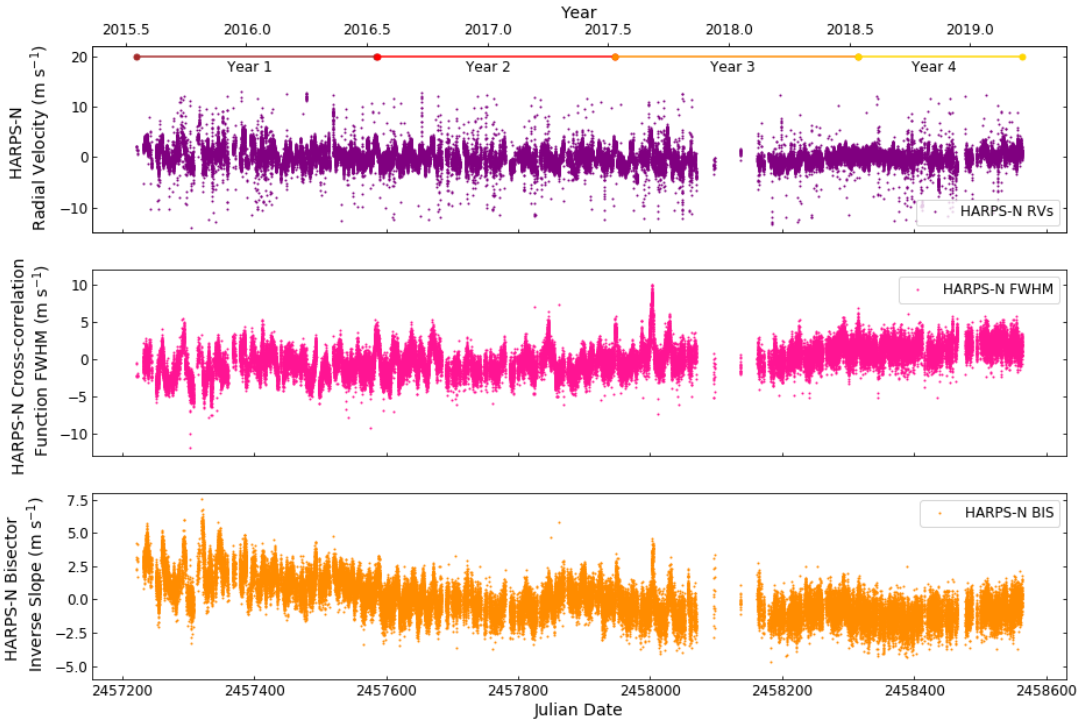

Figure 8.1: HARPS-N solar radial velocity data (top, purple) corrected for barycentric motion and with all solar system planets removed, HARPS-N full-width half-maxiumum of the cross-correlation function (middle, pink), and the bisector inverse slope (bottom, orange); the data are from Collier Cameron et al. (2019). The four years of HARPS-N data are labeled at the top.

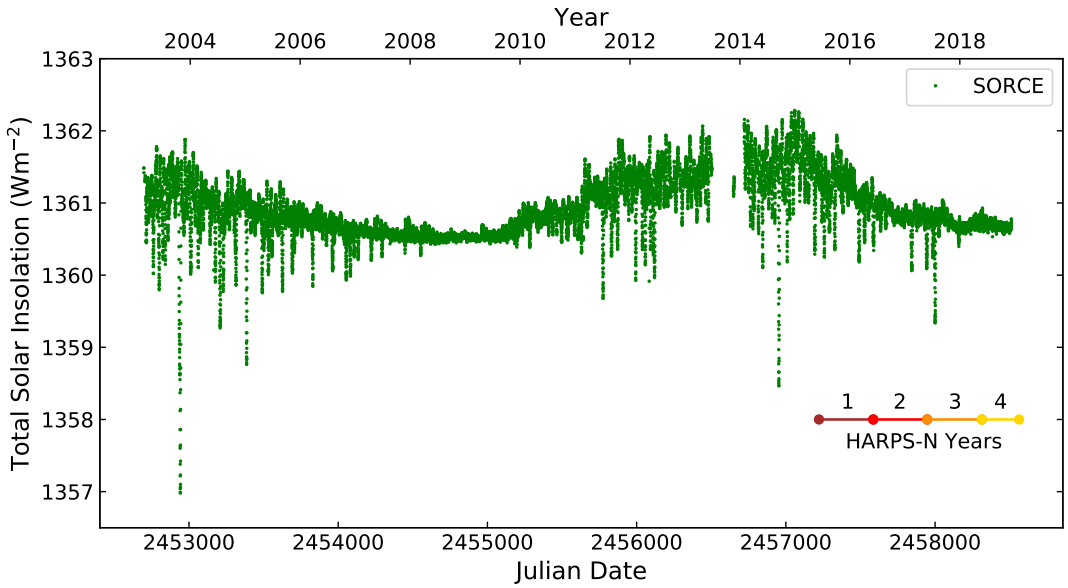

Figure 8.2: SORCE total solar insolation data from February 2003 to August 2019. The four years of data that overlap with the HARPS-N dataset are labeled.

model with the goal of providing uninterrupted and coherent TSI time series for climate modeling (Yeo et al., 2017). The solar irradiance is calculated by a linear combination of solar activity indices connected to sunspots and faculae. The dataset begins February 1947 and extends to September 2016 (Figure 8.3). EMPIRE overlaps with the SORCE dataset from 2003-2016 with good agreement (RMS difference of 0.12 Wm^{-2}). Therefore, this work will use the EMPIRE dataset when discussing variations over time due to its much longer baseline and the SORCE dataset when comparing with the HARPS-N radial velocity data due to the overlap between these two datasets.

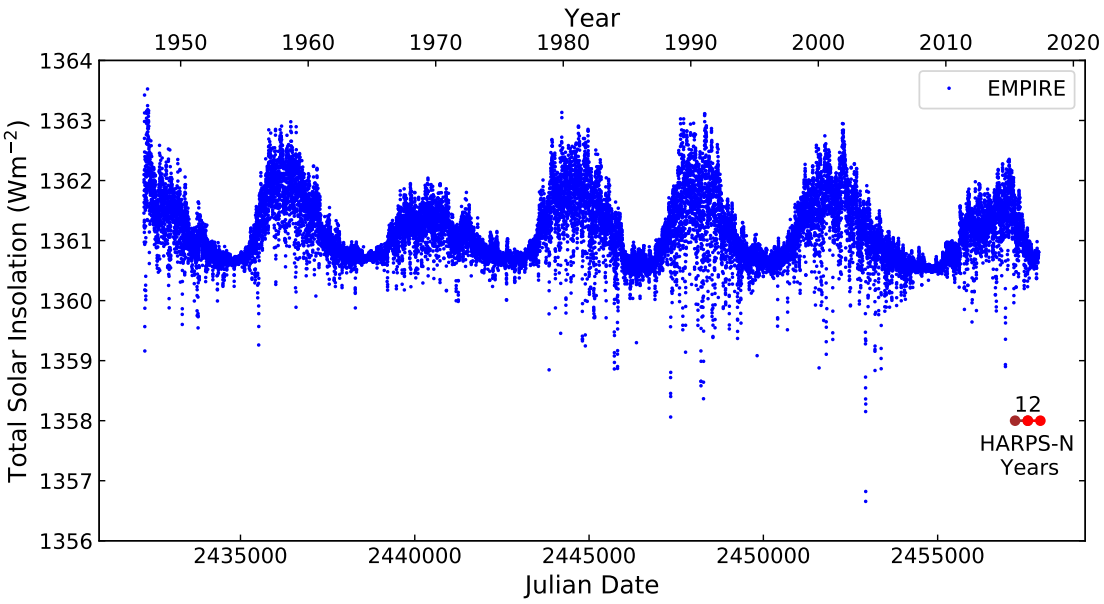

Figure 8.3: EMPIRE total solar insolation data from February 1947 to September 2016. The two years of data that overlap with the HARPS-N dataset are labeled.

8.3.1 Initial Data Comparisons

To directly compare the EMPIRE and SORCE photometry with the HARPS-N radial velocity data, we first split each of the datasets into year-long segments that overlap with the timescale of the HARPS-N data. These segments are labeled "Year 1–4" in Figures 8.1–8.3.

The three datasets used in this project have different sampling cadences and distribution. To normalize the inputs for each fit, we binned the datapoints in daily bins with uncertainties that represent the standard deviation of the points. This binning was also performed to focus on the solar rotation timescale, as opposed to short timescale activity such as pressure oscillations and granulation. Binning on a daily cadence is also standard practice in many precise radial velocity analyses (e.g. Dumusque et al., 2011;

Chaplin et al., 2019).

We initially looked for common periodicities in the datasets using two different techniques, a Lomb-Scargle periodogram and autocorrelation. The Lomb-Scargle periodogram results are shown in Figure 8.4. The majority of the peaks occur at the solar rotation period or at its harmonics. In all four years, the HARPS-N RV data have peaks at the stellar rotation period (27 days) and the 1/2 and 1/3 harmonic. In two years, Year 1 and Year 4, the peak at 1/2 of the rotation period is the highest and the peak at the rotation period is the second highest. The HARPS-N FWHM and BIS data primarily follow the radial velocity data, except for Year 4 which has few significant peaks. For the photometry, the majority of the peaks occur at the stellar rotation period or its harmonics, however the peaks are less consistent than the HARPS-N RV data.

Due to the stochastic nature of stellar activity, the highest peak in a periodogram is often not at the stellar rotation period (Boisse et al., 2011; Nava et al., 2019), therefore we also examine autocorrelation plots for all of our datasets. We first linearly interpolate the HARPS-N data to a uniform daily cadence to perform the autocorrelation using numpy.interp and numpy.correlate in Python. The autocorrelation for the photometry and radial velocity data over Years 1-4 are shown in Figure 8.4. The HARPS-N RV autocorrelation has a distinct "sawtooth" pattern in Years 1, 2, and 4, with peaks at the stellar rotation period and multiples thereof. Year 3 has a break in the middle of the dataset that likely creates the broad peak at 125 days and partially washes out the stellar rotation signal. The FWHM and BIS also peak at the solar rotation period and its harmonics in Years 1–3; there are no significant peaks in Year 4. The photometry

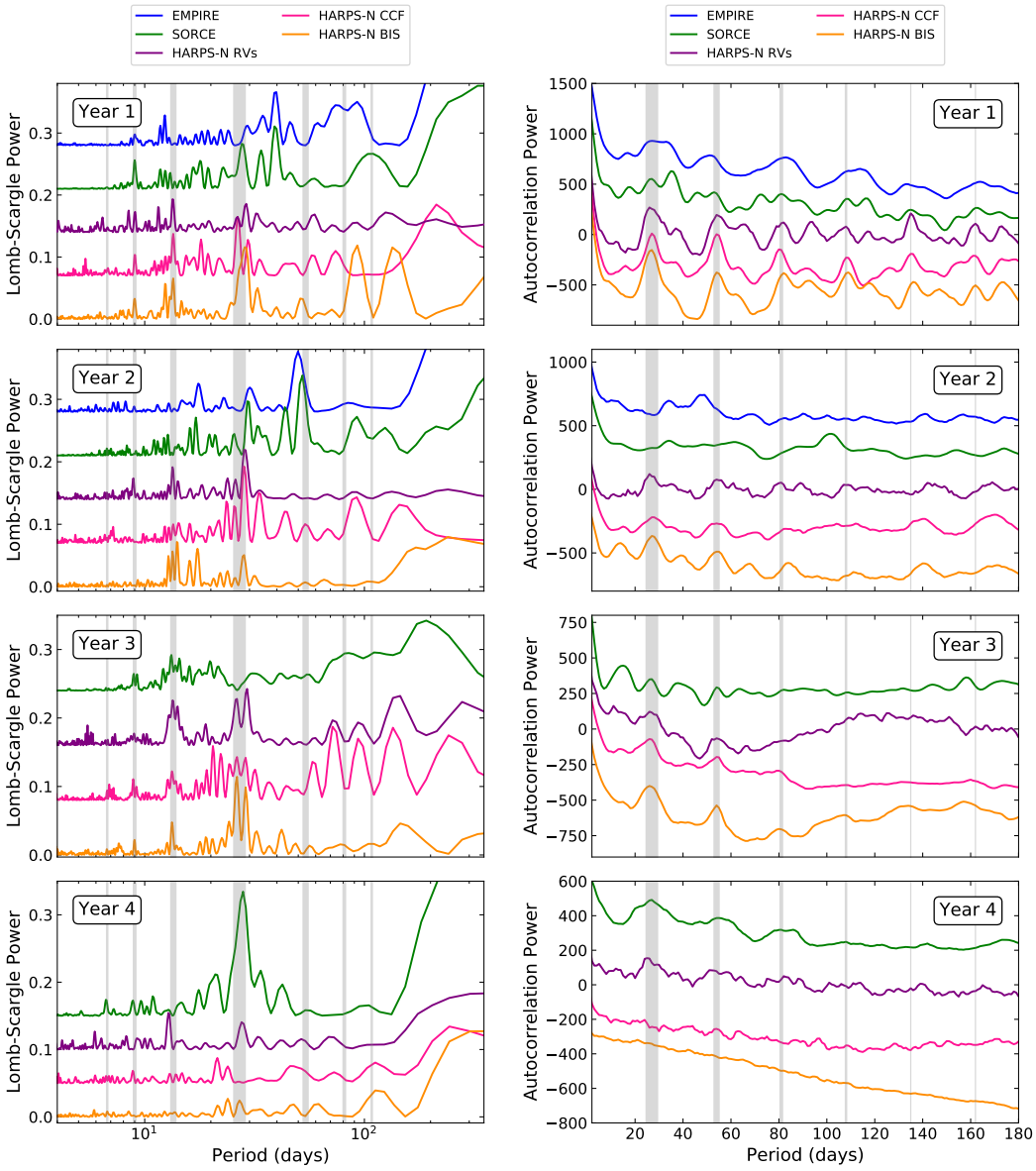

(a) Periodogram (b) Autocorrelation

Figure 8.4: Periodogram and autocorrelation comparisons of the solar photometry and radial velocity data. All datasets are plotted with individual y-offsets for clarity. The stellar rotation period (27d, thick grey line) and its harmonics (thin grey lines) are plotted for comparison. We find that many of the peaks line up with the solar rotation period and its harmonics.

follows the same "sawtooth" pattern in Years 1 and 4. Years 2 and 3 have larger variance in the amplitude of the total solar insolation which may contribute to the inconsistent peaks. In summary, there is good agreement between the SORCE, EMPIRE, and RV data for Years 1 and 4, and good agreement between the RV, FWHM, and BIS data for Years 1–3.

8.3.2 EMPIRE Data Periodicities

To further examine the accuracy of peridogram and autocorrelation analyses we perform both on each year of the 70 yr EMPIRE dataset. We record the highest three peaks in the periodogram and autocorrelation plots for each year to determine how often the top three peaks are consistent with the solar rotation period, shown as a histogram in Figure 8.5. In a periodogram, the solar rotation periods is consistent with the highest peak 14.3% of the time and one of the highest three peaks 48.6% of the time. For the autocorrelation, the rotation period is consistent with the highest peak 21.4% of the time and one of the highest three peaks 44.3% of the time. As the highest peaks are often at values unrelated to the solar rotation period, one should exercise caution when using either of these methods to determine a stellar rotation period.

8.4 Solar Temporal Variations using EMPIRE

To examine the time variation of the solar insolation and its GP hyperparameters, we perform a Gaussian process fit using a quasi-periodic kernel (Equation 7.1) on each year of data separately. An example fit for one year of EMPIRE data is shown in

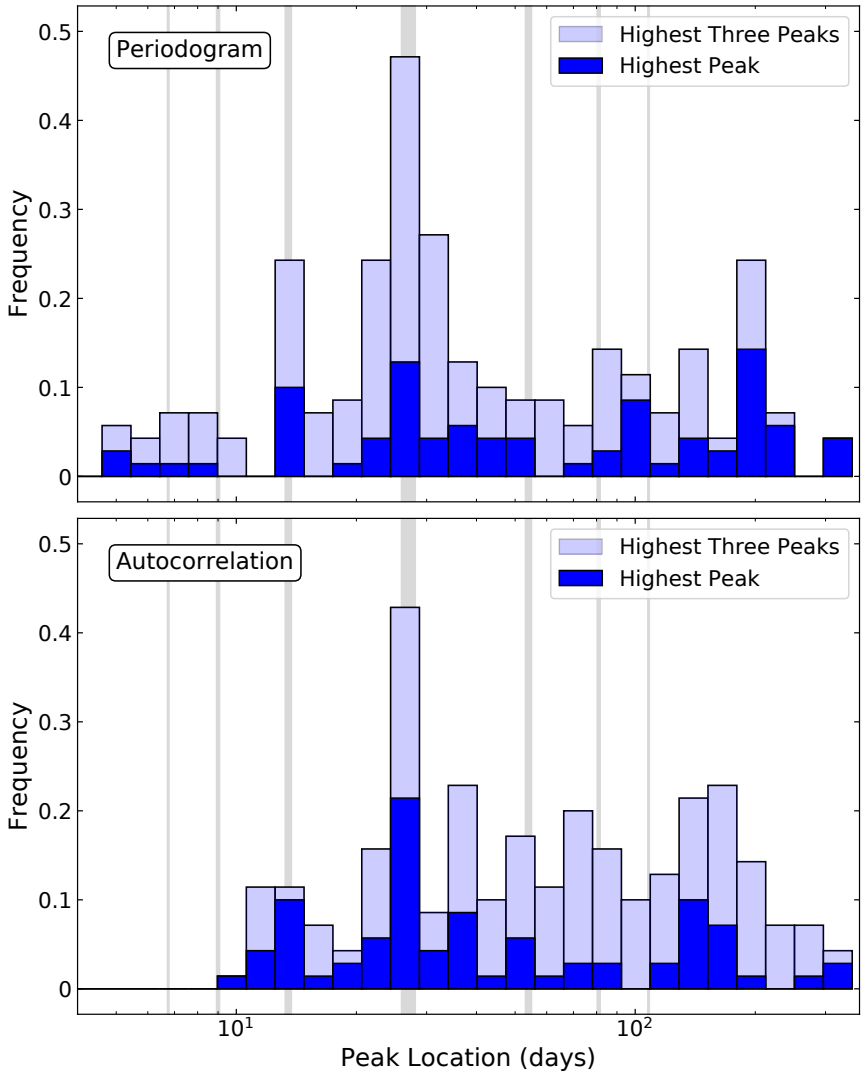

Figure 8.5: Histograms showing the location of the highest (dark blue) and highest three (light blue) peaks in a periodogram (top) and autocorrelation (bottom) analysis of the 70 years of EMPIRE data. The stellar rotation period (27d, thick greyline) and its harmonics (thin grey lines) are plotted for comparison. Both histograms show a plurality of peaks at the solar rotation period; however, one should exercise caution when using either of these methods to determine a stellar rotation period as there are a significant number of peaks unrelated to the solar rotation period.

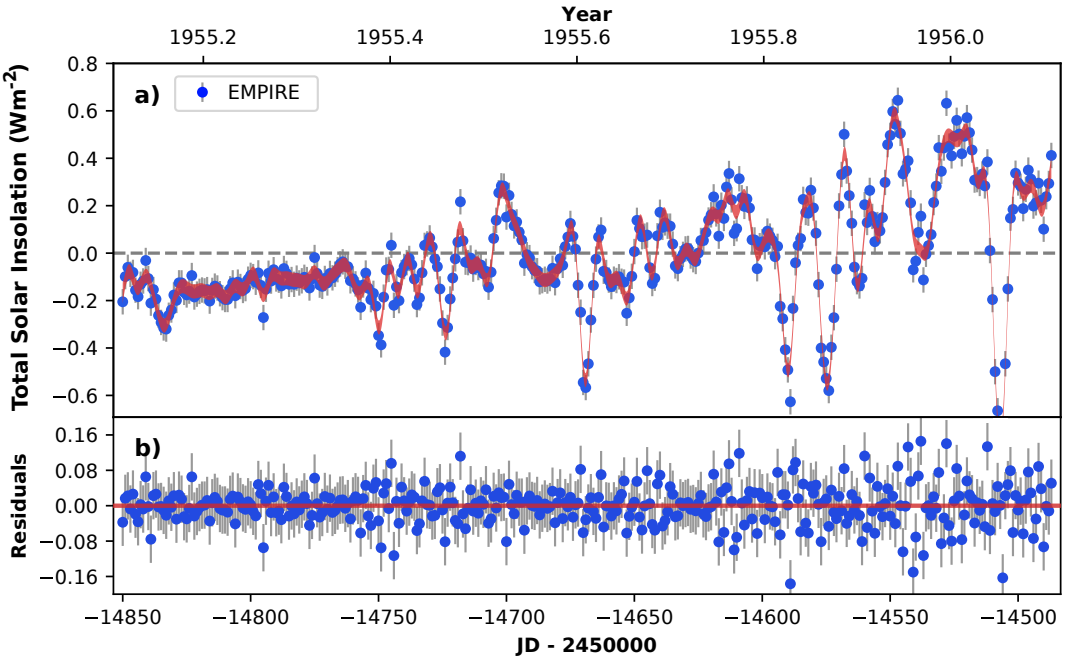

Figure 8.6: Example Gaussian process fit (red line) to one year of EMPIRE total solar irradiance data (blue points). The top panel shows the mean-subtracted data and the bottom panel shows the residuals. A Gaussian process with a quasi-periodic kernel well describes this year of solar photometry.

Figure 8.6. A year was chosen as the timescale so that sufficient rotation periods would occur in each group to accurately determine the parameters from the Gaussian process fit while still being short enough to be a plausible baseline for stellar photometry observations. We acknowledge one of the limitations with this method is we are monitoring discrete changes in the hyperparameters instead of a continuous change.

We perform two fits for each year. The first fit has the following four priors. A non-informative prior is used on the amplitude (uniform prior of $0.01< \eta_1 <10$). As the data is sampled daily, small values for the evolutionary timescale allow the model to artificially change quickly enough to intersect all of the datapoints. Therefore, we limit the values of the evolutionary timescale on the lower end to avoid overfitting and the higher end as the model would be unable to detect a timescale longer than the data baseline (uniform prior of $5\text{d}< \eta_2 <365\text{d}$). For the recurrence timescale, we also limit the lower end to prevent overfitting and upper end at the baseline (uniform prior of $5\text{d}< \eta_3 <365\text{d}$). For other stars, the recurrence timescale can be constrained by a $vsin(i)$ measurement as short rotation periods produce large amplitudes or through determining the stellar rotation period through other methods. Lastly, we constrain the length scale of the periodic component (Gaussian prior of η_4=0.5$\pm$0.05). The length scale is related to the average number of minima in a sample drawn from the Gaussian Process prior. An η_4 value of 0.5 means that there are on average two to three minima. Jeffers and Keller (2009) finds that a random distribution of several active regions on the surface of a star produces two minima in the light curve, resulting in the Gaussian prior around 0.5 used in previous Gaussian process fits (e.g. Haywood et al., 2014; López-Morales

et al., 2016).

The posteriors of the four hyperparameters from 1947 to 2016 are shown in Figure 8.7. The amplitude shows a clear 11 year variation matching the 11 year solar magnetic activity cycle. The variations also correlate well with the number of sunspots and inversely with the cosmic ray flux (Usoskin, 2013).

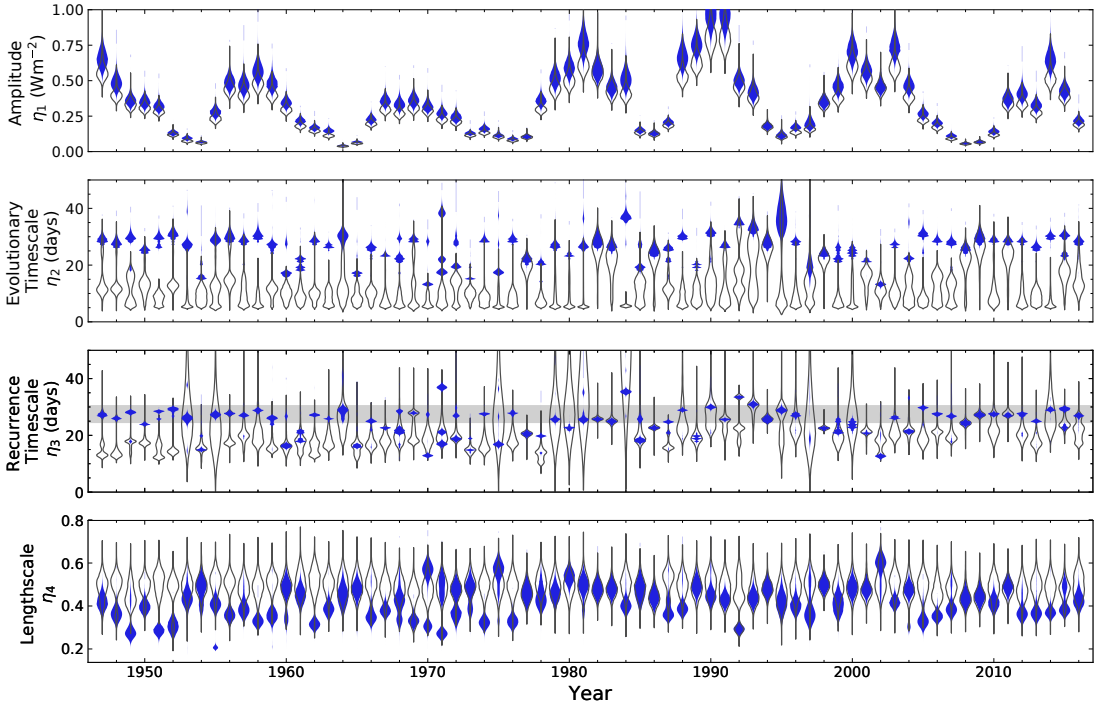

Figure 8.7: Gaussian process hyperparameter posteriors for individual fits of each year of EMPIRE photometry, with (blue shaded) and without (black outline) a prior restricting the evolutionary timescale to be larger than the recurrence timescale. This added prior results in a good match between the solar rotation period (shaded grey bar) and the recurrence timescale posterior.

The evolutionary timescale and recurrence timescale are interrelated. In years with an inferred low evolutionary timescale, the recurrence timescale is fairly uncon-

strained as the model is able to well-fit the data without a strong periodic component. The recurrence timescale describes the periodic component of the photometry and therefore should relate to the solar rotation period. The recurrence timescale posterior is well constrained at the solar rotation period for only a few years (1982, 1983, 1986, 1994, 2008, 2009, and 2011). These years all have something in common: the evolutionary timescale is longer than the recurrence timescale. For the majority of the other years, the inferred evolutionary timescale is shorter than the inferred rotation period. From this, it appears that the model is only successful in determining the rotation period if the evolutionary timescale is longer than the recurrence timescale.

On the Sun, sunspot lifetime is proportional to the spot area (Gnevyshev, 1938; Waldmeier, 1955). Measured sunspot lifetimes range from a few days (Petrovay and van Driel-Gesztelyi, 1997) to hundreds of days (Henwood et al., 2010). However, the evolutionary timescale is not describing individual spot lifetimes but instead the evolution of large active regions. Measured lifetimes of solar active regions ranges from hours to months (Schrijver and Zwaan, 2000; van Driel-Gesztelyi and Green, 2015); the lifetime is roughly proportional to the active region's peak magnetic flux and can depend on the phase of the solar magnetic cycle and strength of surrounding magnetic fields. Large active regions last from weeks to months, many of which have a longer lifetime than the solar rotation period, providing physical justification for a prior restricting the evolutionary timescale to be longer than the recurrence timescale.

Furthermore, the timescales of active region evolution were estimated for 35 main sequence FGK stars through S-index measurements at Mount Willson Observatory

(Donahue et al., 1997). The estimated lifetimes of these active regions ranged from 75 to 3000 days and the stellar rotation period ranged from 5 to 200 days with an average near 50 days. All of these stars have longer active region evolution timescales than their measured rotation periods, suggesting that this relationship holds for other FGK dwarf stars.

This relationship motivates our second fit where we include an additional prior to constrain the evolutionary timescale to be larger than the recurrence timescale ($\eta_2 > \eta_3$). With this additional prior, the recurrence timescale is consistent with the solar rotation period to 1σ for 48 of the 70 years. In addition, many of the previously multi-modal posteriors are now single peaks and the long tail posteriors are better constrained. If one is using a Gaussian process to determine a stellar rotation period, we recommend including this prior. The amplitude shows a small systematic increase with the additional prior; the trend with the solar magnetic cycle remains strong. The structure parameter has a greater variation between the years and has a lower average (approximately 0.4), favoring more high-frequency structure in the lightcurves.

8.5 Direct Comparison of Photometry with Radial Velocity Data

Radial velocity data is often sparsely sampled and therefore poorly constrains the Gaussian process hyperparameters without additional information. In previous works, active stellar lines and photometry have been used to provide stellar activity

information for the radial velocity fit (e.g. Aigrain et al., 2012; Haywood et al., 2014). A key assumption in these analyses is that stellar activity is recorded in the same way between the two data types; however, for stars with low magnetic activity the radial velocity data may be dominated by phenomena not observable from a lightcurve (Wright, 2005; Tayar et al., 2019). The overlap between the SORCE photometry dataset with the well-sampled HARPS-N radial velocity dataset provides an unique opportunity to test this assumption for sun-like stars.

The same procedure described above for the EMPIRE analysis (section 8.4) is performed here, and the results are shown in Figure 8.8. To recap, two fits are run for each dataset; the first (posteriors shown as a black outline) with the following two uniform priors: 5d$< \eta_2 <$365d, 5d$< \eta_3 <$365d and one Gaussian prior: η_4=0.5$\pm$0.05. The second (posteriors shown as a solid color interior) has an additional prior constraining the decay timescale to be larger than the recurrence timescale ($\eta_2 > \eta_3$).

The main takeaway from these fits is that the posteriors are largely consistent between all datasets in the Gaussian process fit with the additional prior ($\eta_2 > \eta_3$); therefore, photometry can provide valuable information about stellar activity for radial velocity analyses. In both fits, the amplitude posteriors are largely consistent within each dataset with a slight downward trend as the data approaches the solar minimum.

There are two interesting comparisons from the initial fit without the additional prior. First, the SORCE photometry and HARPS-N RVs have consistent posteriors that match the solar rotation period only in Year 4 where the SORCE data has a longer evolutionary timescale than recurrence timescale. Second, the FWHM and BIS show

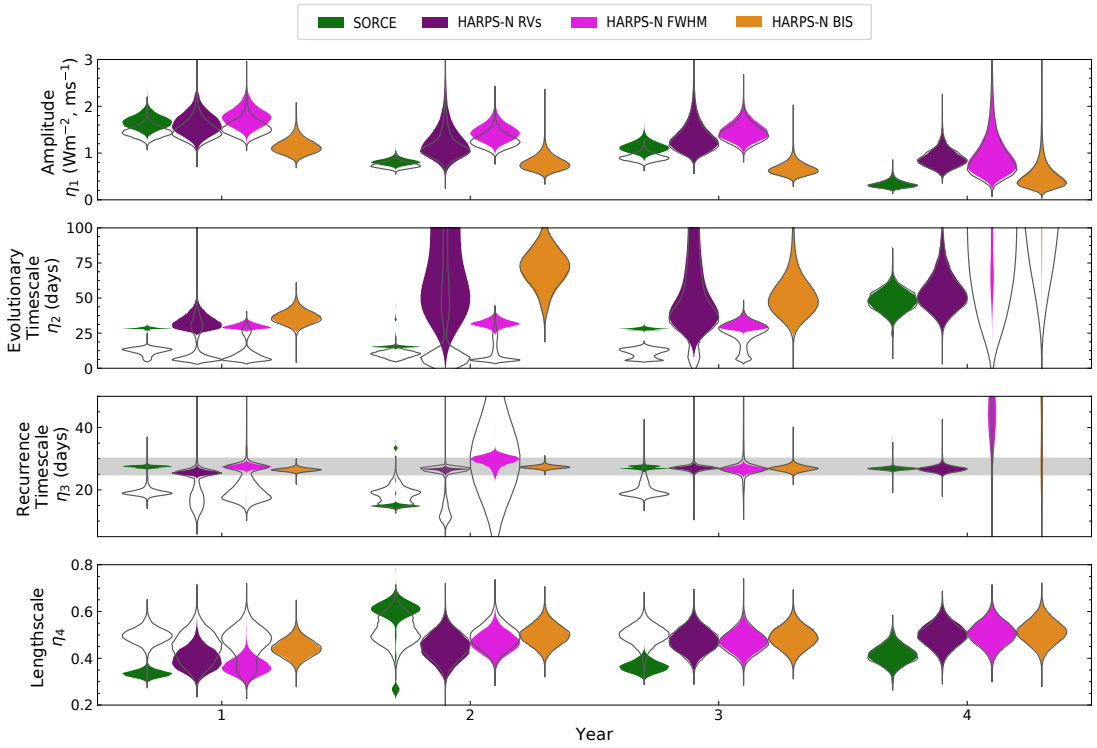

Figure 8.8: Gaussian process hyperparameters for SORCE photometry, HARPS-N RVs, HARPS-N FWHM, and HARPS-N BIS for two fits, one with (shaded) and without (black outline) an additional prior constraining the evolutionary timescale to be longer than the recurrence timescale. The SORCE, FWHM, and BIS amplitudes have been scaled up by factors of 5, 1000, and 1000 respectively to be visible. The recurrence timescales are largely consistent with the solar rotation period (shaded grey bar). The evolutionary timescale, recurrence timescale, and lengthscale posteriors are consistent between the four datasets for most years; therefore, photometry can provide valuable information about stellar activity through constraining these parameters for a radial velocity fit.

opposite results to the photometry. The FWHM data well matches the RVs for Year 1-3 and not Year 4. The BIS posteriors for Year 1-3 are consistent with the solar rotation period and has a longer evolutionary timescale than recurrence timescale.

The posteriors of the second analysis display much higher agreement between the different datasets. The SORCE photometry and HARPS-N RVs are consistent for three of the four years; the inconsistent year, Year 2, SORCE instead has a recurrence timescale of half of the solar rotation period. The RVs and FWHM posteriors are now both well constrained and the recurrence timescale matches the solar rotation for Years 1-3. The BIS remains unchanged for Years 1-3 as the evolutionary timescale was already longer than the recurrence timescale and the recurrence timescale matched the solar rotation period. Lastly, η_4 may be underconstrained in the three HARPS-N datasets as the posteriors closely resemble the Gaussian prior on η_4. The lengthscale parameter for the SORCE photometry is around 0.4, lower than the lengthscale parameter for the three HARPS-N datasets, consistent with the lengthscales found in the EMPIRE analysis (section 8.4).

Year 4 is distinct as the FWHM and BIS do not have well constrained posteriors and do not match the photometry or RVs. Additionally, Year 4 is near the solar minimum and is the one year that the SORCE photometry matched the HARPS-N RVs without the additional prior; perhaps solar activity displays different characteristics in line measurements compared to photometry throughout the solar cycle. Further high-cadence radial velocity monitoring of the sun will be important to confirm many of the observations from this paper and potentially detect changes as a function of the solar cycle.

8.6 Conclusion

We analysed simultaneous disk-integrated photometry and radial velocity data of the Sun in order to determine the useful limits of a combined analysis. We examined the periodicities of five simultaneous datasets, SORCE and EMPIRE photometry, HARPS-N radial velocity, and two HARPS-N line indicators: FWHM and BIS. The periodograms and autocorrelation plots often displayed power at the stellar rotation period and its harmonics; however, the stellar rotation period was not always the highest peak. In the 70 year EMPIRE dataset, the highest peak matched the solar rotation period 14.3% and 21.4% of the time for our periodogram and autocorrelation analysis respectively. We recommend exercising caution when using either of these methods to determine a stellar rotation period due to the large number of peaks at times unrelated to the solar rotation period.

A Gaussian process analysis of photometry can provide more reliable estimates of a star's rotation period. We used a Gaussian process to investigate the time variability of solar photometry through analysing 70 years of EMPIRE data. The time variability analysis determined that the Gaussian process amplitude hyperparameter followed the eleven year solar magnetic cycle. The evolutionary timescale and recurrence timescales remained relatively stable throughout and the recurrence timescale matched the solar rotation period when the additional prior constraining the evolutionary timescale to be greater than the recurrence timescale was included. Therefore, this Gaussian process analysis identified the correct solar rotation period more often than either the periodogram

or autocorrelation analyses.

Photometry can also be a valuable tool for understanding stellar activity in radial velocity data fits. In our direct comparisons between the Gaussian process hyperparameters of the SORCE photometry, HARPS-N RV data, and HARPS-N FWHM and BIS line measurements, the evolutionary timescale and recurrence timescale were consistent between the datasets after including the same additional prior restricting the evolutionary timescale to be longer than the recurrence timescale. We recommend including this additional prior to improve the agreement between Gaussian Process hyperparameters derived from photometry and radial velocity data. The lengthscale parameter was consistent between the four datasets, although the value for the photometry data was systematically low compared to the other three.

Precision Radial Velocity surveys are aiming to characterize Earth-like planets around Solar-type stars with cm s^{-1} radial velocity signals. Gaussian processes informed from well-sampled photometry or activity indicators may enable sufficient stellar activity mitigation to detect these small signals. Overlapping data spanning a full solar cycle or a few solar cycles is necessary to confirm the findings in this paper and to look for evidence for changes as a function of the solar cycle. Further work is also needed to determine how these conclusions could be applied to other stellar types.

Part IV

Individual Planetary Systems

Chapter 9

K2-291

9.1 Abstract

K2-291 is a solar-type star with a radius of $R_* = 0.899 \pm 0.034$ $R_\odot$ and mass of $M_* = 0.934 \pm 0.038$ $M_\odot$. From K2 C13 data, we found one super-Earth planet ($R_p = 1.589^{+0.095}_{-0.072}$ $R_\oplus$) transiting this star on a short period orbit ($P = 2.225177^{+6.6e-5}_{-6.8e-5}$ days). We followed this system up with spectroscopy to derive stellar parameters and determine a planet mass. From our 75 radial velocity measurements using HIRES on Keck I and HARPS-N on Telescopio Nazionale Galileo, we constrained the mass of K2-291 b to $M_p = 6.49 \pm 1.16$ $M_\oplus$. We found it necessary to model correlated stellar activity radial velocity signals with a Gaussian process in order to more accurately model the effect of stellar noise on our data; the addition of the Gaussian process also improved the precision of this mass measurement. With a bulk density of $\rho = 8.84^{+2.50}_{-2.03}$ g cm^{-3}, the planet is consistent with an Earth-like rock/iron composition and no substantial gaseous envelope.

Such an envelope, if it existed in the past, was likely eroded away by photo-evaporation during the first billion years of the star's lifetime.

9.2 Introduction

NASA's Kepler and K2 missions have have found hundreds of small, transiting planets with orbital periods less than 10 days. Planets with such short orbital periods are not represented among the Solar System planets. In this paper, we describe the discovery and characterization of one such super-Earth sized planet, K2-291 b, orbiting close to its host star (P = $2.225177^{+6.6e-5}_{-6.8e-5}$ days).

With a radius of $R_p = 1.589^{+0.095}_{-0.072}$ $R_\oplus$, K2-291 b lies between two peaks in planet occurrence (Fulton et al., 2017). This bimodality in radius space potentially corresponds to a divide in planet composition (Marcy et al., 2014; Weiss and Marcy, 2014; Lopez and Fortney, 2014; Rogers, 2015). By determining the mass of K2-291 b, we explore this potential boundary between super-Earth and sub-Neptune planets.

Furthermore, one way that sub-Neptunes can transition across this divide to become rocky super-Earths is through photoevaporation, a process where high energy photons from the star heat and ionize the envelope causing significant portions to escape. Low mass planets receiving high stellar fluxes will lose a larger portion of their envelopes (Owen and Wu, 2013; Lopez and Fortney, 2013). This paper explores the potential occurrence of such a process for K2-291 b.

In section 9.3 we describe the transit discovery and characterization from K2

data. Next, we describe our stellar characterization and stellar activity analysis in section 9.4. Our follow-up radial velocity observations are described and analyzed in section 9.5. We discuss implications of the bulk density of K2-291 b and potential planet evolution through photoevaporation in section 9.6. Finally, we conclude in section 9.7.

9.3 K2 Light Curve Analysis

Photometry of K2-291 was collected during Campaign 13 of NASA's K2 mission between 2017 Mar 08 and 2017 May 27. We processed the K2 data using a photometric pipeline that has been described in detail in past works by members of our team (Petigura et al., 2018, and references therin). In short, we used the package `k2phot` to analyze the K2 light curves (Petigura et al., 2015; Aigrain et al., 2016), perform photometry on the K2 target pixel files, model the time and position dependent photometric variability, and choose the aperture that minimizes noise on three-hour timescales.

We find the signal of one transiting planet at a period of P = $2.225177^{+6.6e-5}_{-6.8e-5}$ days (Figure 9.1, Table 9.1) in the light curve with the publicly available `TERRA` algorithm (Petigura et al., 2018). In short, `TERRA` flags targets with potential transit signals as threshold-crossing events (TCEs); once a TCE is flagged, `TERRA` masks the previous TCE and is run again on the target star to search for additional signals in the same system. For K2-291, `TERRA` finds one TCE with a signal-to-noise ratio of 21; this signal is consistent with a super-Earth-sized planet transit. After determining the parameters of the host star, described below, we perform a full MCMC analysis on the light curve

using a custom Python wrapper of the `batman`[1] transit fitting code (Kreidberg, 2015).

Our general approach is described further in our previous papers (e.g. Crossfield et al., 2016). In short, we initialize our `batman` fit with the best-fit parameters from `TERRA` to perform a maximum-likelihood fit and use `emcee`[2] (Foreman-Mackey et al., 2013) to determine errors. Our model parameters are the time of transit T_0, orbital period P, inclination i, radius of planet in stellar radii (R_p/R_*), transit duration T_{14}, second-to-third contact duration T_{23}, semimajor axis in stellar radii R_*/a, impact parameter b, and quadratic limb-darkening coefficients u_1 and u_2. Figure 9.1 shows our best-fit transit model and Table 9.1 lists the parameters and uncertainties.

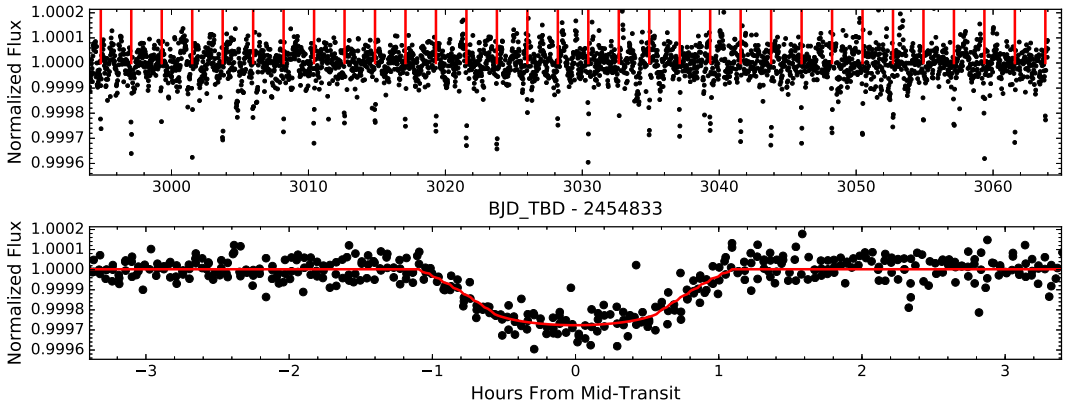

Figure 9.1: Top: Normalized flux of K2 light curve with red tick-marks indicating the transit times. Bottom: Phase-folded transit data (black points) including our model fit (red line).

[1] Available at https://github.com/lkreidberg/batman
[2] Available at https://github.com/dfm/emcee

Parameter	Name (units)	Value
T_0	Time of transit (BJD_{TDB})	$2457830.06163^{+0.00099}_{-0.00104}$
P	Period (days)	$2.225177^{+0.000066}_{-0.000068}$
i	Inclination (degrees)	$85.26^{+0.23}_{-0.20}$
R_P/R_*	Radius of planet in stellar radii (%)	$1.614^{+0.062}_{-0.033}$
T_{14}	Total duration (hr)	$1.719^{+0.041}_{-0.032}$
T_{23}	Second-to-third contact transit duration (hr)	$1.625^{+0.043}_{-0.035}$
R_*/a	Semimajor axis in stellar radii	$0.1283^{+0.0017}_{-0.0016}$
b	Impact parameter	$0.646^{+0.021}_{-0.026}$
a	Semimajor axis (AU)	$0.03261^{+0.00044}_{-0.00044}$
R_P	Radius ($R_\oplus$)	$1.589^{+0.095}_{-0.072}$
S_{inc}	Incident stellar flux ($S_\oplus$)	633^{+59}_{-56}

Table 9.1: K2-291 Transit Derived Parameters

9.4 Stellar Characterization

9.4.1 Data Collection

We collected 75 radial velocity measurements of K2-291 with HIRES and HARPS-N. We obtained 50 measurements with HIRES between August 2017 and February 2018. These data were collected with the C2 decker with a typical signal-to-noise ratio (SNR) of 150/pixel (125k on the exposure meter, ∼10 minute exposures). An iodine cell was used for wavelength calibration (Butler et al., 1996). We also collected a higher resolution template observation with the B3 decker on 2017 September 6 with 0.8" seeing. The template was a triple exposure with a total SNR of 346/pixel (250k each on the exposure meter) without the iodine cell. See chapter 5 and Howard et al. (2010) for more details on this data collection method.

We obtained 25 measurements with HARPS-N between November 2017 and March 2018 as part of the HARPS-N Collaboration's Guaranteed Time Observations

(GTO) program. The observations follow a standard observing approach of one or two observations per GTO night, separated by 2–3 hours. The spectra have signal-to-noise ratios in the range SNR = 35 – 99 (average SNR = 66), seeing and sky transparency dependent, at 550 nm in 30 minute exposures. This separation was designed to well sample the planet's orbital period and to minimize the stellar granulation signal (Dumusque et al., 2011).

The HIRES data reduction and analysis followed the California Planet Search method described in chapter 6 and further in Howard et al. (2010). The HARPS-N spectra were reduced with version 3.7 of the HARPS-N Data Reduction Software (DRS), which includes corrections for color systematics introduced by variations in seeing (Cosentino et al., 2014). The HARPS-N radial velocities were computed with a numerical weighted mask following the methodology outlined by Baranne et al. (1996) and Pepe et al. (2002). The resultant radial velocities are presented in Figure 9.4.

The HIRES data were collected with three consecutive exposures of ten minutes each to well sample the stellar p-mode (acoustic) oscillations which occur on a timescale of a few minutes. The HARPS-N data were collected in single observations. Multiple exposures per night were frequently taken separated by a few hours to better sample the planet orbital period.

9.4.2 Stellar Parameters

We derived the stellar parameters by combining constraints from spectroscopy, astrometry, and photometry. The methodology is described in detail in Fulton and

Parameter	Name (Units)	Value
Name and Magnitude (MAST)		
K2		291
EPIC		247418783
UCAC ID		558-013367
2MASS ID		05054699+2132552
Gaia DR2		3409148746676599168
HD		285181
Kp	mag	9.89
R	mag	9.84 ± 0.14
J	mag	8.765 ± 0.032
K	mag	8.35 ± 0.02
V	mag	10.01 ± 0.03
Location (Gaia 2018)		
RA	Right ascention (deg)	05 05 46.991
DEC	Declination (deg)	+21 32 55.021
π	Parallax (arcsec)	0.011076 ± 6.03e-05
d	Distance (pc)	$90.23^{+0.51}_{-0.46}$
Stellar Properties (Kosiarek 2019)		
A_v	Extinction (mag)	0.11740 ± 0.00061
R_*	Radius ($R_\odot$)	$0.899^{+0.035}_{-0.033}$
M_*	Mass ($M_\odot$)	0.934 ± 0.038
L_*	Luminosity ($L_\oplus$)	$0.682^{+0.014}_{-0.016}$
$T_{\rm eff}$	Effective temperature (K)	5520 ± 60
log(g)	Surface gravity (cgs)	4.50 ± 0.05
[Fe/H]	Metallicity (dex)	0.08 ± 0.04
$v \sin i$	Rotation (km s^{-1})	< 2.0
log(age)	Age (yr)	$9.57^{+0.30}_{-0.49}$
$\log(R'_{\rm HK})$	Chromospheric activity	-4.726

MAST: Mikulski Archive for Space Telescopes https://archive.stsci.edu/
Gaia 2018: Gaia Collaboration et al. (2018), Kosiarek 2019: Kosiarek et al. (2019a)

Table 9.2: K2-291 Stellar Parameters

Petigura (2018) and summarized in the following paragraphs. We used the HIRES template spectrum to determine the parameters described below. A comparison analysis performed on the HARPS-N data resulted in consistent parameters.

Stellar radius is derived from the Stefan Boltzman Law given an absolute bolometric magnitude $M_{\rm bol}$ and an effective temperature. We derived stellar effective temperature $T_{\rm eff}$, surface gravity $\log(g)$, and metallicity [Fe/H] by fitting our iodine-free template spectrum using the Spectroscopy Made Easy[3] (SME) spectral synthesis code (Valenti and Piskunov, 2012) following the prescriptions of Brewer et al. (2016). Stellar mass is then calculated using the package `isoclassify`[4] (Huber et al., 2017a). We then derived bolometric magnitudes according to

$$M_{\rm bol} = m_K - A_K - \mu - BC_K, \tag{9.1}$$

where m_K is the apparent K-band magnitude, A_K is the line-of-sight K-band extinction, μ is the distance modulus, and BC_K is the K-band bolometric correction. In our modeling, constraints on m_K come from 2MASS (Skrutskie et al., 2006) and constraints on μ come from the Gaia DR2 parallax measurement (Gaia Collaboration et al., 2018). We derived BC_K by interpolating the grid of BC_K computed by Conroy et al., in prep. To find $\rm A_K$, we first estimate $\rm A_v$ from a 3D interstellar dust reddening map by Green et al. (2018), then convert to $\rm A_K$ using the extinction vector from Schlafly et al. (2018).

[3] Available at `http://www.stsci.edu/~valenti/sme.html`
[4] Available at `https://github.com/danxhuber/isoclassify`

The stellar rotation velocity $v \sin i$, is computed using the SpecMatch-Syn code (Petigura, 2015). Due to the resolution of the instrument the code has been calibrated down to 2 km s^{-1}; values smaller should be considered as an upper limit. Although we measured a value of 0.2 km s^{-1}, we adopt $v \sin i < 2$ km s^{-1}.

9.4.3 Stellar Activity Analysis

We examine the K2 light curve periodicity (Figure 9.2) with a Lomb-Scargle periodogram from `scipy` (Jones et al., 2001) and attribute the clear signal at 18.1 days to rotational modulation of stellar surface features (e.g. spots). There is a secondary peak at half of the strongest peak, and no other significant peaks.

One must consider these timescales when planning radial velocity data collection and analysis to adequately average out or monitor these signals (Dumusque et al., 2011). As described in above, we chose the exposure time, spacing, and number of exposures to reduce the effects of p-modes and granulation. We investigated the potential radial velocity signal from the stellar rotation by examining the Calcium II H and K lines (S_{HK}) in the HIRES and HARPS-N data (Isaacson and Fischer, 2010).

We found a clear signal in both the S_{HK} and radial velocity data that matches the timescale of the rotation period of K2-291 (Figure 9.3), as determined from the K2 light curve; therefore we need to account for this signal in our radial velocity analysis.

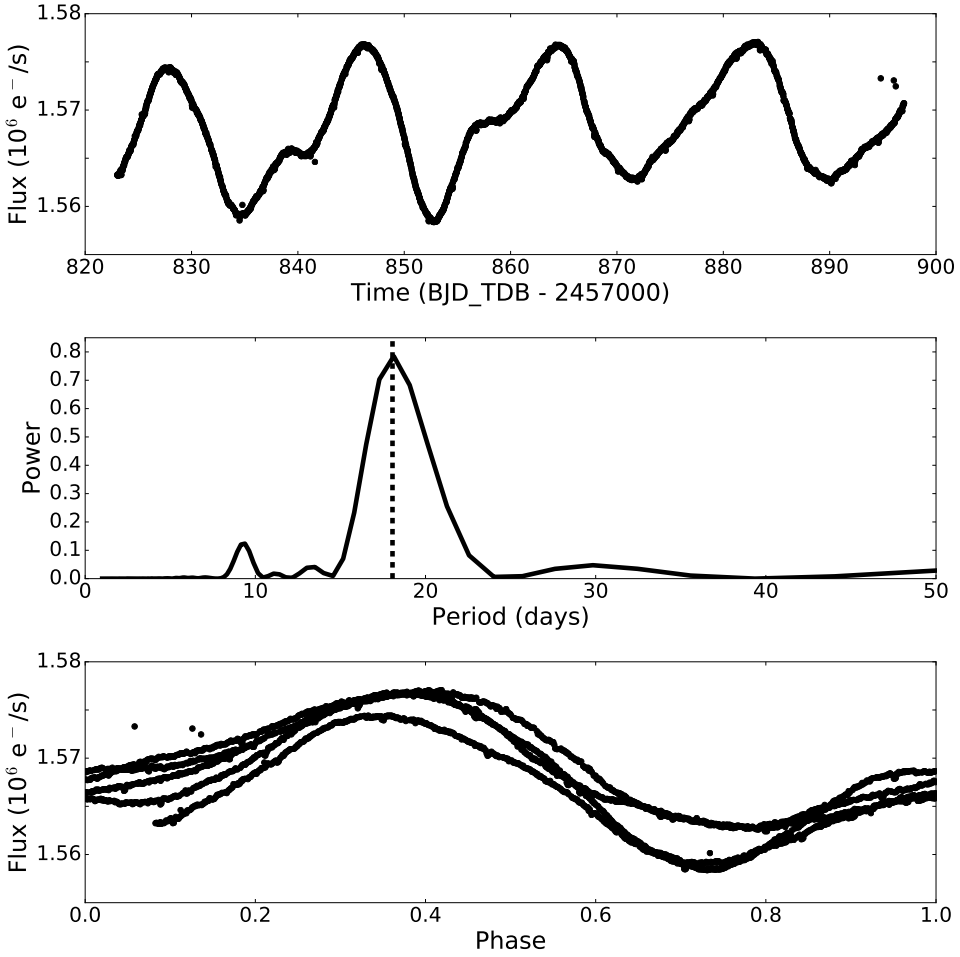

Figure 9.2: Top: Light curve of K2-291 from K2 C13. We attribute the periodicity to stellar rotation and the variation to star spot modulation. Middle: Lomb-Scargle periodogram of K2 data, illustrating clear periodicity at 18.1 days (dotted line). Bottom: K2 data phase-folded over 18.1 days.

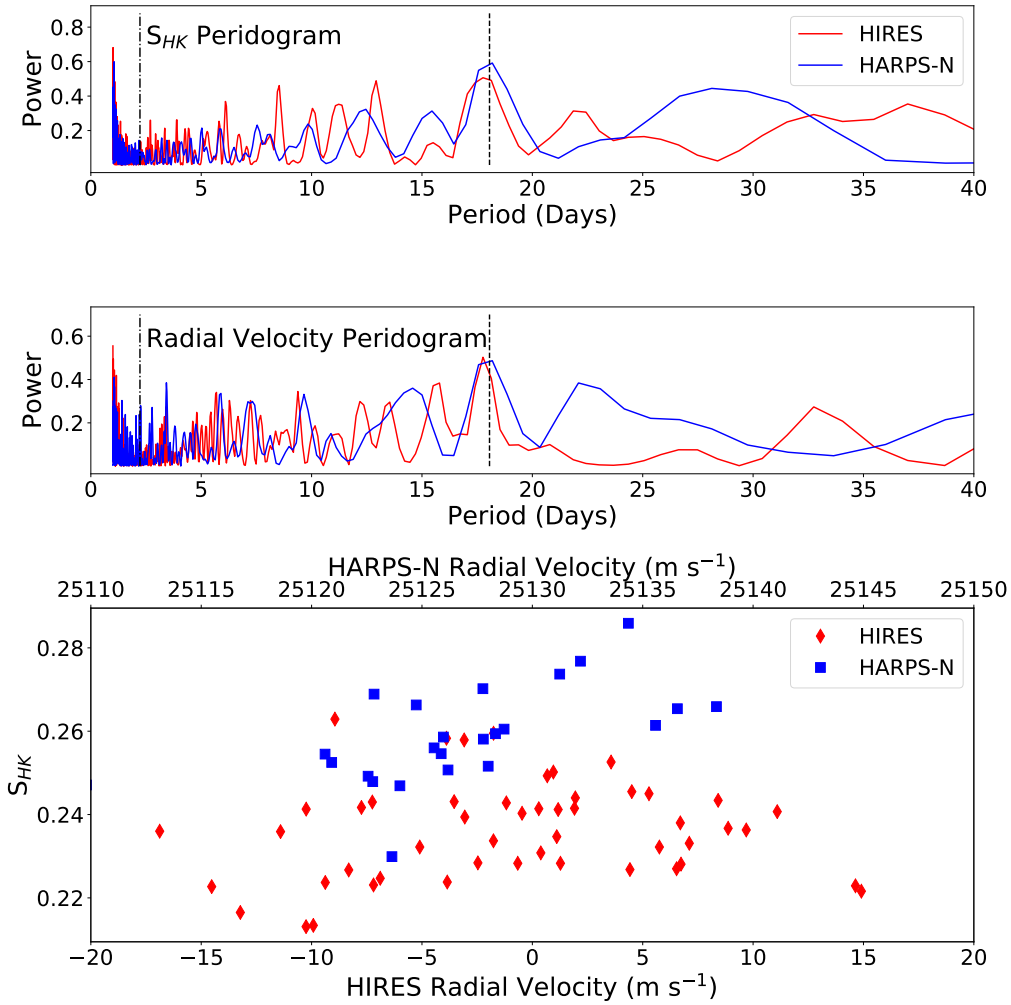

Figure 9.3: Periodograms of S_{HK} (top), radial velocity (middle), and S_{HK} vs. radial velocity (bottom). The stellar rotation period is represented by a dashed line. The planet's orbital period is represented by a dash-dot line. There is a strong radial velocity signal and S_{HK} signal at the stellar rotation period in both datasets.

9.5 Radial Velocity Analysis

9.5.1 Keplerian Radial Velocity Fit

A single planet at an orbital period of P=$2.225177^{+6.6e-5}_{-6.8e-5}$ days was found in the K2 photometry (section 9.3); we include a Gaussian prior on the orbital period P and time of transit $T_{\rm conj}$ from the K2 data (Table 9.1). We first modeled this system using a one-planet fit including a constant offset for each dataset γ. This fit results in a semi-amplitude for the 2.2 day planetary signal of K_p=3.1±1.7 m s^{-1}.

Next, we tested models including an additional trend ($\dot{\gamma}$), curvature ($\ddot{\gamma}$), and eccentricity (e, ω). We used the Bayesian Information Criteria (BIC) to evaluate if the fit improved sufficiently to justify the additional free parameters; a positive ΔBIC indicates an improved fit. The trend is the only additional parameter which has a noticeable ΔBIC (ΔBIC = 8.29); the trend is $\dot{\gamma}$ = 0.07±0.02 m s^{-2}. There is nearly no change for the curvature (ΔBIC = 0.84) or eccentric (ΔBIC = -1.90) cases. All three additional parameters result in semi-amplitudes within 1-σ of the circular fit.

9.5.2 Gaussian Process Inclusion and Training

Stellar activity of K2-291 has an appreciable effect on our measured radial velocities. As discussed previously, there is a periodic signal in the radial velocity data that matches both the stellar rotation period determined from K2 data and the periodicity in the Calcium H and K lines ($S_{\rm HK}$). We modeled this stellar signal simultaneously with our planet fit using a Gaussian process implemented in `radvel`.

We explore these hyper-parameters for this system by performing a maximum likelihood fit to the K2 light curve with the quasi-periodic kernel (Equation 7.1) then determine the errors through a MCMC analysis. We find $\gamma_{K2} = 1567969.00^{+1766.12}_{-1830.87}$ e^- s^{-1}, $\sigma = 54.60 \pm 9.57$ e^- s^{-1}, $\eta_1 = 4429.95^{+897.65}_{-673.95}$ e^- s^{-1}, $\eta_2 = 25.18^{+3.50}_{-3.59}$ days, $\eta_3 = 19.41^{+0.68}_{-1.14}$ days, $\eta_4 = 0.42^{+0.04}_{-0.03}$. This stellar rotation period (η_2) is consistent with the results of our periodogram analysis in subsection 9.4.3.

9.5.3 Gaussian Process Radial Velocity Fit

We then perform a radial velocity fit including a Gaussian process to account for the affects of stellar activity on our measurements. We model our Gaussian process as a sum of two quasi-periodic kernels, one for each instrument as HIRES and HARPS-N have different properties, such as wavelength ranges, that could alter the way that stellar activity affects the data. Each kernel includes identical timescale parameters (η_2, η_3, and η_4) but allows for different amplitudes (η_1).

We inform the priors on these hyper-parameters from the Gaussian process light curve fit. η_1 is left as a free parameter as light curve amplitude cannot be directly translated to radial velocity amplitude. η_2 has a Gaussian prior describing the exponential decay of the spot features (25.18 ± 3.59 days). η_3 has a Gaussian prior constrained from the stellar rotation period (19.14 ± 1.14 days). η_4 constrains the number of maxima and minima per rotation period with a Gaussian prior (0.42 ± 0.04), as described in López-Morales et al. (2016). We do not include a prior on the phase of the periodic component of the stellar rotation because spot modulation tends to manifest in radial

velocity data with a relative phase shift.

The planet parameters derived from our Gaussian process analysis are consistent with our original, non-Gaussian process fit within 1-σ. The uncertainty on the semi-amplitude of the planet signal has decreased by a factor of three to $K_p = 3.33 \pm 0.59$ m s^{-1}. We then investigate the inclusion of additional parameters with our Gaussian process fit. All of the tested models increased the BIC value; therefore none of them justified the additional parameters. We adopt the model including the Gaussian process with no additional parameters as our best fit, all other models have results within 1-σ; our best-fit parameters are listed in Table 9.3.

We choose to include a Gaussian process in our analysis to improve the accuracy of our results by including the affects of stellar activity. The Gaussian process was able to also improve the precision of the mass measurement by a factor of three since the planet orbital period is far from the stellar rotation period, both periods were well sampled with the data, and the stellar activity is dominated by the rotation signal.

9.6 Composition and Photoevaporation Discussion

Composition models and observations of Kepler planets have shown a dividing line between super-Earth and sub-Neptune planets at 1.5-2 $R_\oplus$ (e.g. Weiss and Marcy, 2014; Lopez and Fortney, 2014; Rogers, 2015; Dressing and Charbonneau, 2015; Fulton et al., 2017). K2-291 b is at the inner edge of the divide, which makes its composition particularly interesting. With a mass of 6.49 ± 1.16 $M_\oplus$ and a radius of $1.589^{+0.095}_{-0.072}$ $R_\oplus$,

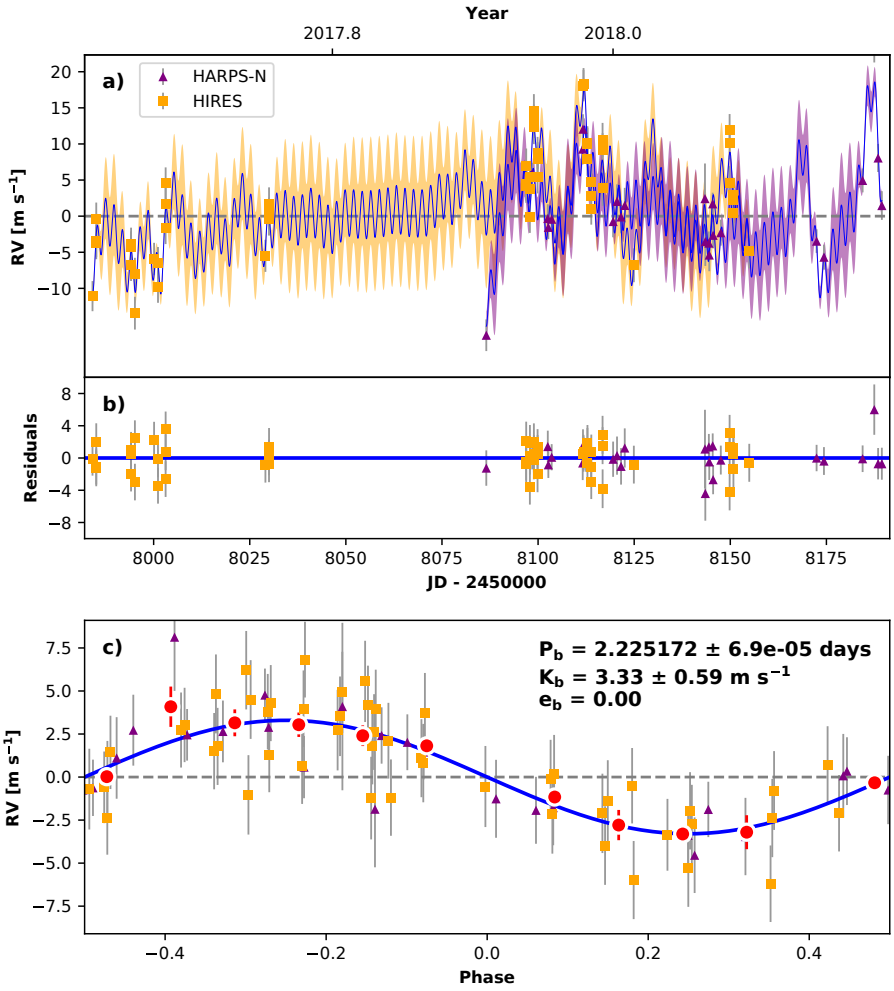

Figure 9.4: Best-fit one-planet Keplerian orbital model for K2-291. The maximum likelihood model is plotted while the orbital parameters listed in Table 9.3 are the median values of the posterior distributions. The thin blue line is the best fit one-planet model with the mean Gaussian process model; the colored area surrounding this line includes the 1-σ maximum likelihood Gaussian process uncertainties. We add the radial velocity jitter term(s) listed in Table 9.3 in quadrature with the measurement uncertainties for all radial velocities. **b)** Residuals to the best fit one-planet model and Gaussian process model. **c)** Radial velocities phase-folded to the ephemeris of planet b. The small point colors and symbols are the same as in panel **a**. Red circles are the same velocities binned in 0.08 units of orbital phase. The phase-folded model for planet b is shown as the blue line.

Parameter	Name (Units)	Value
Planet Parameters		
P_b	Period (days)	$2.225172^{+6.9e-05}_{-7e-05}$
$T\mathrm{conj_b}$	Time of conjunction ($\mathrm{BJD_{TDB}}$ - 2457000)	$830.0616^{+0.0011}_{-0.0010}$
e_b	Eccentricity	$\equiv 0.0$
ω_b	Argument of periapse (radians)	$\equiv 0.0$
K_b	Semi-amplitude (m s^{-1})	3.33 ± 0.59
M_b	Mass ($M_\oplus$)	6.49 ± 1.16
ρ_b	Density (g cm^{-3})	$8.84^{+2.50}_{-2.03}$
Other Parameters		
γ_{HIRES}	Mean center-of-mass velocity (m s−1)	-3.5 ± 3.2
$\gamma_{\mathrm{HARPS-N}}$	Mean center-of-mass velocity (m s−1)	$25126.2^{+3.4}_{-3.5}$
$\dot{\gamma}$	Linear acceleration (m s^{-1} day^{-1})	$\equiv 0.0$
$\ddot{\gamma}$	Quadratic acceleration (m s^{-1} day^{-2})	$\equiv 0.0$
σ_{HIRES}	Jitter (m s^{-1})	$1.85^{+0.43}_{-0.37}$
$\sigma_{\mathrm{HARPS-N}}$	Jitter (m s^{-1})	$1.43^{+0.85}_{-0.67}$
$\eta_{1,HIRES}$	Amplitude of covariance (m s^{-1})	$8.45^{+2.21}_{-1.65}$
$\eta_{1,HARPS-N}$	Amplitude of covariance (m s^{-1})	$8.59^{+2.23}_{-1.77}$
η_2	Evolution timescale (days)	$26.09^{+3.50}_{-3.62}$
η_3	Recurrence timescale (days)	$18.66^{+0.95}_{-0.79}$
η_4	Structure parameter	0.41±0.04

Table 9.3: K2-291 Radial Velocity Fit Parameters

K2-291 b has a density consistent with that of a silicate planet with an iron core ($\rho = 8.84^{+2.50}_{-2.03}$ g cm^{-3}).

We investigated its composition using Equation 8 from Fortney et al. (2007), which assumes a pure silicate and iron composition, to estimate the mass fraction of each. For our mean mass and radius, the mass fraction of silicates is 0.61 and the mass fraction of iron is 0.39, similar to the 0.35 iron core mass fraction of the Earth. For a high gravity case (1-σ low radius, 1-σ high mass), the mass fraction of silicates would be 0.39. For a low gravity case (1-σ high radius, 1-σ low mass), the mass fraction of silicates would be 0.94. In all cases, no volatiles are needed to explain the mass and radius of K2-291 b.

We also estimated the maximum envelope mass fraction of K2-291 b through a model grid from Lopez and Fortney (2014). This grid assumes a solar metallicity envelope with a minimum envelope mass fraction of 0.1%. We generated 100000 random samples of the envelope fraction from our normal distributions on K2-291 b's mass, radius, age, and flux. From this, we determined that the 3-σ upper limit on the envelope fraction is 0.3%. This result is consistent with other small, close-in Kepler planets; Kepler planets within 0.15 AU and smaller than 2 $R_\oplus$ have an envelope fraction less than 1% (Wolfgang and Lopez, 2015).

K2-291 b's lack of a substantial volatile envelope could be explained by atmospheric loss. For lower mass planets experiencing a large amount of stellar insolation, photoevaporation (hydrodynamic escape) is the dominant atmospheric loss process. Photoevaporation occurs when high energy photons from the host star ionize and heat

the atmosphere causing it to expand and escape (Owen and Wu, 2013). K2-291 b is potentially the core of a sub-Neptune planet that underwent photoevaporation. We cannot, however, rule out a scenario where K2-291 b formed with a high density from its onset. In that case, perhaps K2-291 b formed after the gas disk had dissipated, or giant impacts by planetesimals stripped the envelope early in its formation.

Due to the hydrodynamic escape of the envelope for close-in planets, the boundary between complete loss and retention of 1% of the envelope is at 0.1 AU for a 6 $M_\oplus$ planet orbiting a solar mass star (Owen and Wu, 2013). K2-291 b orbits within this boundary at a = 0.03261±0.00044 AU. For the mass ($M_p = 6.49 \pm 1.16$) and stellar insolation ($S_{\rm inc} = 633^{+59}_{-56}$ $S_\oplus$) of K2-291 b specifically, all of its hydrogen-helium should have been lost between 100 Myr and 1 Gyr, depending on the original hydrogen-helium mass fraction and mass loss efficiency (Lopez and Fortney, 2013). We determined an age from the HIRES spectra of $3.7^{+3.7}_{-2.5}$ Gyr, longer than this photevaporation timescale.

We ran additional models using the Lopez and Fortney (2014) model grid to calculate the radius K2-291 b would have with an additional hydrogen-helium envelope. Adding 0.1% H/He by mass would result in a planet radius of $R_p = 1.82$ $R_\oplus$. Similarly, an additional 1% or 10% would equal a radius of $R_p = 2.2$ $R_\oplus$ or $R_p = 3.7$ $R_\oplus$, respectively. Therefore, a small addition of between 1% and 10% H/He would increase the radius of K2-291 b enough to move the planet across the Fulton gap to the sub-Neptune side. Together, these analyses imply that K2-291 b may have formed as a sub-Neptune with a substantial volatile envelope and transitioned across the Fulton gap to a super-Earth planet through photevaporation.

9.7 Conclusion

We described the discovery and characterization of K2-291 b, a super-Earth planet with a radius of $R_p = 1.589^{+0.095}_{-0.072}$ $R_\oplus$. We collected spectra to characterize the stellar properties and perform radial velocity analyses. We determined a planet mass of $M_p = 6.49 \pm 1.16$ $M_\oplus$.

We accounted for quasi-periodic radial velocity variations induced by the host star's moderate activity levels using Gaussian process regression (Blunt et al. in prep, Haywood et al., 2014). This improves the accuracy of our mass determination (e.g. Haywood et al., 2018). In our case, the Gaussian process framework also increases the precision of our mass determination over an uncorrelated-noise only treatment. The increased precision likely results from favourable sampling of the rotational and active-region timescales (López-Morales et al., 2016), combined with the fact that the orbital period is very distinct from these activity timescales.

The density of K2-291 b ($\rho = 8.84^{+2.50}_{-2.03}$ g cm^{-3}) is consistent with a silicate and iron composition. The high density of the planet, along with the high solar flux received by the planet ($S_{\rm inc} = 633^{+59}_{-56}$ $S_\oplus$), indicate that if K2-291 b formed with a substantial envelope, it has been eroded away by photo-evaporation.

Chapter 10

GJ 3470

10.1 Abstract

We report an improved mass and density for GJ 3470 b, a Neptune-sized planet orbiting a bright M-dwarf, derived from new radial velocity observations. We analyzed ground-based photometry from the Fairborn Observatory to determine the characteristic stellar activity timescales for our Gaussian Process fit, including the stellar rotation period and activity region decay timescale. A stellar rotation signal is evident in the radial velocity data and is included in our fit using a Gaussian process trained on the photometry. We find the mass of GJ 3470 b to be $12.58^{+1.31}_{-1.28}$ $M_{\oplus}$. Due to the low planet density ($0.93^{+0.56}_{-0.31}$ g cm^{-3}) and bright host star (K = 8.0 mag), GJ 3470 b is a good candidate for JWST transmission spectra. This updated mass measurement provides key information for interpreting future transmission spectra observations.

10.2 Introduction

GJ 3470 is a bright (K = 8.0 mag), nearby ($29.9^{+3.7}_{-3.4}$ pc) M1.5 dwarf hosting one Neptune-sized planet in a 3.33 day orbit (Cutri et al., 2003; Bonfils et al., 2012), the full system parameters are listed in Table 10.1. GJ 3470 b was discovered in a HARPS radial velocity campaign that searched for short-period planets orbiting M dwarfs and was subsequently observed in transit. GJ 3470 b has an equilibrium temperature near 700 K and radius of 3.9 $R_\oplus$. Its mass has been measured previously to be 13.73±1.61, 14.0±1.8, and $13.9^{+1.5}_{-1.4}$ $M_\oplus$ by Bonfils et al. (2012), Demory et al. (2013), and Biddle et al. (2014) respectively. Its low density supports a substantial atmosphere covering the planet (Biddle et al., 2014). Five previous studies have investigated its atmospheric composition. Fukui et al. (2013) found variations in the transit depths in the J, I, and 4.5 μm bands that suggest the atmospheric opacity varies with wavelength due to the absorption or scattering of stellar light by atmospheric molecules. Nascimbeni et al. (2013) detected a transit depth difference between the ultraviolet and optical wavelengths also indicating a Rayleigh-scattering slope, confirmed by Biddle et al. (2014) and Dragomir et al. (2015). Crossfield et al. (2013) found a flat transmission spectrum in the K-band suggesting a hazy, methane-poor, or high-metallicity atmosphere. Additionally, GJ 3470 b is being targeted by JWST GTO observations.

Parameter	Value	Units	Source
Photometric Properties			
Spectral type	M1.5		Reid et al. (1997)
V	12.3	mag	Bonfils et al. (2012)
K	7.989 ± 0.023	mag	Cutri et al. (2003)
J	8.794 ± 0.019	mag	Cutri et al. (2003)
H	8.206 ± 0.023	mag	Cutri et al. (2003)
Rotation Period	21.54 ± 0.49	days	Kosiarek et al. (2019b)
Spectroscopic Properties			
Luminosity	0.029 ± 0.002	$L_\odot$	Bonfils et al. (2012)
Mass	0.51 ± 0.06	$M_\odot$	Biddle et al. (2014)
Radius	0.48 ± 0.04	$R_\odot$	Biddle et al. (2014)
Distance	$30.7^{+2.1}_{-1.7}$	pc	Demory et al. (2013)
Age	0.3–3	Gyr	Bonfils et al. (2012)
Temperature	3652 ± 50	K	Biddle et al. (2014)
Surface Gravity	4.658 ± 0.035	cgs	Demory et al. (2013)
[Fe/H]	+0.20 ± 0.10		Demory et al. (2013)
Transit Properties			
T_0 (−2450000)	6677.727712 ± 0.00022	BJD	Dragomir et al. (2015)
T_{14}	$0.07992^{+0.00100}_{-0.00099}$	days	Dragomir et al. (2015)
P	3.3366413±0.0000060	days	Dragomir et al. (2015)
R_p	3.88 ± 0.32	$R_\oplus$	Biddle et al. (2014)
a/R_*	$12.92^{+0.72}_{-0.65}$		Dragomir et al. (2015)
T_{eq}	615 ± 16	K	Bonfils et al. (2012)

Table 10.1: GJ 3470 Stellar and Planet b Transit Properties

10.3 Radial Velocity Analysis

10.3.1 Data Collection

We obtained radial velocity measurements of GJ 3470 using the High Resolution Echelle Spectrometer (HIRES, Vogt et al., 1994) on the Keck I Telescope. We collected 56 measurements of GJ 3470 from 2012 Sep 25 to 2017 Mar 15. These spectra were taken with an iodine cell and the C2 decker; a template spectrum was also taken in order to calibrate the wavelength and estimate the radial velocity uncertainty. On average, measurements of GJ 3470 were collected with an exposure time of 1200s in order to reach a SNR of 60/pixel (40k counts). The observations and data reduction followed the California Planet Search method described in Howard et al. (2010).

An additional 114 Doppler measurements collected with HARPS were used in the following GJ 3470 analysis, 61 from the original discovery paper (Bonfils et al., 2012) and 53 additional measurements taken in the same fashion (Astudillo-Defru et al., 2015, 2017). Our HIRES measurements have an average uncertainty of 1.9 m s^{-1} while the two sets of HARPS measurements have an average uncertainty of 4.2 m s^{-1}.

10.3.2 Stellar Activity Analysis

We first analyzed ground-based photometry of GJ 3470 to determine the stellar rotation period. Then we examined the potential effects of stellar activity in the radial velocity data by measuring the strength of these Calcium II H and K spectral lines ($S_{\rm HK}$) in our HIRES radial velocity measurements (Isaacson and Fischer, 2010). We

produced periodograms with all of these data products to look for similarities between them. Finally, we modeled the radial velocity data of GJ 3470 with Gaussian processes trained on the photometry to remove correlated stellar activity.

Photometry was collected at the Fairborn Observatory in Arizona with the Tennessee State University Celestron C14 0.36 m Automated Imaging Telescope (AIT) (Henry, 1999; Eaton et al., 2003). The AIT has a SBIG STL-1001E CCD camera and a Cousins R filter. Images were corrected for bias, flat fielding, and differential extinction. Differential magnitudes were computed using five field stars. 842 observations were collected from Dec 2012 to May 2017 (Table 10.2).

The tallest peak in the periodogram (Figure 10.1) corresponds to a period of 21.54 ± 0.49 days; the uncertainty is the standard deviation between the peaks for each observing season. We interpret this peak as the stellar rotation period, as shown by the brightness variation from star spots rotating in and out of view. This rotation period is consistent with that found by Biddle et al. (2014).

For GJ 3470, there is a hint of an RV-$S_{\rm HK}$ correlation in the early HIRES data; although the full dataset has a correlation coefficient of -0.0753 and p-value of 0.5812. Furthermore, the radial velocity periodogram contains a significant peak near the stellar

Observing Season	Date Range (HJD)	N_{obs}	Sigma (mag)	Mean (mag)
2012-2013	2456272–2456440	297	0.00535	-0.99917 ± 0.00031
2013-2014	2456551–2456813	289	0.00397	-1.00205 ± 0.00023
2014-2015	2456949–2457180	108	0.00419	-1.00494 ± 0.00040
2015-2016	2457323–2457508	83	0.00384	-1.00214 ± 0.00042
2016-2017	2457705–2457879	65	0.00586	-1.00417 ± 0.00073

Table 10.2: Summary of C14 AIT Photometric Observations of GJ 3470

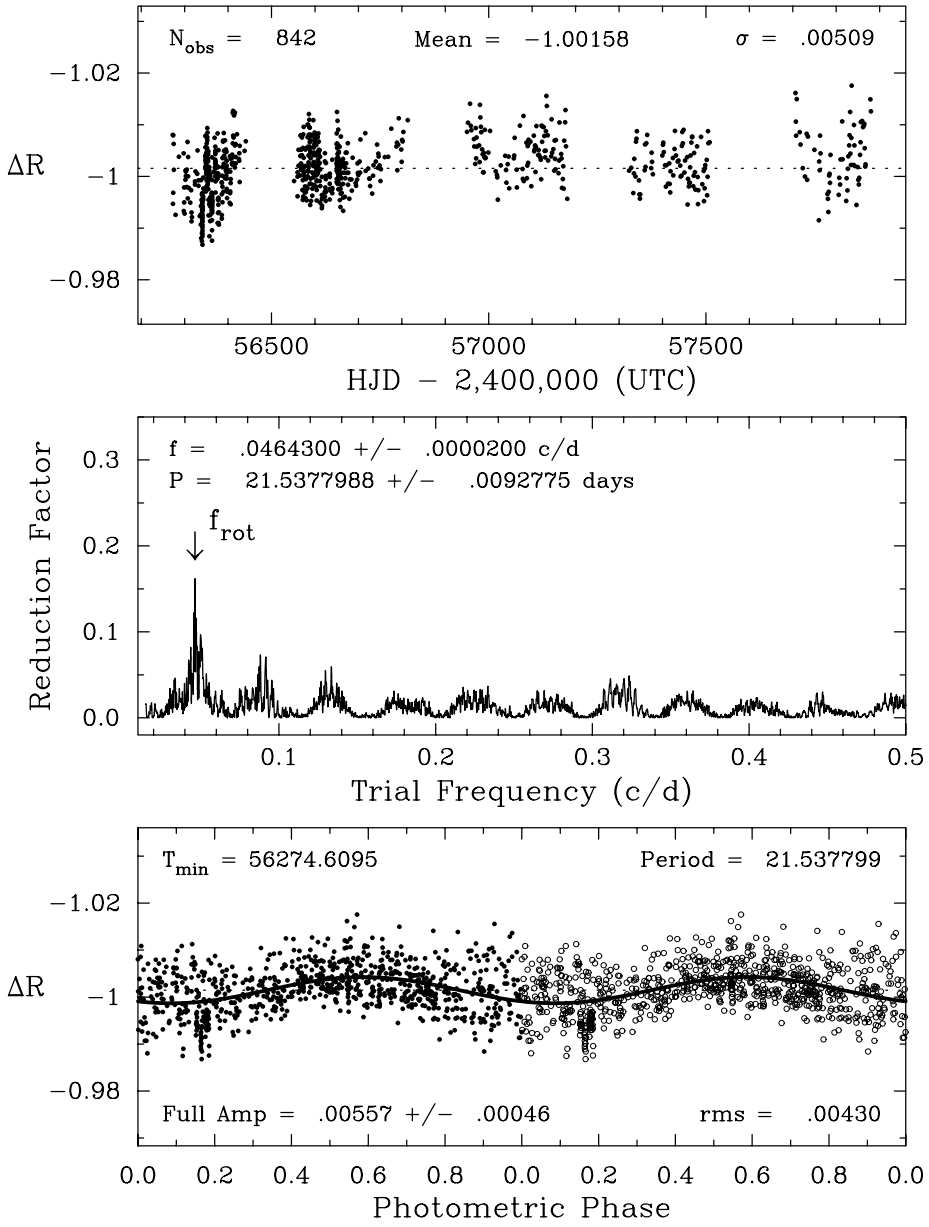

Figure 10.1: Top: Photometry of GJ 3470 from 2012 to 2017 from the C14 AIT at Fairborn Observatory. Middle: Power spectrum of the observations in frequency space illuminated a stellar rotation period of 21.54 days. We inflated the period uncertainty to 21.54 ± 0.49 days, to account for the variation in rotation period between years. Bottom: Phased photometry over the periodogram peak at 21.54 days.

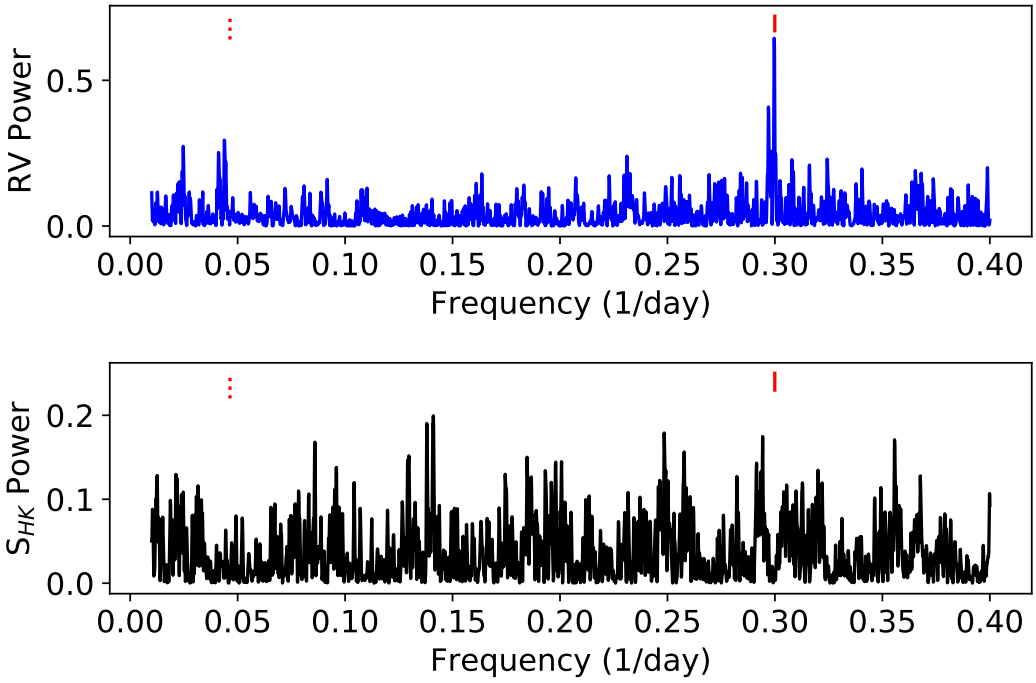

Figure 10.2: GJ 3470: Periodogram of the radial velocity data (top) and S_{HK} periodogram (bottom). The main peak in radial velocity at 3.3 days matches the period of planet b (red tick mark). The next prominent peaks are near the stellar rotation period (red dotted mark, see Figure 10.1). The radial velocity and S_{HK} periodograms do not have any prominent peaks in common.

rotation period (Figure 10.2), which suggests that the stellar rotation signal needs to be accounted for in the radial velocity analysis. We therefore used this photometry to inform our Gaussian Processes priors in the radial velocity fit.

10.3.3 Radial Velocity Fit

For our radial velocity analysis of GJ 3470, we adopt the period, time of conjunction, and planet radius derived from a variety of ground based telescopes (Biddle et al., 2014). The remaining parameters were initialized from Dragomir et al. (2015).

We used a Gaussian process to model the correlated noise associated with the stellar activity in our radial velocity fit. We ran our Gaussian process analysis on the photometry from Fairborn Observatory (FO) and find $\gamma_{FO} = 1.003 \pm 0.001$, $\sigma_{FO} = 0.0029 \pm 0.0001$, $\eta_1 = -0.0036^{+0.0003}_{-0.0004}$, $\eta_2 = 48.98^{+9.54}_{-7.28}$ days, $\eta_3 = 21.84^{+0.35}_{-0.36}$ days, $\eta_4 = 0.55 \pm 0.06$. This stellar rotation period (η_3) is consistent with the results of our periodogram analysis to within 1-σ.

We then perform our radial velocity fit including a Gaussian process modeled as a sum of two quasi-periodic kernels (Equation 7.1), one for each instrument, as HIRES and HARPS have different properties that could alter the effect of stellar activity on the data. Each kernel includes identical η_2, η_3, and η_4 parameters but allows for different η_1 values. Our priors are as follows: η_1 is left as a free parameter as light curve amplitude cannot be directly translated to radial velocity amplitude, for η_2, η_3, and η_4, we used a kernel density estimate of the Fairborn Observatory photometry posteriors.

After running an initial radial velocity fit including only one circular, Keplerian

planet signal, we investigated models including an acceleration term, curvature term, and eccentricity. The Aikike Information Criterion (AIC) was used to determine if the fit improvement justified the additional parameters; a ΔAIC of < 2 indicates a similar fit, $2 < \Delta$AIC< 10 favors the additional parameter, and a ΔAIC > 10 is a strong justification for the additional parameter. Only the eccentricity parameters improved the AIC (ΔAIC_{acc} = -0.71, ΔAIC_{curv} = -1.44, and ΔAIC_{ecc} = 6.45). All of the tested radial velocity models resulted in planet masses within 1-σ of the circular fit values shown in Table 10.3

We then investigated a model including an eccentricity constraint from Spitzer observations of the secondary eclipse. The secondary eclipse was 0.309 days later than expected for a circular orbit, which results in a constraint on $ecos(\omega)$ of $0.014546^{+0.000753}_{-0.000659}$ (Benneke et al., 2019). For this fit we used $ecos(\omega)$ and $esin(\omega)$ as the fitting basis due to the prior set by the secondary eclipse. We find an eccentricity of $e_b = 0.114 \pm 0.051$ for the eccentric model constrained by this secondary eclipse measurement, the best fit curve is shown in Figure 10.3.

The non-zero eccentricity value of GJ 3470 b is particularly interesting in the context of other systems. GJ 436 b, another planet similar in mass, radius, period, and stellar host, has a puzzlingly high eccentricity of 0.150 $\pm$ 0.012 (Deming et al., 2007). These high eccentricity values may be an emerging clue on how these types of planets form and migrate.

Parameter	Value	Units
Gaussian Priors		
$T\mathrm{conj_b}$	2455953.6645 ± 0.0034	JD
P_b	3.3371 ± 0.0002	days
$e \cos \omega_b$	0.01454 ± 0.00075323	
$\eta_{1,HIRES}$	[0,100]	m s^{-1}
$\eta_{1,HARPS}$	[0,100]	m s^{-1}
η_2	$48.98^{+9.54}_{-7.28}$	days
η_3	$21.84^{+0.35}_{-0.36}$	days
η_4	0.55 ± 0.006	
Orbital Parameters		
P_b	$3.336649^{+8.4e-05}_{-8.1e-05}$	days
$T\mathrm{conj_b}$	2455953.663 ± 0.0035	JD
e_b	$0.114^{+0.052}_{-0.051}$	
ω_b	$-1.44^{+0.1}_{-0.04}$	radians
K_b	$8.21^{+0.47}_{-0.46}$	m s^{-1}
M_b	$12.58^{+1.31}_{-1.28}$	$M_\oplus$
ρ_b	$0.93^{+0.56}_{-0.31}$	g cm^{-3}
Other Parameters		
γ_{HIRES}	$0.3^{+1.2}_{-1.1}$	m s^{-1}
γ_{HARPS}	$26500.52^{+0.59}_{-0.6}$	m s^{-1}
$\dot{\gamma}$	$\equiv 0.0$	m s^{-1} day^{-1}
$\ddot{\gamma}$	$\equiv 0.0$	m s^{-1} day^{-2}
σ_{HIRES}	$1.9^{+0.7}_{-0.67}$	m s^{-1}
σ_{HARPS}	$0.0023^{+0.49}_{-0.0023}$	m s^{-1}
$\eta_{1,HIRES}$	$3.94^{+0.90}_{-0.78}$	m s^{-1}
$\eta_{1,HARPS}$	$1.79^{+0.69}_{-0.71}$	m s^{-1}
η_2	$49.40^{+10.00}_{-7.55}$	days
η_3	$21.92^{+0.42}_{-0.41}$	days
η_4	0.56 ± 0.06	

Table 10.3: GJ 3470 Radial Velocity MCMC Priors and Posteriors

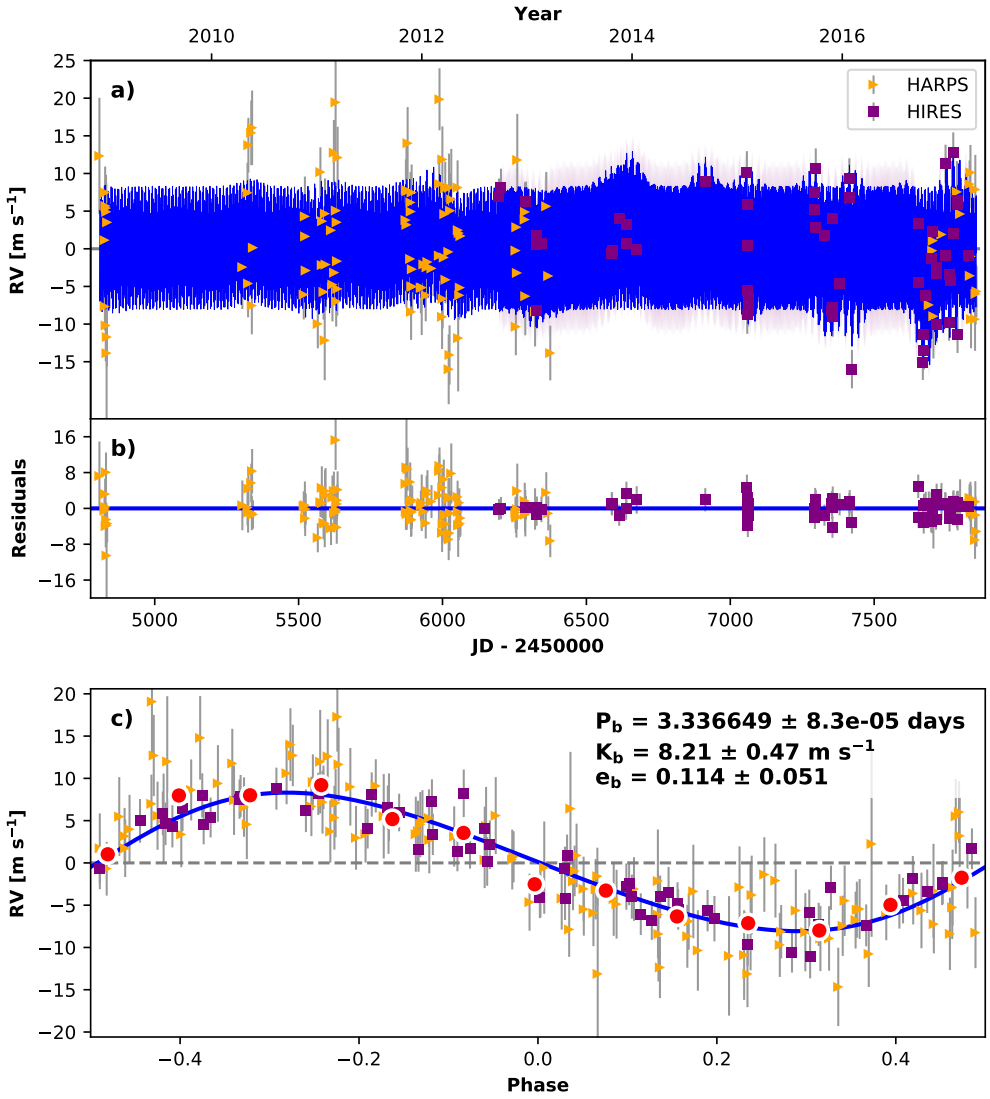

Figure 10.3: Best-fit 1-planet Keplerian orbital model for GJ 3470 with $ecos(\omega)$ constraints from the secondary eclipse observation. The thin blue line is the best fit 1-planet model with the mean Gaussian process model; the colored area surrounding this line includes the 1-σ maximum likelihood Gaussian process uncertainties. We add in quadrature the radial velocity jitter term(s) listed in Table 10.3 with the measurement uncertainties for all RVs. **b)** Residuals to the best fit 1-signal model. **c)** RVs phase-folded to the ephemeris of planet b. The small point colors and symbols are the same as in panel a). Red circles are the same velocities binned in 0.08 units of orbital phase.

10.4 Conclusion

Photometric monitoring of planet-hosting stars is important to determine the stellar rotation period and spot modulation to therefore separate the stellar activity from the planet-induced radial velocity signals. $S_{\rm HK}$ was not be a good indicator for stellar activity in this M dwarf star. There was little to no correlation between the RVs and $S_{\rm HK}$; however, the rotation period found by our photometric monitoring was present in our radial velocity data. We used a Gaussian process trained on our photometry to increase the accuracy of our radial velocity fits.

From our radial velocity analysis, we determine the mass of GJ 3470 b to nearly ten sigma ($M_b = 12.58^{+1.31}_{-1.28}$ $M_\oplus$). We additionally constrain the planet eccentricity ($e_b = 0.114^{+0.52}_{-0.51}$) from our radial velocity analysis and a measured secondary eclipse from Spitzer. Non-zero eccentricities may be an emerging clue on how warm-Neptunes form and migrate.

Chapter 11

K2-3

11.1 Abstract

We report improved masses, radii, and densities for three planets in the K2-3 system, derived from a combination of new radial velocity and transit observations. We analyzed ground-based photometry from the Evryscope to determine the characteristic stellar activity timescales for our Gaussian Process fit, including the stellar rotation period and activity region decay timescale. The stellar rotation signal is included in our fit using a Gaussian process trained on the photometry. We find the masses of K2-3 b and K2-3 c to be $6.48^{+0.99}_{-0.93}$ $M_\oplus$ and $2.14^{+1.08}_{-1.04}$ $M_\oplus$. K2-3 d was not significantly detected and has a 3-σ upper limit of 2.80 $M_\oplus$. This system is a good training case for characterizing future TESS systems; due to the low planet densities ($\rho < 3.7$ g cm^{-3}) and bright host star (K = 8.6 mag), they are ideal candidates for transmission spectroscopy in order to characterize the atmospheric compositions of small planets.

Parameter	Value	Units	Source
Identifying Information			
RA	11:29:20.388		Crossfield et al. (2015)
DEC	-01:27:17.23		Crossfield et al. (2015)
Photometric Properties			
J	9.421 ± 0.027	mag	Cutri et al. (2003)
H	8.805 ± 0.044	mag	Cutri et al. (2003)
K	8.561 ± 0.023	mag	Cutri et al. (2003)
Kp	11.574	mag	Huber et al. (2016)
Rotation period	40 ± 2	days	Kosiarek et al. (2019b)
Spectroscopic Properties			
Barycentric RV	32.6 ± 1	km/s	Crossfield et al. (2015)
Distance	45 ± 3	pc	(Crossfield et al., 2015)
Hα	0.38 ± 0.06	Ang	Crossfield et al. (2015)
Age	≥ 1	Gyr	(Crossfield et al., 2015)
Spectral Type	M0.0 ± 0.5 V		Crossfield et al. (2015)
[Fe/H]	-0.32 ± 0.13		Crossfield et al. (2015)
Temperature	3896 ± 189	K	Crossfield et al. (2015)
Mass	0.601 ± 0.089	M_{Sun}	Crossfield et al. (2015)
Radius	0.561 ± 0.068	R_{Sun}	Crossfield et al. (2015)
Density	3.58 ± 0.61	ρ_{Sun}	Almenara et al. (2015)
Surface Gravity	4.734 ± 0.062	cgs	Almenara et al. (2015)

Table 11.1: K2-3 Stellar Properties

11.2 Introduction

K2-3 (EPIC 201367065) is a bright (Ks = 8.6 mag), nearby (45 ± 3 pc) M0 dwarf star hosting three planets from 1.5–2 $R_\oplus$ at orbital periods between 10 and 45 days (Crossfield et al., 2015), the full system parameters are listed in Table 11.1. These planets receive 1.5–10 times the flux incident on Earth; planet d orbits near the habitable zone.

K2-3 b, c, and d were discovered in K2 photometry (Crossfield et al., 2015). Since then, there have been multiple radial velocity and transit follow-up measurements. Almenara et al. (2015) collected 66 HARPS spectra and determined the mass of planet

b, c, and d to be 8.4 ± 2.1, $2.1^{+2.1}_{-1.3}$, and 11.1 ± 3.5 $M_\oplus$ respectively. Almenara et al. (2015) cautions that the radial velocity semi-amplitudes of planets c and d are likely affected by stellar activity. Dai et al. (2016) collected 31 spectra with Planet Finder Spectrograph (PFS) on Magellan and modeled the radial velocity data with Almenara's HARPS data. The combined datasets constrained the masses of planets b, c, and d to be 7.7 ± 2.0, < 12.6, and $11.3^{+5.9}_{-5.8}$ $M_\oplus$ respectively. Damasso et al. (2018) performed a radial velocity analysis on a total of 132 HARPS spectra and 197 HARPS-N spectra, including the Almenara sample. This HARPS analysis found the mass of planet b and c to be 6.6 ± 1.1 and $3.1^{+1.3}_{-1.2}$ $M_\oplus$, respectively. The mass of planet d is estimated as $2.7^{+1.2}_{-0.8}$ $M_\oplus$ from a suite of injection-recovery tests. Beichman et al. (2016) refined the ephemeris and radii of the three planets with seven follow-up Spitzer transits and Fukui et al. (2016) observed a ground-based transit of K2-3 d to further refine its ephemeris.

11.3 Radial Velocity Analysis

11.3.1 Data Collection

We obtained radial velocity measurements of K2-3 using the High Resolution Echelle Spectrometer (HIRES, Vogt et al., 1994) on the Keck I Telescope. We collected 74 measurements of K2-3 from 2015 Feb 4 to 2017 Apr 11. These spectra were taken with an iodine cell and the C2 decker; a template spectrum was also taken in order to calibrate the wavelength and estimate the radial velocity uncertainty. On average, measurements were collected with an exposure time of 1600s in order to reach a signal-to-noise (SNR)

ratio of 87/pixel (80k counts on the HIRES exposure meter). The observations and data reduction followed the California Planet Search method described in Howard et al. (2010).

An additional 360 Doppler measurements were used in the following K2-3 analysis. We include 31 spectra collected with PFS (Dai et al., 2016), 132 spectra collected with HARPS, and 197 spectra collected with HARPS-N (Almenara et al., 2015; Damasso et al., 2018). Our HIRES measurements have an average uncertainty of 1.7 m s^{-1}, whereas the PFS, HARPS, and HARPS-N measurements have average uncertainties of 2.5 m s^{-1}, 2.1 m s^{-1}, and 2.0 m s^{-1} respectively.

11.3.2 Stellar Activity Analysis

We first examined the potential effects of stellar activity by measuring the strength of the Calcium II H and K spectral lines in our HIRES measurements (Isaacson and Fischer, 2010). We calculated the correlation coefficient and probability value (p-value) for the $S_{\rm HK}$ and radial velocity data for each season of data collection. Then, we examined their periodograms for potential similarities. We also analyzed ground-based photometry to determine the stellar rotation period. Finally, we modeled the radial velocity data with Gaussian processes trained on the photometry to remove correlated stellar activity.

We investigate the possible correlation between $S_{\rm HK}$ and radial velocity values for K2-3 as the stellar rotation period found from K2 photometry (40 $\pm$ 10 days; Dai et al., 2016) is near planet d's orbital period. Dai et al. (2016) and Damasso et al. (2018)

find the planet signal to be degenerate with the stellar rotation signal. The correlation coefficient is -0.0169 and p-value is 0.8869 for the full dataset (using scipy, Jones et al., 2001), suggesting that the radial velocities are not correlated with the stellar activity as measured by $S_{\rm HK}$. We also do not find any similar significant peaks in the periodograms (Figure 11.1).

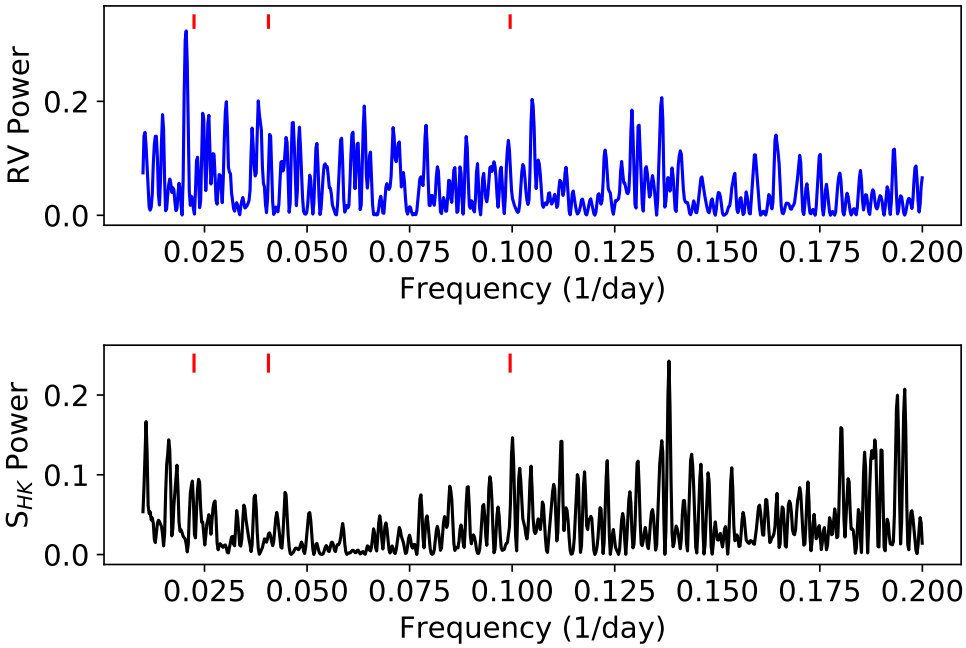

Figure 11.1: K2-3: periodograms of the radial velocity data (top) and $S_{\rm HK}$ (bottom). The three planet periods are shown by red tick marks at the top of the figures. The two periodograms do not have similar prominent peaks. Although the planet periods are not all visible in the radial velocity periodogram due to their meter-per-second amplitudes, we are able to detangle the planet signals in the radial velocity data by constraining the periods and conjunction times from K2 and Spitzer transits.

$S_{\rm HK}$ may be a poor activity indicator for M dwarf stars. To better characterize the possible rotation signal of K2-3, we analyzed photometry from the Evryscope. The Evryscope is an array of 24 61mm telescopes together imaging 8000 square degrees of

sky every two minutes (Law et al., 2015). From its 2015 installation at CTIO in Chile to the publication of this work in Kosiarek et al. (2019b), the Evryscope observed on over 500 clear nights, tracking the sky for 2 hours at a time before "ratcheting" back and continuing observations, for an average of ∼6 hours of continuous monitoring each night. The Evryscope observes in Sloan-g' at a resolution of 13"/pixel. High-cadence photometry of K2-3 is included in the Evryscope light curve database from January 2016 to March 2018 (Figure 11.2). Because K2-3 is in the Northernmost region of the Evryscope field of view, the coverage of the target is limited each year, resulting in a total of 10^4 epochs; most Southern stars are observed with 4–6× more points.

Evryscope light curves are generated using a custom pipeline. The Evryscope image archive contains 2.5 million raw images, ∼250TB of total data. Each image, consisting of a 30MPix FITS file from one camera, is dark-subtracted, flat-fielded and then astrometrically calibrated using a custom wide-field solver. Large-scale background gradients are removed, and forced-aperture photometry is then extracted based on known source positions in a reference catalog. Light curves are generated for approximately 15 million sources across the Southern sky by differential photometry in small sky regions using carefully-selected reference stars; residual systematics are removed using two iterations of the SysRem detrending algorithm. For 10th magnitude stars, this process results in ≈1% photometric stability at 2-minute cadence when measured in multiple-year lightcurves over all sky conditions; co-adding produces improved precisions, down to ∼6 mmag.

Evryscope collected 9931 epochs of K2-3 at 2 minute cadence in Sloan-g' from

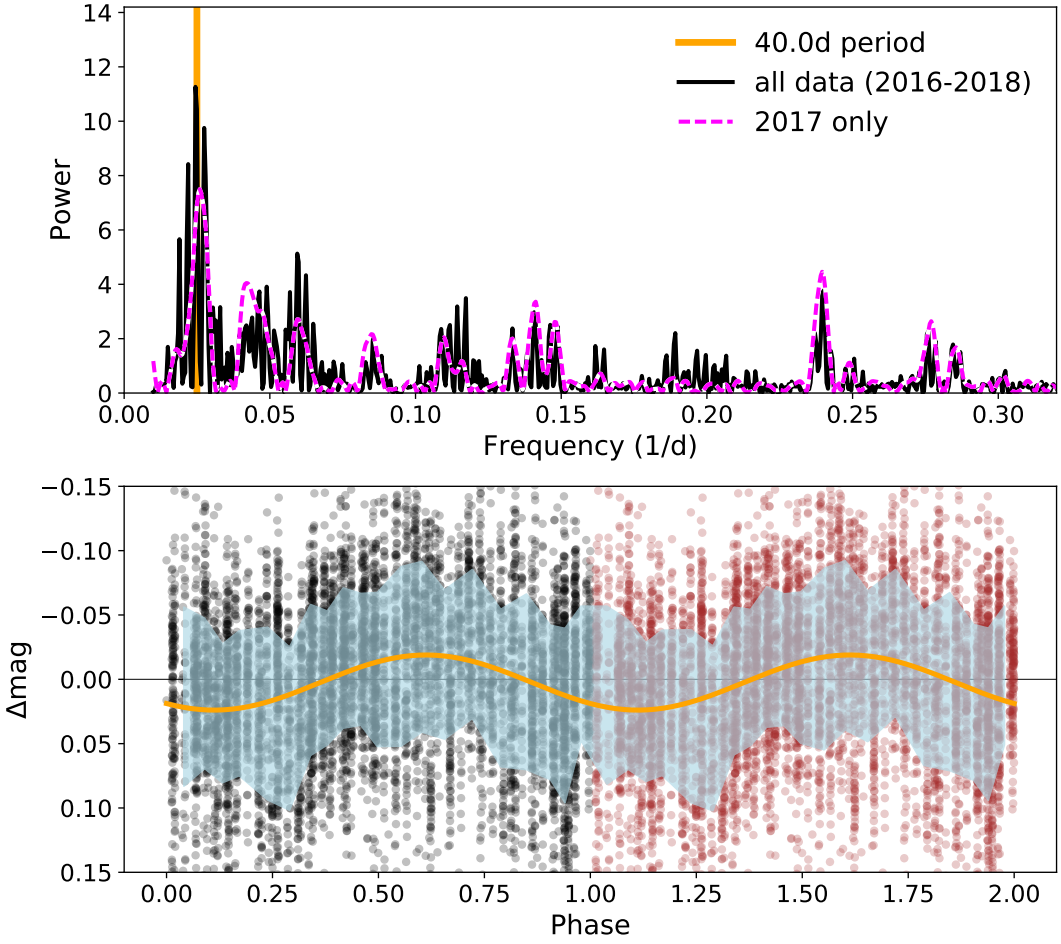

Figure 11.2: Evryscope photometry of K2-3, consisting of 9931 epochs at 2 minute cadence in Sloan-g' from January 2016 to March 2018. Top panel: The Lomb-Scargle (LS) periodogram of K2-3 displays significant power around 40 days (orange vertical line). A purple dashed line shows the power of only the 2017 photometry as a secondary confirmation. Bottom panel: Phase-folded lightcurve folded over 40 days. The phase is repeated to guide the eye, and points are binned to 8-minute cadence to improve precision on this relatively faint Evryscope target. The 1-σ region about the mean of the phased lightcurve is shown (light blue area), along with a 40 d sinusoid with a characteristic amplitude of 0.02 mags (orange curve).

January 2016 to March 2018. The data were analyzed using a Lomb-Scargle periodogram to determine the likely rotation period of K2-3 (Figure 11.2). The highest peak is at 40.0 days, but power from the central peak is split due to the inter-year window function, verified by injecting similar signals to K2-3 and other nearby stars. An alias of the 40.0 day signal exists at reduced power near 20 days. The periodogram for only the 2017 photometry produces a peak signal of 38 days. A signature of evolving starspot activity due to differential rotation near 40 days may explain this difference. The 40.0 day period shows a sinusoidal variation with a 0.02 magnitude variation. Therefore, we infer the rotation period of K2-3 to be 40 $\pm$ 2 days from the Evryscope data. Both the 2017 and the all-data rotation periods agree with the estimate from K2 data, within measurement errors. We use the Evryscope photometry to inform our Gaussian process priors in the radial velocity fit.

11.3.3 Radial Velocity Fit

For our radial velocity fit, we adopt the planet orbital periods and times of conjunction from our Spitzer analysis (Section 3, Kosiarek et al., 2019b). We used a Gaussian process to model the correlated noise associated with the stellar activity in our radial velocity fit. We ran our Gaussian process analysis on the photometry from Evryscope (ES) and find $\gamma_{ES} = 11.61 \pm 0.01$ mag, $\sigma_{ES} = 0.017^{+0.004}_{-0.003}$ mag, $\eta_1 = 0.03 \pm 0.01$ mag, $\eta_2 = 44.57^{+12.58}_{-16.23}$ days, $\eta_3 = 37.80^{+1.77}_{-2.04}$ days, $\eta_4 = 0.47 \pm 0.05$. This stellar rotation period (η_3) is consistent with the results of our periodogram analysis in subsection 9.4.3 to within 2-σ.

We then perform our radial velocity fit including a Gaussian process modeled as a sum of four quasi-periodic kernels (Equation 7.1), one for HIRES, HARPS, HARPS-N and PFS, as described above for GJ 3470. Our Gaussian process hyperparameter priors are as follows: η_1 is left as a free parameter as light curve amplitude cannot be directly translated to radial velocity amplitude. To construct priors on η_2, η_3, and η_4, we use a kernel density estimate of the Evryscope photometry posteriors.

After running an initial radial velocity fit including only three circular Keplerian planet signals, we investigated additional models including an acceleration term, curvature term, and planet eccentricity. The fit including an additional term for acceleration, curvature, and eccentricity had ΔAIC of -2.17, -2.22, and -2.92 respectively; none of these justified the additional parameter. Table 11.2 shows the MCMC priors, orbital parameters, and statistics for the Gaussian process model of K2-3. Our radial velocity fit is shown in Figure 11.3 and the best fit curves for each planet are shown in Figure 11.4.

From our Gaussian process fit, we find that the semi-amplitude of the signal from planet d is consistent with 0 to 1-σ. It is possible that this planet has a small semi-amplitude ($K_d << 1$ m s^{-1}) and we were unable to detect it. Alternatively, as the period of planet d ($P_d = 44.56$ days) is near the stellar rotation period ($\eta_3 \approx 40$ days), it is possible that the signal of planet d is indistinguishable from the stellar activity signal. Further work is needed to distinguish between the two possibilities and determine the mass of planet d.

Our mass measurements of K2-3 b and c are within 1-σ of Almenara et al. (2015) and Dai et al. (2016). Our mass measurement of K2-3 d is within 3-σ of Dai et al.

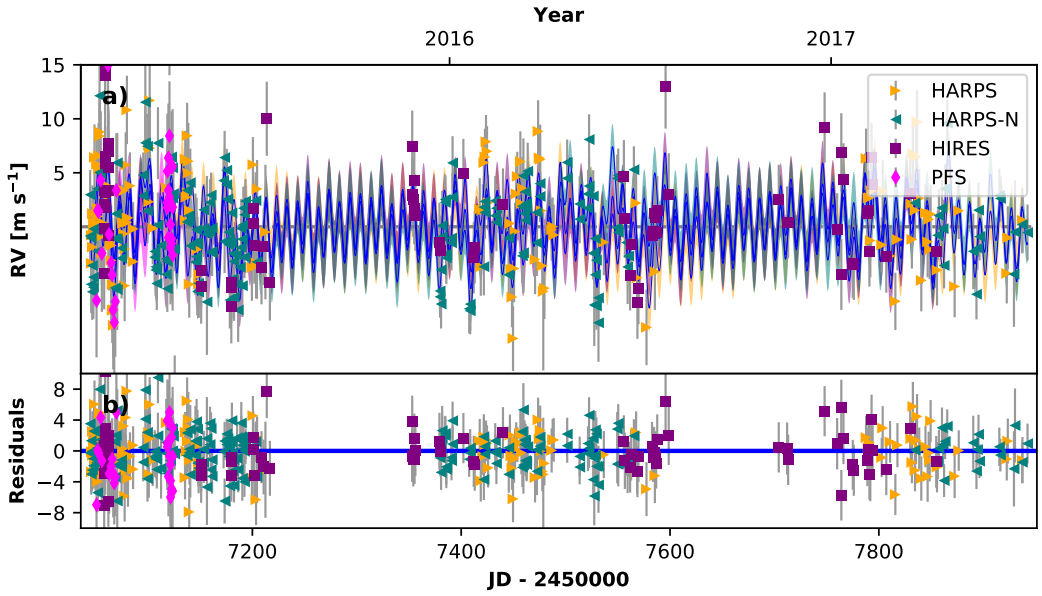

Figure 11.3: Best-fit three-planet Keplerian orbital model for K2-3 including a Gaussian process. The thin blue line is the best fit three-planet model with the mean Gaussian process model; the colored area surrounding this line includes the 1-σ maximum likelihood Gaussian process uncertainties. We add in quadrature the jitter terms listed in Table 11.2 with the measurement uncertainties for the data. **b)** Residuals to the best fit three-planet model.

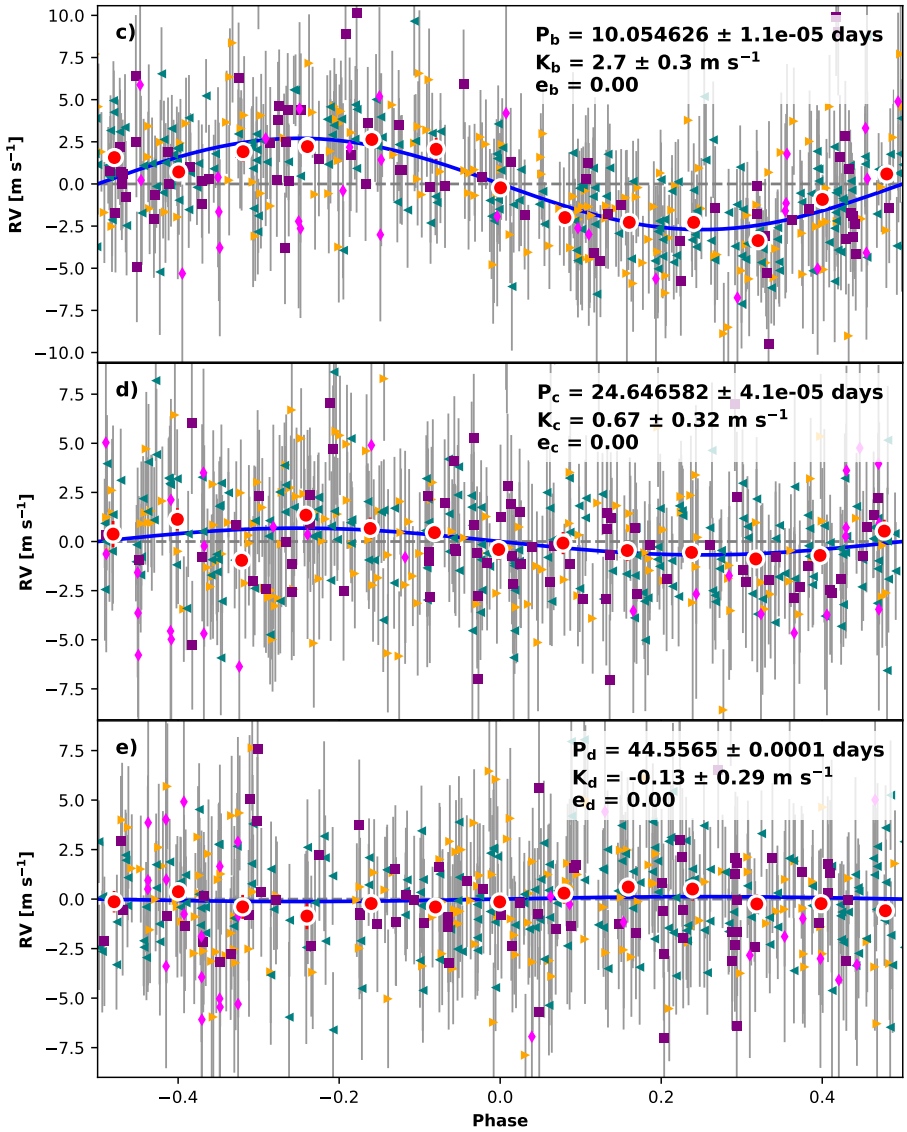

Figure 11.4: Best-fit three-planet Keplerian orbital model for K2-3 phase-folded to each planet orbital period. See Figure 11.3 for the full dataset. The thin blue line is the best fit three-planet model with the mean Gaussian process model. We add in quadrature the jitter terms listed in Table 11.2 with the measurement uncertainties for the data. **c), d), e)** Radial velocities phase-folded to the ephemeris of planet b, c, d. The Keplerian orbital models for all other planets have been subtracted. Red circles are the same velocities binned in 0.08 units of orbital phase.

Parameter	3 Planet Fit	Units
Gaussian Priors		
$T\mathrm{conj_b}$	$2456813.41843 \pm 0.00039$	JD
P_b	$10.054626 \pm 1e-05$	days
$T\mathrm{conj_c}$	$2456812.28013 \pm 0.00095$	JD
P_c	$24.646582 \pm 3.9e-05$	days
$T\mathrm{conj_d}$	$2456826.22347 \pm 0.00053$	JD
P_d	$44.556456 \pm 9.7e-05$	days
$\eta_{1,all}$	[0,100]	m s^{-1}
η_2	$44.57^{+12.58}_{-16.23}$	days
η_3	$37.80^{+1.77}_{-2.04}$	days
η_4	0.47 ± 0.05	
Orbital Parameters		
P_b	$10.054626^{+1e-05}_{-1.1e-05}$	days
$T\mathrm{conj_b}$	$2456813.41843 \pm 0.00041$	JD
e_b	$\equiv 0.0$	
ω_b	$\equiv 0.0$	radians
K_b	$2.72^{+0.29}_{-0.3}$	m s^{-1}
M_b	$6.48^{+0.99}_{-0.93}$	$M_\oplus$
ρ_b	$3.70^{+1.67}_{-1.08}$	g cm^{-3}
P_c	$24.646582^{+4.1e-05}_{-4e-05}$	days
$T\mathrm{conj_c}$	$2456812.28018^{+0.00098}_{-0.001}$	JD
e_c	$\equiv 0.0$	
ω_c	$\equiv 0.0$	radians
K_c	0.67 ± 0.32	m s^{-1}
M_c	$2.14^{+1.08}_{-1.04}$	$M_\oplus$
ρ_c	$2.98^{+1.96}_{-1.50}$	g cm^{-3}
P_d	$44.55646^{+0.00011}_{-0.0001}$	days
$T\mathrm{conj_d}$	$2456826.22346 \pm 0.00056$	JD
e_d	$\equiv 0.0$	
ω_d	$\equiv 0.0$	radians
K_d	$-0.13^{+0.28}_{-0.31}$	m s^{-1}
M_d	$-0.50^{+1.10}_{-1.20}$	$M_\oplus$
ρ_d	$-0.98^{+2.20}_{-2.83}$	g cm^{-3}
K_d (3-σ upper)	0.71	m s^{-1}
M_d (3-σ upper)	2.80	$M_\oplus$
ρ_d (3-σ upper)	5.62	g cm^{-3}

Table 11.2: K2-3 Radial Velocity MCMC Priors and Posteriors Part 1

Parameter	3 Planet Fit	Units
Other Parameters		
$\gamma_{\rm PFS}$	-1.3 ± 2.2	m s^{-1}
$\gamma_{\rm HIRES}$	$-2.98^{+0.97}_{-1.0}$	m s^{-1}
$\gamma_{\rm HARPS-N}$	$0.53^{+0.71}_{-0.74}$	m s^{-1}
$\gamma_{\rm HARPS}$	$-0.59^{+0.69}_{-0.73}$	m s^{-1}
$\dot{\gamma}$	$\equiv 0.0$	m s^{-1} day^{-1}
$\ddot{\gamma}$	$\equiv 0.0$	m s^{-1} day^{-2}
$\sigma_{\rm PFS}$	$4.85^{+1.0}_{-0.88}$	m s^{-1}
$\sigma_{\rm HIRES}$	$2.98^{+0.47}_{-0.42}$	m s^{-1}
$\sigma_{\rm HARPS-N}$	$1.61^{+0.26}_{-0.25}$	m s^{-1}
$\sigma_{\rm HARPS}$	$2.06^{+0.34}_{-0.32}$	m s^{-1}
$\eta_{1,PFS}$	$4.75^{+3.72}_{-2.58}$	m s^{-1}
$\eta_{1,HIRES}$	$3.21^{+0.84}_{-0.73}$	m s^{-1}
$\eta_{1,HARPS}$	$3.04^{+0.64}_{-0.53}$	m s^{-1}
$\eta_{1,HARPS-N}$	$3.07^{+0.61}_{-0.48}$	m s^{-1}
η_2	$62.25^{+10.78}_{-9.84}$	days
η_3	$39.16^{+0.88}_{-0.96}$	days
η_4	$0.41^{+0.05}_{-0.04}$	

Table 11.3: K2-3 Radial Velocity MCMC Priors and Posteriors Part 2

(2016) and 4-σ of Almenara et al. (2015). Our measurements of K2-3 b is within 1-σ of Damasso et al. (2018), K2-3 c is within 2-σ, and K2-3 d is within 2-σ of their RV fit and within 3-σ of their injection/recovery tests. We have improved the precision of the mass measurement of these planets compared to previous measurements. However, due to the potential stellar activity contamination, use caution with the measurement for K2-3 d.

In terms of the planet compositions, K2-3 b and c both have a bulk density consistent with a mixture of silicates and water. As a water planet is an unlikely product of planet formation, they likely have iron-silicate cores with a small volatile envelope. Assuming an Earth-like core, K2-3 b and c both have about 0.5% H/He by mass (Lopez and Fortney, 2014). However, K2-3 c is also consistent with no volatile atmosphere given

a sufficient amount of lighter material in the core; the 3-σ mass measurement is consistent with an Earth-like composition. K2-3 d is potentially the lightest planet compared to others of similar radii; it needs substantial volatiles to explain the non-detection. The two main interpretations are: (1) the planet is sufficiently low-mass to not detect its signal, requiring a significant volatile percentage, or (2) we have not adequately accounted for the stellar activity radial velocity signal in this analysis; therefore, the actual mass of planet d is higher than listed here.

11.4 Transmission Spectra Discussion

K2-3 d and the K2-3 UV emission will be observed with HST in cycles 24 and 25 (GO 14682, GO 15110). It is important to characterize potential atmospheric targets to determine precise mass and surface gravity measurements, as these parameters will affect the interpretation of future transmission spectroscopy observations.

We simulated model transmission spectra for the K2-3 planet system using ExoTransmit (Kempton et al., 2017) to examine their possible atmospheric compositions (Figure 11.5). Two spectra were created for planet b and c according to the 1-σ lower and upper bounds on the mass. Two spectra were created for planet d according to the upper 1-σ and upper 2-σ mass, as the mass measurement is consistent with zero. Our assumptions include no clouds, chemical equilibrium, a 100 M/H ratio, and the 1 bar radius equals the transit radius.

The transit depth was adjusted to match the K2 (Crossfield et al., 2015) and

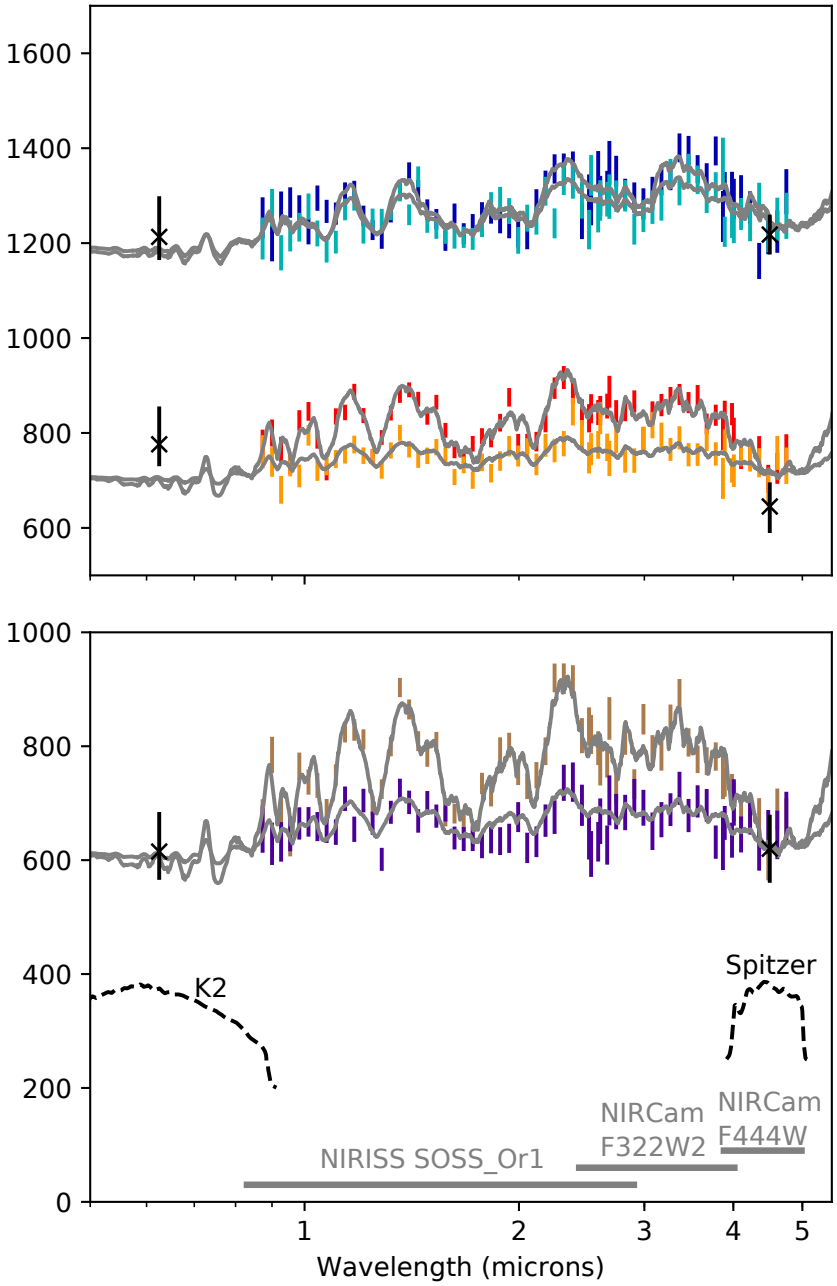

Figure 11.5: Simulated transmission spectra (grey) of K2-3 b (blue/green, top) and c (red/orange, middle) for their 1-σ low mass and high mass cases and spectra for K2-3 d (brown/purple, bottom) for the upper 1-σ and 2-σ cases. Error bars refer to simulated JWST observations with PandExo (Batalha et al., 2017b). K2 and Spitzer datapoints and bandpasses are shown in black. JWST instrument wavelength ranges are shown in grey.

Spitzer (Kosiarek et al., 2019b) transit depths. Simulated JWST observations and error bars are superimposed on top of the spectra using PandExo[1] (Greene et al., 2016; Batalha et al., 2017b). We simulated one transit for each planet for each of three instrument modes: NIRCam F332W2, NIRCam F444W, and NIRISS SOSS_Or1. We used the Phoenix grid models to simulate a stellar spectrum with a magnitude of 8.56 K-mag, temperature of 3890 K, metallicity of 0.3, and log(g) of 4.8. For each transit, we included a baseline of equal time to the transit time, zero noise floor, and resolution of R = 35.

For K2-3 b, the absorption features would be observable for a true mass value within 1-σ of our mass measurement; the light and dark blue simulated datapoints are both inconsistent with a flat spectra. From this, K2-3 b is particularly a good target for future atmospheric study. For K2-3 c, the absorption features would be easily observable for a mass on the lower 1-σ side of our measurement, but would be much more difficult for the higher-mass case. Lastly, K2-3 d would have distinguishable features as long as the mass is lower than our 2-σ upper limit.

The Spitzer transit depths for K2-3 c and d are quite similar (Kosiarek et al., 2019b) although their K2 transit depths are considerably offset. Beichman et al. (2016) also finds similar Spitzer transit depth for K2-3 c and d. We were unable to create a model spectra for planet c that was consistent with both the K2 and Spitzer data to 1-σ. However, this model did not include clouds, which could improve the fit of the model to the data (Sing et al., 2016).

Transmission spectra can help to constrain a planet's mass further as the scale

[1]We present a wrapper for easier PandExo simulations: https://github.com/iancrossfield/jwstprep

height depends on the planet's gravity (de Wit and Seager, 2013). However, one must be careful as there are significant degeneracies between the effects of mass and composition for small planets (Batalha et al., 2017a). With the mass of the planets constrained here through the radial velocity method, further constraints can be put on the atmospheric composition from the transmission spectra.

These planets are example training cases for future TESS planets. TESS will find a large sample of bright systems around nearby stars (Ricker et al., 2014; Sullivan et al., 2015; Ballard, 2019). These types of planets will be ideal for JWST atmospheric observations due to their bright host stars. Prior to transmission spectroscopy observations, these systems will need to be followed-up in a similar method as described in this work to determine the planet masses in order to correctly interpret the spectra.

11.5 Conclusion

Photometric monitoring of planet-hosting stars is important to determine the stellar rotation period and spot modulation to therefore separate the stellar activity from the planet-induced radial velocity signals. This is especially important for planetary systems with low-amplitude radial velocity signals as these signals may be hidden by stellar activity. We used a Gaussian process trained on our photometry to account for this stellar activity.

$S_{\rm HK}$ was not be a good indicator for stellar activity in this M dwarf star. Although there was no radial velocity correlation with $S_{\rm HK}$, our Evryscope photometry

showed clear periodicity near the orbital period of K2-3 d; it is important to account for this activity to measure an accurate mass of planet d. Photometry and Hα could be useful diagnostics for M dwarf stellar rotation periods instead of $S_{\rm HK}$ (Newton et al., 2017; Robertson et al., 2015; Damasso et al., 2018).

We measured the masses of K2-3 b and K2-3 c to be $6.48^{+0.99}_{-0.93}$ $M_\oplus$ and $2.14^{+1.08}_{-1.04}$ $M_\oplus$, respectively. We determined an upper limit on the mass of K2-3 d of 2.80 $M_\oplus$. With such a low mass, this planet is consistent with having a substantial volatile envelope which decreases its chance for habitability. As such, K2-3 likely hosts three sub-Neptune planets instead of super-Earth planets. These planets present an interesting case for transmission spectroscopy observations of temperate sub-Neptunes.

Chapter 12

HD 97658

12.1 Introduction

HD 97658 b is a 2.4 $R_\oplus$ sub-Neptune discovered with Keck-HIRES in the NASA-UC Eta-Earth Survey (Howard et al., 2011), and later found to transit by Dragomir et al. (2013) using the MOST telescope. It orbits a bright ($V = 7.7$) K1 star with a 9.5 day period, and was ranked the 6th best confirmed planet for transmission spectroscopy with $R_\mathrm{p} < 5\ R_\oplus$ in Rodriguez et al. (2017).

HD 97658 b was monitored by the Spitzer Space Telescope; Van Grootel et al. (2014) produced a global Bayesian analysis result combing the Spitzer, MOST, and Keck-HIRES data. They found that HD 97658 b has an intermediate density of $3.90^{+0.70}_{-0.61}$ g cm^{-3}, indicating a rocky composition of at least 60% by mass, around 0%–40% of water and ice, and a H-He dominated envelope of at most 2% by mass.

Guo et al. (2020) describes the characterization of HD 97658 b through HST

transmission spectroscopy measurements. Transmission spectrocopy analysis benefits from a precise planetary mass measurement therefore we performed a radial velocity analysis on the HD 98657 system including additional HIRES data to derive an updated mass of HD 97658 b.

12.2 Radial Velocity Analysis

12.2.1 Data Collection

Since January 1997 we have collected 553 radial velocity measurements with the High Resolution Echelle Spectrometer (HIRES, Vogt et al., 1994) on the Keck I Telescope on Maunakea and 215 measurements with the Levy spectrograph on the Automated Planet Finder at Lick Observatory (APF, Radovan et al., 2014, Vogt et al., 2014). These data were all collected through an iodine cell for wavelength calibration and point spread function reference (Butler et al., 1996). One set of iodine-free spectra were collected with each instrument to use as a model of the intrinsic stellar spectrum. The HIRES data were often taken in sets of three due to the short ∼2 minute exposures to mitigate the effects of stellar oscillations, this was not necessary for the APF due to the smaller aperture and longer exposure times (∼10-20 minute exposures). The HIRES data from January 2005 to August 2010 were previously analyzed in the discovery paper of HD 97658 b (Howard et al., 2011). The data reduction and analysis followed the California Planet Search method described in Howard et al. (2010).

12.2.2 Stellar Activity Analysis

We first investigated the star for signs of stellar activity by examining the Calcium H and K lines (S_{HK}, Isaacson and Fischer (2010), Figure 12.1) in the HIRES and APF data. There is a clear periodicity in both the S_{HK} and the radial velocity data around 3500 days in the HIRES dataset (Figure 12.2). The APF data does not have a long enough baseline to detect such a long signal. In addition, we compare this long term variation in S_{HK} and radial velocity signals with the brightness and color variation of HD 97658 which was measured with the Fairborn T8 0.80m automatic photoelectric telescope (Henry, 1999). As is shown in Figure 12.1, there is a clear correlation in the variations seen in radial velocities, stellar activity data, stellar brightness, and stellar color. This relation implies that the long-term radial velocity variation is caused by stellar activity. The length of the signal (9.6 yr) indicates that it is likely the star's magnetic activity cycle (slightly shorter than our Sun's eleven-year cycle).

12.2.3 Radial Velocity Fit

We model this system in `radvel` as a two-Keplerian system for planet b and the stellar activity. We include priors on the transit parameters of planet b from Van Grootel et al. (2014). We incorporate this stellar activity signal at around 3500 days into our radial velocity fit as an additional Keplerian signal because it has a sinusoidal shape and only two cycles of this signal are captured by the data. We use a Gaussian prior on the period (3424±41 days) and reference phase of this signal (2457372±21 BJD) from a `radvel` 1-Keplerian fit of the HIRES S_{HK} data. Our radial velocity fit is shown

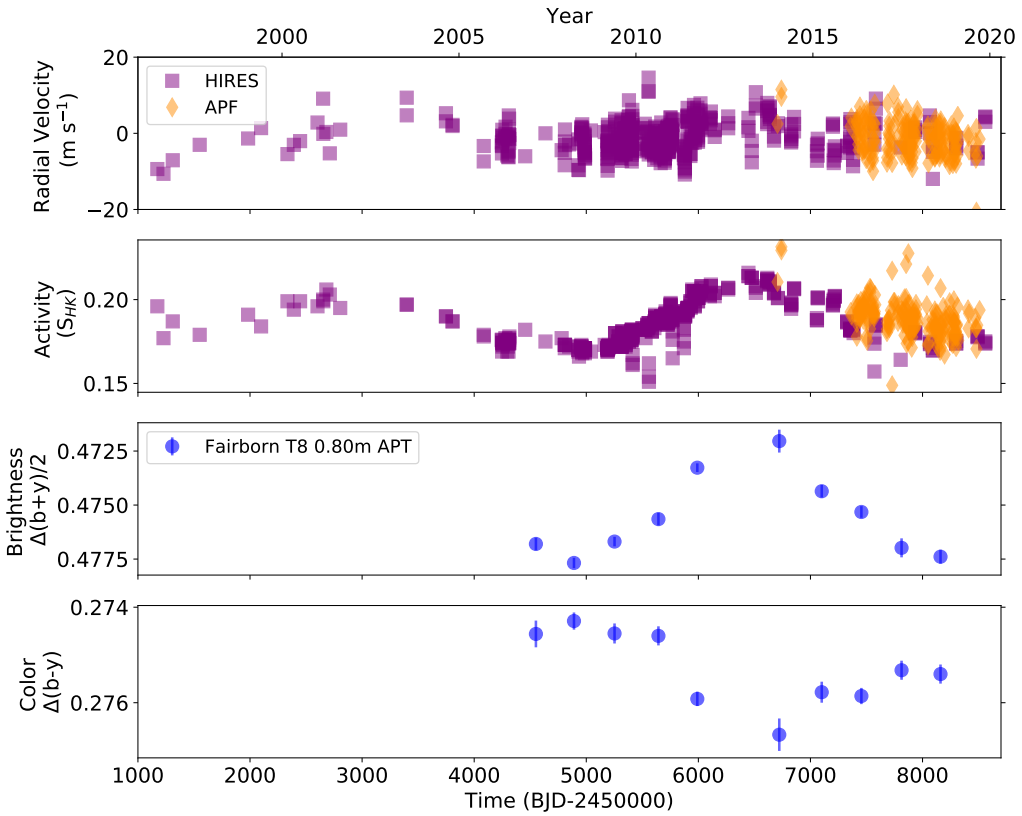

Figure 12.1: Time series of our radial velocity and Calcium H and K activity (S_{HK}) data from HIRES and APF, and photometry from the Fairborn T8 0.80m APT including both brightness and color information. There is a clear variation in the radial velocity data matched by the activity data, brightness, and color all without a phase offset. This relation implies that the long-term radial velocity variation is stellar activity.

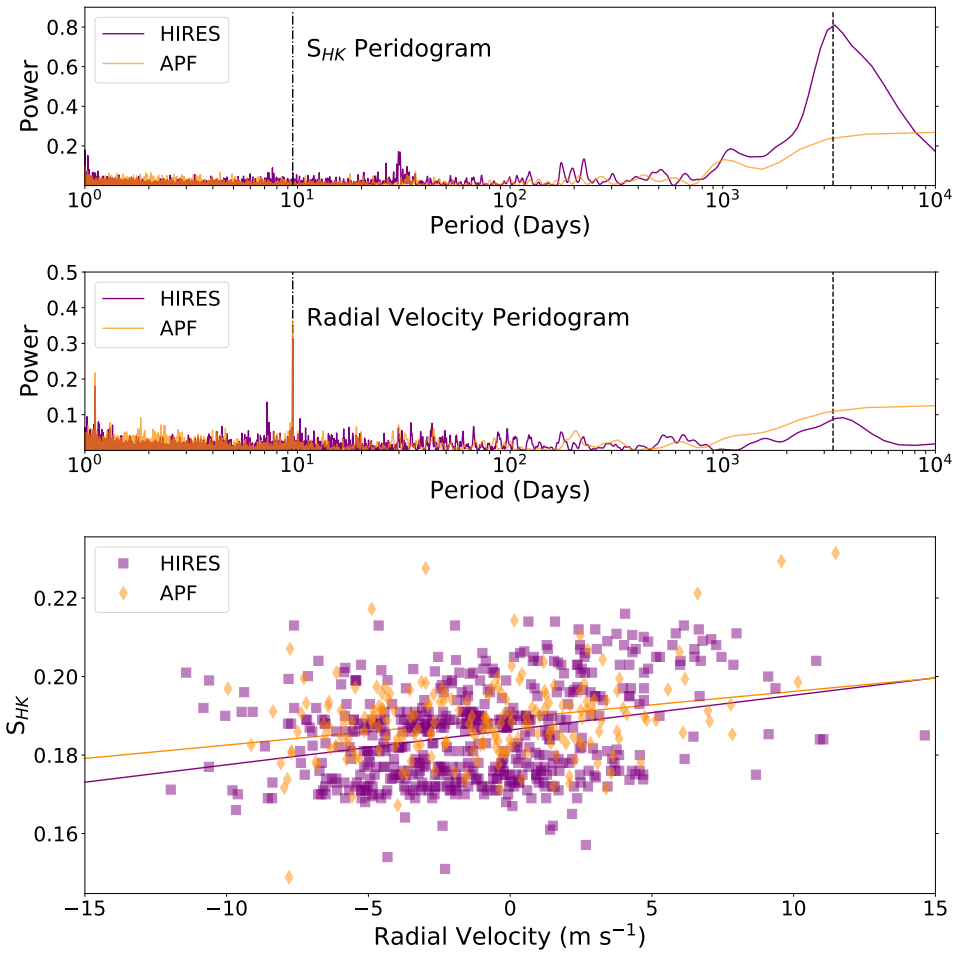

Figure 12.2: Periodograms of S_{HK} (top) and radial velocity (middle), and S_{HK} vs. radial velocity (bottom). In both periodograms, the stellar activity cycle (Figure 12.1, $\sim$ 3500 days) is represented by a dashed line and the planet's orbital period (9.49 days) is represented by a dash-dot line. There is a strong radial velocity signal and S_{HK} signal at the stellar activity cycle timescale in the HIRES data. There is a correlation between the S_{HK} and radial velocity data in both datasets, shown as the solid lines in the bottom panel.

in Figure 12.3, and the output parameters are listed in Table 12.1. Note the planet mass is calculated assuming our best-fit inclination ($i = 89.6$) with the HST/WFC3 dataset, which shows $\sin(i) \approx 1$.

We also test a non-zero planet eccentricity for completeness; however the inclusion of the additional parameters is not favored by the AIC. The resulting eccentricity is small, consistent with zero to two sigma (e_b=$0.030^{+0.034}_{-0.021}$), and results in consistent planet parameters to the circular case. Therefore we adopt the circular fit results. We also test including a Gaussian process to model the stellar activity signal with the hyperparameters constrained from a fit of the HIRES S_{HK} data. The results are consistent with the Keplerian fit; the baseline covers only two cycles of the activity therefore the deviation from a simple sinusoid is small. Since the fit has consistent posteriors, the additional parameters needed for the Gaussian process fit do not seem warranted and we present the Keplerian fit as our final result.

12.3 Conclusion

We improved the precision on the mass of HD 97658 b using additional HIRES and APF radial velocity data in order to derive a precise surface gravity for atmospheric transmission spectroscopy measurements. We find a mass of $M_b = 7.81^{+0.55}_{-0.44}$ $M_\oplus$ and density of $\rho_b = 3.78^{+0.61}_{-0.51}$ g cm^{-3}.

We detect a coherent stellar signal present in our radial velocity data, Calcium II H & K lines, stellar brightness, and b-y color. This signal has a periodicity of 9.6

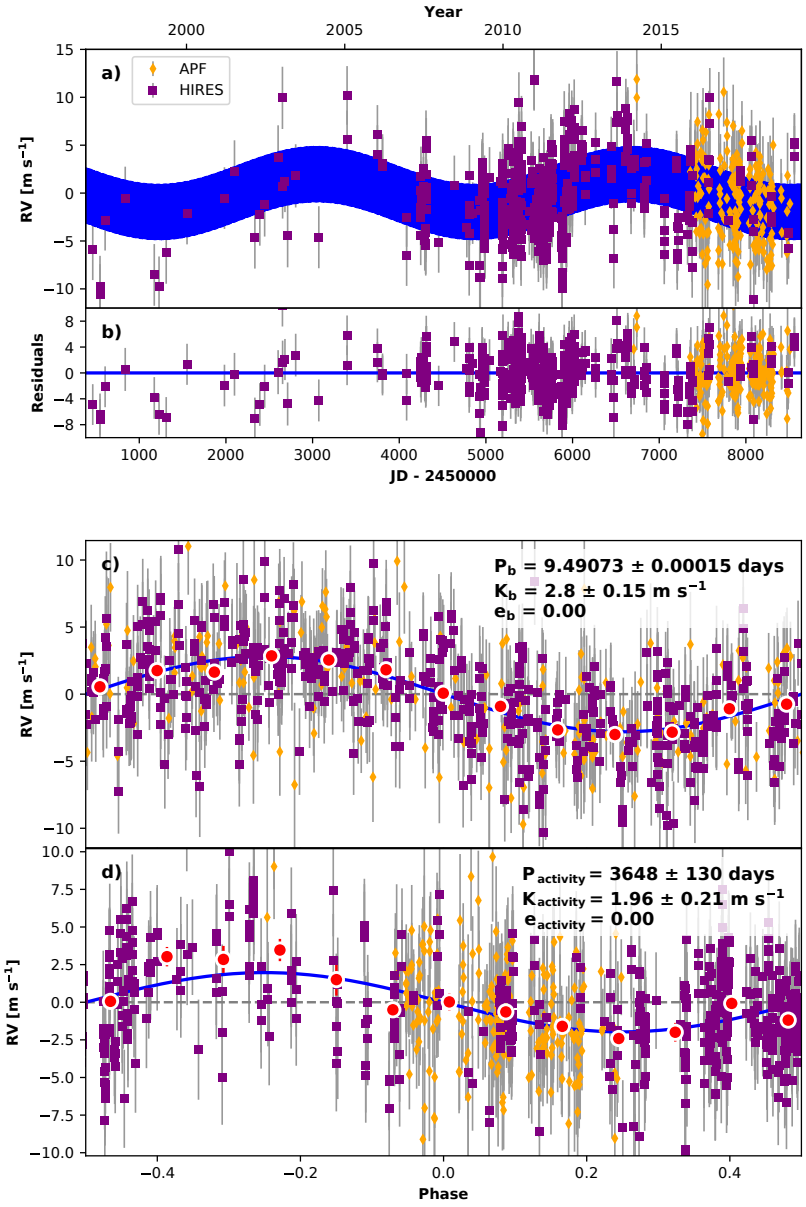

Figure 12.3: Best-fit one-planet Keplerian orbital model for HD 97658 including stellar activity (blue line). We add in quadrature the jitter terms listed in Table 12.1 with the measurement uncertainties for the data. **b)** Residuals to the best fit model. **c)** Radial velocities phase-folded to the ephemeris of planet b. The Keplerian orbital model for the stellar activity has been subtracted. Red circles are the same velocities binned in 0.08 units of orbital phase. **d)** Radial velocities phase-folded to the ephemeris of the stellar activity.

Parameter	Name (units)	Value
P_b	Period (days)	9.49073 ± 0.00015
$T\mathrm{conj}_\mathrm{b}$	Time of conjunction ($\mathrm{BJD_{TDB}}$)	2456361.805 ± 0.0006
e_b	Eccentricity	$\equiv 0.0$
ω_b	Argument of periapse (radians)	$\equiv 0.0$
K_b	Semi-amplitude (m s^{-1})	2.81 ± 0.15
M_b	Mass ($\mathrm{M_\oplus}$)	$7.81^{+0.55}_{-0.44}$
ρ_b	Density (g cm^{-3})	$3.78^{+0.61}_{-0.51}$
P_activity	Period (days)	3652^{+130}_{-120}
$T\mathrm{conj}_\mathrm{activity}$	Reference Time ($\mathrm{BJD_{TDB}}$)	2457605^{+100}_{-89}
e_activity	Eccentricity	$\equiv 0.0$
ω_activity	Argument of periapse (radians)	$\equiv 0.0$
K_activity	Semi-amplitude (m s^{-1})	1.96 ± 0.21
γ_HIRES	Mean center-of-mass velocity (m s^{-1})	-0.85 ± 0.17
γ_APF	Mean center-of-mass velocity (m s^{-1})	$-0.42^{+0.33}_{-0.34}$
$\dot{\gamma}$	Linear acceleration (m s^{-1} day^{-1})	$\equiv 0.0$
$\ddot{\gamma}$	Quadratic acceleration (m s^{-1} day^{-2})	$\equiv 0.0$
σ_HIRES	Jitter (m s^{-1})	$2.93^{+0.11}_{-0.1}$
σ_APF	Jitter (m s^{-1})	$1.3^{+0.31}_{-0.35}$

Table 12.1: HD 97658 Radial Velocity Parameters

years, therefore we attribute it to the star's magnetic cycle. We include this activity cycle in our radial velocity fit as a second sinuosoid to improve our determination of the planet parameters.

Chapter 13

GJ 9827

13.1 Abstract

GJ 9827 is a bright, nearby star that hosts three super-Earths discovered by K2 that are well suited for atmospheric characterization. Through a multi-year high-cadence observing campaign with Keck/HIRES, we improved the planets' mass measurements in anticipation of Hubble Space Telescope transmission spectroscopy. We modeled activity-induced radial velocity signals with a Gaussian process informed by the Calcium II H&K lines in order to more accurately model the effect of stellar noise on our data. We measured planet masses of M_b=4.87 $\pm$ 0.37 $M_\oplus$, M_c=1.92 $\pm$ 0.49 $M_\oplus$, and M_d=3.42 $\pm$ 0.62 $M_\oplus$. We investigated the planets' compositions through comparing their masses and radii to a range of interior models: GJ 9827 b and GJ 9827 c are both consistent with a 50/50 rock-iron composition, and GJ 9827 d requires additional volatiles.

13.2 Introduction

GJ 9827 (K2-135) is a bright (V = 10.3 mag, K = 7.2 mag), nearby (distance = 30 pc) K6 dwarf star hosting three planets discovered in K2 Campaign 12 (Niraula et al., 2017; Rodriguez et al., 2018). Planets b and c orbit near a 3:1 resonance at 1.2 days and 3.6 days, with planet d at 6.2 days. These three planets span the gap seen in the radius distribution of small planets (Fulton et al., 2017) sized at 1.529±0.058 $R_\oplus$, 1.201±0.046 $R_\oplus$, and 1.955±0.075 $R_\oplus$ respectively. Niraula et al. (2017) additionally collected 7 radial velocity observations with FIES to vet the system and to derive stellar parameters.

The mass of planet b was first determined with radial velocity observations from PFS by Teske et al. (2018) (M_b ∼8 $M_\oplus$), who placed upper limits on planets c and d (M_c <2.5 $M_\oplus$, M_d <5.6 $M_\oplus$). Through additional measurements with HARPS and HARPS-N, Prieto-Arranz et al. (2018) determined the masses of all three planets (M_b=3.74±0.50 $M_\oplus$, M_c=1.47±0.59 $M_\oplus$, and M_d=2.38±0.71 $M_\oplus$). The masses of planets b and d were further refined by Rice et al. (2019) with new HARPS-N radial velocity measurements and a Gaussian process informed by the K2 light curve (M_b=4.91±0.49 $M_\oplus$ and M_d=4.04±0.84 $M_\oplus$). Both Prieto-Arranz et al. (2018) and Rice et al. (2019) discuss how the inner planets have a high density and the outer planet has a lower density, suggesting that photoevaporation or migration could have played a role in the evolution of this system; we discuss this possibility further in section 13.4 and chapter 16.

13.3 Radial Velocity Analysis

13.3.1 Data Collection

We obtained 92 measurements of GJ 9827 with HIRES between 2017 September 22 and 2020 January 8. These data were collected with the C2 decker (14″ x 0.861″, resolution = 50k) with a typical signal-to-noise radio (SNR) of 200/pixel (250k on the exposure meter, median exposure time of 18.5 minutes). We also collected a higher resolution template observation with the B3 decker (14″ x 0.574″, resolution = 67k) on 2017 December 30 with a SNR of 200/pixel without the iodine cell. Both the C2 and B3 decker allow for sky subtraction which is important for the quality of the radial velocities for a V=10 mag star. We included an additional 142 measurements in our GJ 9827 analysis, for a total of 234 measurements: 7 from FIES (Niraula et al., 2017), 36 from PFS (Teske et al., 2018), 35 from HARPS (Prieto-Arranz et al., 2018), and 64 from HARPS-N (Prieto-Arranz et al., 2018; Rice et al., 2019).

We updated the stellar parameters to incorporate the latest measurements, especially the Gaia DR2 parallaxes (Gaia Collaboration et al., 2016, 2018; Luri et al., 2018). We used multiband stellar photometry (Gaia G and 2MASS JHK), the Gaia parallax, and a stellar effective temperature and metallicity derived from Keck/HIRES spectra via the SpecMatch-Emp tool (Yee et al., 2017). The SpecMatch-Emp values are $T_{\rm eff} = 4195 \pm 70$ K and [Fe/H]$= -0.29 \pm 0.09$. We input these values into the isoclassify tool using the grid-mode option (Huber et al., 2017b) to derive the stellar parameters listed in Table 13.1.

Parameter	Units	Value
[Fe/H]	dex	-0.26±0.08
M_*	$M_\odot$	0.593±0.018
R_*	$R_\odot$	0.579±0.018
log g	dex	4.682±0.021
$T_{\rm eff}$	K	4294±52

Table 13.1: GJ 9827 Stellar Parameters

13.3.2 Stellar Activity Analysis

The K2 light curve for GJ 9827 shows quasi periodic variation with signs of active region evolution between rotation cycles (Figure 13.1). The K2 photometry shown in this paper was produced using k2phot (Petigura et al., 2015, 2017). A Lomb-Scargle periodogram of the K2 data shows two strong peaks around 15 and 30 days consistent with previous works, one peak is likely the rotation period and the other a harmonic. We consider both peaks since stellar rotation periods often do not appear as the highest peak in a periodogram (Nava et al., 2019). The shorter period is favored by Niraula et al. (2017) from the $v \sin i$ measurement, whereas the longer period is favored by Rodriguez et al. (2018); Teske et al. (2018); Prieto-Arranz et al. (2018); Rice et al. (2019) from a combination of periodogram, autocorrelation, and Gaussian process analyses on the light curve as well as from the inferred age of GJ 9827 .

The Keck/HIRES S_{HK} and radial velocity data shown in Figure 13.1, both reveal a tenuous stellar rotation signal at 30 days, consistent with the longer peak in the K2 light curve peridogram. In agreement with previous findings, we conclude that this 30 day signal is likely caused by stellar rotation, as it is present in both the S_{HK} data and the photometry. Since there is power at the same period in our radial velocity

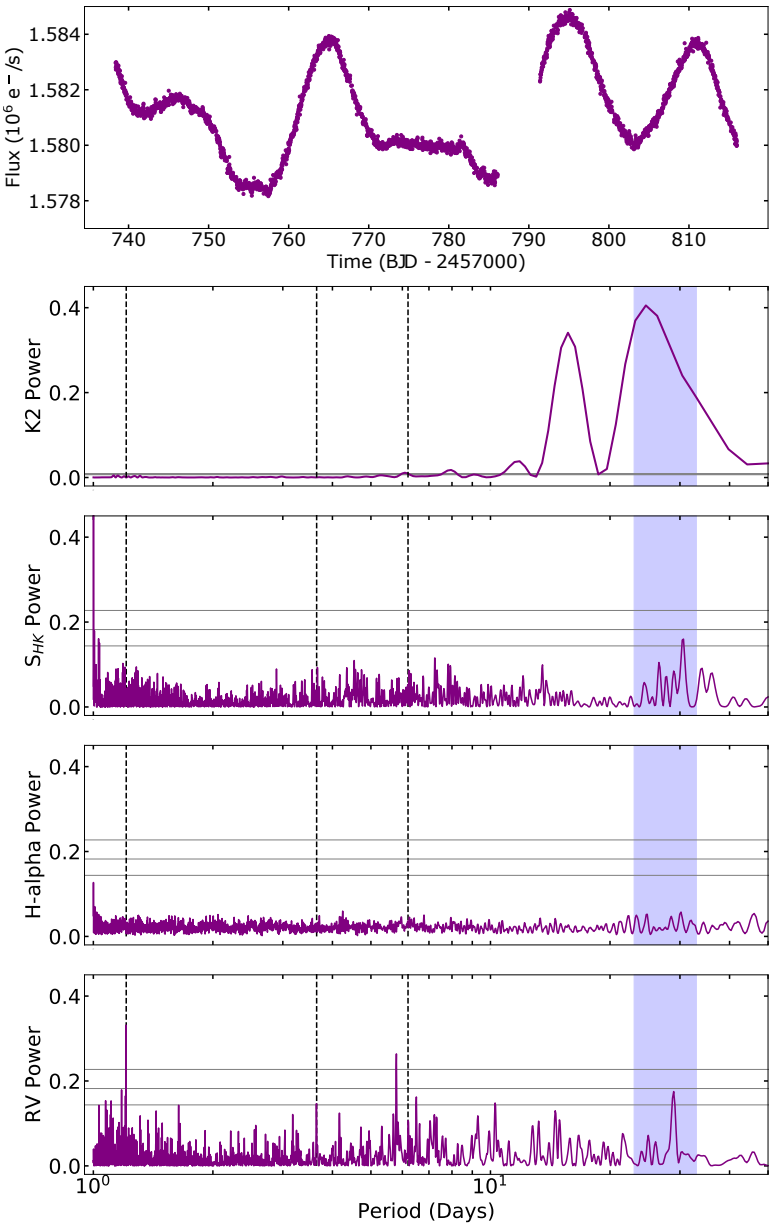

Figure 13.1: Stellar activity analysis for GJ 9827 from K2 photometry and HIRES spectroscopy. There are clear stellar rotation and active region evolution signals visible in the K2 photometry. The Lomb-Scargle periodograms of the K2 photometry, S_{HK}, H-alpha, and radial velocity data include false alarm probabilities of 0.5, 0.1, 0.01 (horizontal lines), stellar rotation (blue shaded area), and planet orbital periods (dashed lines). The S_{HK} and radial velocity data have power consistent with the K2 photometry at 30 days.

data, we need to account for this signal in our radial velocity analysis in order to derive accurate mass measurements for the planets. We chose to mitigate this signal using a Gaussian process.

13.3.3 Radial Velocity Fit

There is evidence of stellar activity in our radial velocity data from the periodogram analysis in section 13.3.2. We include a Gaussian process with a quasi-periodic kernel to model this activity signal in our radial velocity fit as described in chapter 7.

The K2 light curve fit is well constrained by the Gaussian process and produces a stellar rotation period consistent with the periodogram analysis of this data (η_3=$28.62^{+0.48}_{-0.38}$ days). The H-alpha data has very low variation; it is not well fit by this kernel and does not produce meaningful posteriors. The S_{HK} data is well fit by this quasi-periodic kernel and produces a stellar rotation period (η_3) consistent with our periodogram analysis in section 13.3.2. The photometry and the S_{HK} data both produce consistent posteriors; we choose to adopt the posteriors from the S_{HK} fit because these data are taken simultaneously with the radial velocity data and are therefore a direct indicator of the chromospheric magnetic activity. The posteriors on the parameters from our S_{HK} fit are: $\gamma_{S_{HK}} = 0.646^{+0.027}_{-0.026}$, $\sigma_{S_{HK}} = 0.0183^{+0.0035}_{-0.0032}$, $\eta_1 = 0.079^{+0.017}_{-0.012}$, $\eta_2 = 94^{+50}_{-25}$ days, $\eta_3 = 29.86^{+0.78}_{-0.83}$ days, and $\eta_4 = 0.587^{+0.14}_{-0.096}$.

We then performed a Gaussian process fit on the radial velocity data including priors on η_2, η_3, and η_4 equivalent to the S_{HK} fit posteriors. We tested fits including a trend, curvature, and planet eccentricities but reject all of these models due to their

higher AIC values. These tested fits resulted in semi-amplitudes for all three planets consistent to 1σ for planets b and d, and 2σ for planet c with the circular three-planet Gaussian process fit.

We present our GJ 9827 results in Table 13.2. We list the results from a circular three-planet case with and without a Gaussian process for comparison, and adopt the fit including the Gaussian process shown in Figure 13.2. We measure masses for these planets to be M_b=4.87 ± 0.37 $M_\oplus$, M_c=1.92 ± 0.49 $M_\oplus$, and M_d=3.42 ± 0.62 $M_\oplus$.

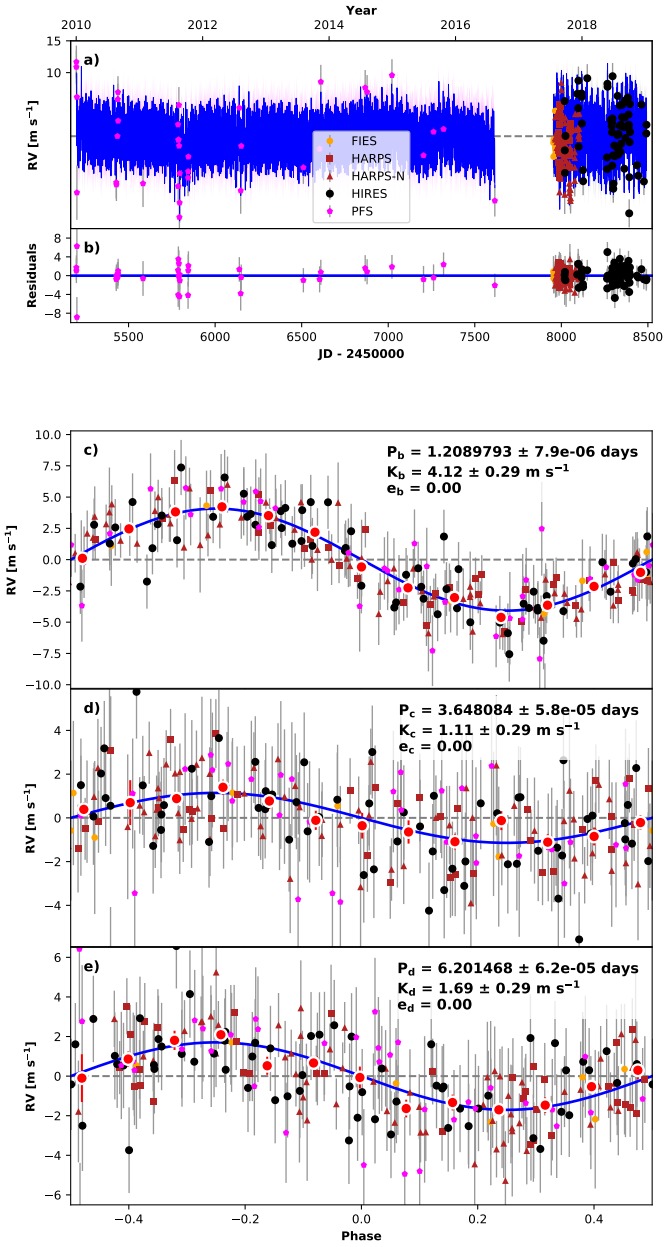

Figure 13.2: Best-fit three-planet Keplerian orbital model for GJ 9827 including a Gaussian process. The thin blue line is the best-fit three-planet model with the mean Gaussian process model; the colored area surrounding this line includes the 1σ maximum-likelihood Gaussian process uncertainties. We add in quadrature the jitter terms listed in Table 13.2 with the measurement uncertainties for the data. **b)** Residuals to the best fit three-planet model. **c), d), e)** RVs phase-folded to the ephemeris of planet b, c, and d, respectively. The Keplerian orbit models for the other planets have been subtracted. Red circles are the same velocities binned in 0.08 units of orbital phase.

Parameter	Name (Units)	Keplerian fit	Gaussian Process fit (adopted)
Orbital Parameters			
P_b	Period (days)	$1.2089765^{+2.2e-06}_{-2.3e-06}$	$1.2089765 \pm 2.3e-06$
$T\mathrm{conj_b}$	Time of Conjunction (BJD-2457700)	38.82586 ± 0.00026	38.82586 ± 0.00026
R_b	Radius ($\mathrm{R}_\oplus$)	$\equiv$1.529$\pm$0.058	$\equiv$1.529$\pm$0.058
e_b	Eccentricity	$\equiv 0.0$	$\equiv 0.0$
ω_b	Argument of Periapse	$\equiv 0.0$	$\equiv 0.0$
K_b	Semi-Amplitude (m s^{-1})	3.5 ± 0.32	4.1 ± 0.3
a_b	Semimajor Axis (AU)	0.01866 ± 0.00019	0.01866 ± 0.00019
M_b	Mass ($\mathrm{M}_\oplus$)	$4.12^{+0.39}_{-0.38}$	4.87 ± 0.37
ρ_b	Density (g cm^{-3})	$6.32^{+1.0}_{-0.87}$	$7.47^{+1.1}_{-0.95}$
P_c	Period (days)	$3.648095^{+2.5e-05}_{-2.4e-05}$	$3.648095 \pm 2.4e-05$
$T\mathrm{conj_c}$	Time of Conjunction (BJD-2457700)	42.19927 ± 0.00071	$42.19929^{+0.00072}_{-0.00071}$
R_c	Radius ($\mathrm{R}_\oplus$)	$\equiv$1.201$\pm$0.046	$\equiv$1.201$\pm$0.046
e_c	Eccentricity	$\equiv 0.0$	$\equiv 0.0$
ω_c	Argument of Periapse	$\equiv 0.0$	$\equiv 0.0$
K_c	Semi-Amplitude (m s^{-1})	1.28 ± 0.32	1.13 ± 0.29
a_c	Semimajor Axis (AU)	$0.03896^{+0.00039}_{-0.0004}$	$0.03896^{+0.00039}_{-0.0004}$
M_c	Mass ($\mathrm{M}_\oplus$)	$2.17^{+0.54}_{-0.55}$	1.92 ± 0.49
ρ_c	Density (g cm^{-3})	$6.9^{+2.0}_{-1.8}$	$6.1^{+1.8}_{-1.6}$
P_d	Period (days)	$6.20183 \pm 1e-05$	$6.20183 \pm 1e-05$
$T\mathrm{conj_d}$	Time of Conjunction (BJD-2457700)	40.96114 ± 0.00044	$40.96114^{+0.00045}_{-0.00044}$
R_d	Radius ($\mathrm{R}_\oplus$)	$\equiv$1.955$\pm$0.075	$\equiv$1.955$\pm$0.075
e_d	Eccentricity	$\equiv 0.0$	$\equiv 0.0$
ω_d	Argument of Periapse	$\equiv 0.0$	$\equiv 0.0$
K_d	Semi-Amplitude (m s^{-1})	1.63 ± 0.31	1.7 ± 0.3
a_d	Semimajor Axis (AU)	$0.0555^{+0.00056}_{-0.00057}$	$0.0555^{+0.00055}_{-0.00057}$
M_d	Mass ($\mathrm{M}_\oplus$)	3.29 ± 0.64	3.42 ± 0.62
ρ_d	Density (g cm^{-3})	$2.41^{+0.58}_{-0.52}$	$2.51^{+0.57}_{-0.51}$

Derived parameters use M_*=0.593 $\pm$ 0.018, R_*=0.579 $\pm$ 0.019 (Kosiarek et al., 2021), $\mathrm{R}_b/\mathrm{R}_*$=0.02420 $\pm$ 0.00044, $\mathrm{R}_c/\mathrm{R}_*$=0.01899 $\pm$ 0.00036, $\mathrm{R}_d/\mathrm{R}_*$=0.03093 $\pm$ 0.00062 (Rodriguez et al., 2018).

Table 13.2: GJ 9827 Radial Velocity Fit Parameters Part 1

Parameter	Name (Units)	Keplerian fit	Gaussian Process fit (adopted)
Instrument Parameters			
$\gamma_{\rm HIRES}$	Mean center-of-mass (m s^{-1})	$-1.87^{+0.38}_{-0.39}$	$-2.4^{+1.3}_{-1.4}$
$\gamma_{\rm HARPS}$	Mean center-of-mass (m s^{-1})	31946.64 ± 0.37	$31947.7^{+4.0}_{-3.6}$
$\gamma_{\rm HARPS-N}$	Mean center-of-mass (m s^{-1})	$31948.64^{+0.43}_{-0.42}$	$31950.2^{+2.7}_{-2.6}$
$\gamma_{\rm PFS}$	Mean center-of-mass (m s^{-1})	0.28 ± 0.86	0.6 ± 1.2
$\gamma_{\rm FIES}$	Mean center-of-mass (m s^{-1})	$31775.5^{+1.1}_{-1.2}$	31775.6 ± 1.5
$\sigma_{\rm HIRES}$	Jitter (m s^{-1})	$3.45^{+0.32}_{-0.27}$	$2.15^{+0.49}_{-0.43}$
$\sigma_{\rm HARPS}$	Jitter (m s^{-1})	$1.65^{+0.39}_{-0.35}$	$0.91^{+0.44}_{-0.45}$
$\sigma_{\rm HARPS-N}$	Jitter (m s^{-1})	$2.79^{+0.39}_{-0.35}$	$0.74^{+0.44}_{-0.45}$
$\sigma_{\rm PFS}$	Jitter (m s^{-1})	$4.68^{+0.75}_{-0.62}$	4.0 ± 1.1
$\sigma_{\rm FIES}$	Jitter (m s^{-1})	$0.0001^{+0.0016}_{-0.0001}$	$0.035^{+2.6}_{-0.035}$
Gaussian Process Parameters			
$\eta_{1,\rm HIRES}$	Amplitude (m s^{-1})	N/A	$3.7^{+1.2}_{-1.0}$
$\eta_{1,\rm HARPS}$	Amplitude (m s^{-1})	N/A	$5.3^{+3.5}_{-2.2}$
$\eta_{1,\rm HARPS-N}$	Amplitude (m s^{-1})	N/A	$5.1^{+2.3}_{-1.5}$
$\eta_{1,\rm PFS}$	Amplitude (m s^{-1})	N/A	4.0 ± 1.1
$\eta_{1,\rm FIES}$	Amplitude (m s^{-1})	N/A	$0.035^{+2.6}_{-0.035}$
η_2	Evolutionary Timescale (days)	N/A	82^{+17}_{-14}
η_3	Signal Period (days)	N/A	$28.62^{+0.48}_{-0.38}$
η_4	Lengthscale	N/A	$0.418^{+0.082}_{-0.065}$

Table 13.3: GJ 9827 Radial Velocity Fit Parameters Part 2

13.4 Composition Discussion

To further investigate the interior compositions of these planets, we compared their masses and radii with model composition grids from Zeng and Sasselov (2013); Lopez and Fortney (2014); Zeng et al. (2016). We focus on two main compositions: Earth-like rock & iron cores surrounded by H/He envelopes and mixtures of water, rock, and iron. Our results are tabulated in Table 13.4.

Planet	f_{HHe} (%)	f_{H_2O} (%)
GJ 9827 b	$0.02^{+0.01}_{-0.01}$	$2.20^{+3.84}_{-1.69}$
GJ 9827 c	$0.01^{+0.01}_{-0.00}$	$13.57^{+25.18}_{-10.40}$
GJ 9827 d	$0.54^{+0.20}_{-0.17}$	$79.10^{+14.35}_{-20.14}$

Table 13.4: GJ 9827 Planets' Potential Hydrogen/Helium and Water Mass Fraction Surrounding an Earth-like Core

To calculate potential H/He mass fractions, we use the grids of thermal evolution models provided by Lopez & Fortney (2014) which calculate the radius of a planet given varying incident fluxes relative to Earth ($S_{inc}/S_{\oplus}$), masses ($M_p/M_{\oplus}$), ages, and fractions f_{HHe} of their masses contained in H/He envelopes surrounding Earth-like rock and iron cores. We use the `smint` (Structure Model INTerpolator) interpolation and envelope mass fraction fitting package[1] to solve the inverse problem of inferring a planet's envelope mass fraction from its incident flux, mass, age, and radius.

`smint` performs linear interpolation over a grid of f_{HHe}, $\log_{10} M_p/M_{\oplus}$, system age and $\log_{10} S_{inc}/S_{\oplus}$ and returns the corresponding planet radius. We then run a MCMC that fits for the combination of S_{inc}, M_p, age, and f_{HHe} that best matches

[1] `https://github.com/cpiaulet/smint`

the observed planet radius. We adopt Gaussian priors on S_{inc} and M_p informed by the stellar and planetary parameters. We use a uniform prior on the planet's envelope mass fraction over the range spanned by the Lopez and Fortney (2014) grids (from 0.1% to 20%) and adopt a uniform prior on the system age from 1 to 10 Gyr. Each of the 100 chains is run for at least 10,000 steps, 60% of which are discarded as burn-in. We make sure that, in each case, the chains have run for at least 50 times the maximum autocorrelation time recorded across all parameters and thus secure that our chains are converged and well sample the posterior PDFs. We display a corner plot for GJ 9827 d, the only planet consistent with a moderate H/He envelope (Figure 13.3). GJ 9827 d is consistent with a 1% H/He envelope by mass.

To fit for the water mass fractions (f_{H_2O}), we use the implementation of the Zeng et al. (2016) two-component (water+rock) model grid in `smint` (Table 13.4). The MCMC process is analog to that used to fit for f_{HHe}, adopting a uniform prior on the water mass fraction (0–100 %) and a Gaussian prior on the planet mass. We match the observed planet radius via a Gaussian likelihood.

To further investigate the potential f_{H_2O}, we explore three component models of H_2O, $MgSiO_3$, and Fe. We use a numerical tool[2] in order to solve for the interior structure of each planet and produce ternary diagrams of the range of combinations of $MgSiO_3$, Fe, and H_2O mass fractions that are compatible with the observed mass and radius (Zeng and Sasselov, 2013; Zeng et al., 2016). These ternary diagrams are shown in Figure 13.4. GJ 9827 b and GJ 9827 c both have a low H_2O fraction ($\leq$40%) and a

[2] `https://www.cfa.harvard.edu/~lzeng`

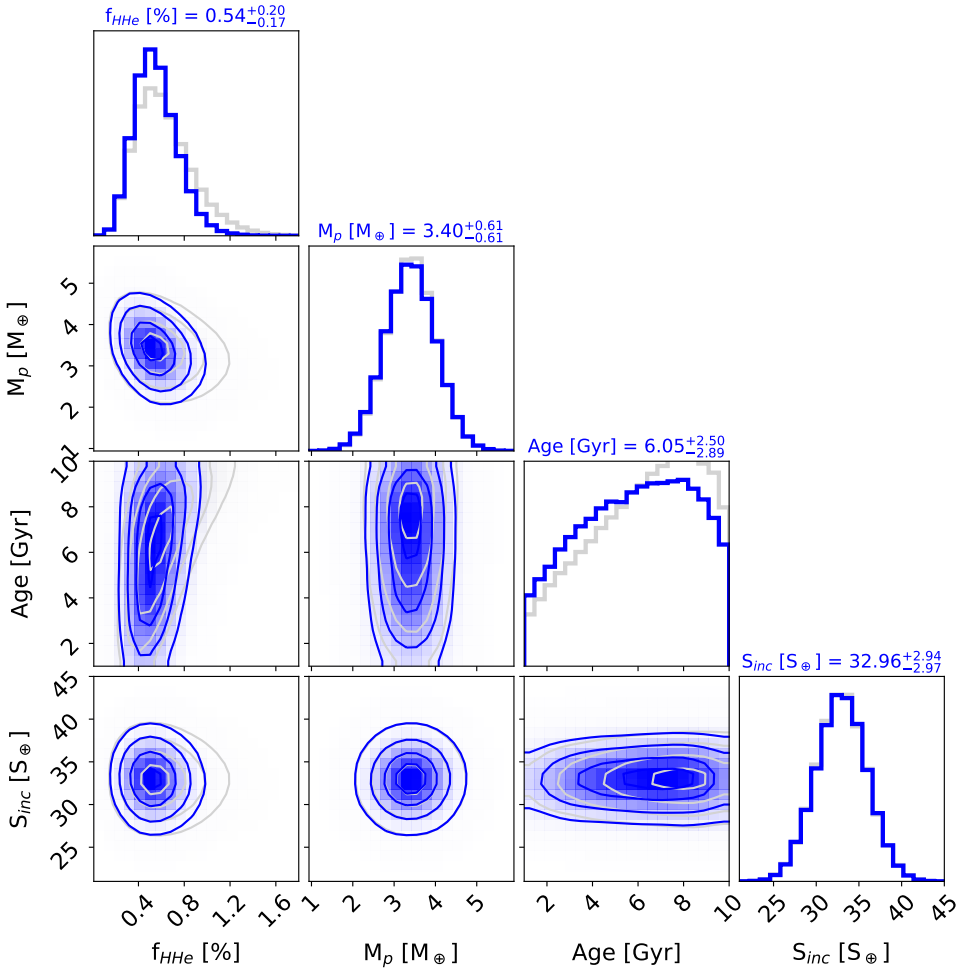

(a) GJ 9827 d

Figure 13.3: H_2/He Composition Models for GJ 9827. Joint and marginalized posterior distributions on the fitted parameters for a 1× (50×) solar metallicity H_2/He envelope atop an Earth-like core are shown in blue (gray). The median and $\pm 1\sigma$ constraints on the parameters for the 1× solar metallicity case are quoted above each marginalized distribution.

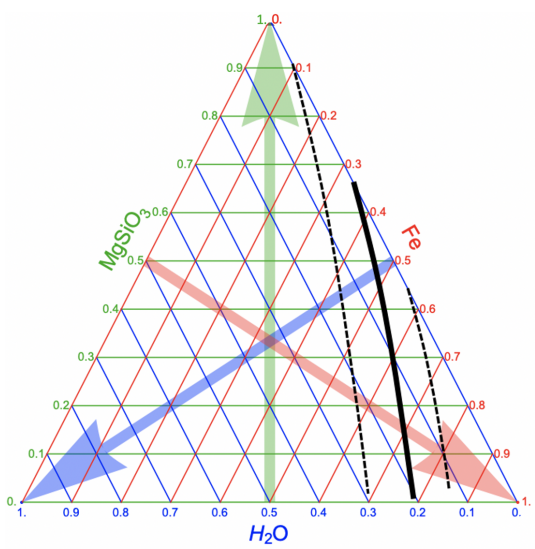

(a) GJ 9827 b

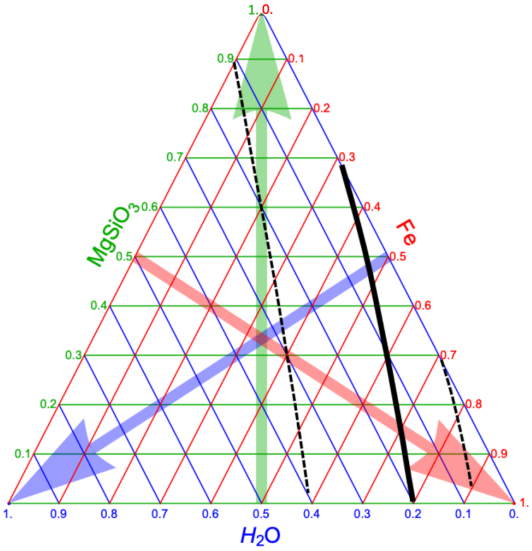

(b) GJ 9827 c

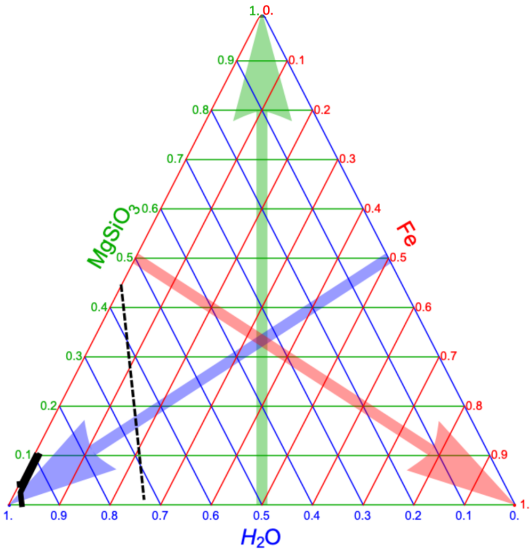

(c) GJ 9827 d

Figure 13.4: Ternary diagrams for GJ 9827 using a 3-component H_2O/$MgSiO_3$/Fe model (Zeng and Sasselov, 2013; Zeng et al., 2016). The solid line outlines the median mass and radius of each planet, while the dashed line(s) delineate the 1σ contours. At any point in the diagram the mass fractions can be found by following the three thin colored lines towards their respective side.

wide range of possibilities for $MgSiO_3$ & Fe. GJ 9827 d is consistent with a high H_2O fraction (50–100%) and small fractions of $MgSiO_3$ (0–50%) and Fe (0–30%).

Both Prieto-Arranz et al. (2018) and Rice et al. (2019) suggest that photoevaporation may have sculpted the inner two rocky GJ 9827 planets. However, the outer planet, GJ 9827 d, must have retained a moderate fraction of volatiles to be consistent with its mass and radius. We examine whether the system as a whole is consistent with the theory of photoevaporation through calculating the minimum mass required of planet d to retain its atmosphere assuming planets b and c lost theirs to photoevaporation, as described in Owen and Campos Estrada (2019). We find the minimum mass for GJ 9827 d is 1 $M_\oplus$, lower than its mass of 3.3 $M_\oplus$. Therefore, this system is in agreement with this photevaporation model (Owen and Wu, 2013, 2017). Although, GJ 9827 d may have had a different type of atmospheric evolution other than photoevaporation. Kasper et al. (2020) set stringent limits on the presence of any extended atmosphere around GJ 9827 d via high-resolution spectroscopy of the metastable 10,833 Å He triplet, inconsistent with current models of atmospheric formation and mass loss.

13.5 Conclusion

This bright host star hosts three super-Earth and sub-Neptune planets well suited for atmospheric characterization, two with pending HST transmission spectra analyses (Hedges et al. in prep, Benneke et al in prep). As the results of a multi-year high-cadence observing campaign with Keck/HIRES, we improved the planets' mass

measurements in preparation for the interpretation of these HST transmission spectra.

We measured planet masses in the GJ 9827 system to be M_b=4.87 $\pm$ 0.37 $M_\oplus$, M_c=1.92 $\pm$ 0.49 $M_\oplus$, and M_d=3.42 $\pm$ 0.62 $M_\oplus$. We have achieved 5σ masses for the two planets with pending HST analyses. Stellar activity signatures in the photometry and Calcium II H&K lines informed our use of a Gaussian process to account for this activity in our radial velocity fit.

Through our interior composition analysis, we found GJ 9827 b and GJ 9827 c are both consistent with a 50/50 rock-iron composition and GJ 9827 d requires additional volatiles to be consistent with its bulk density.

Chapter 14

HD 106315

14.1 Abstract

HD 106315 is a bright, nearby star that hosts two small planets discovered by K2 that are well suited for atmospheric characterization. Through a multi-year high-cadence observing campaign with Keck/HIRES and Magellan/PFS, we improved the planets' mass measurements in anticipation of HST transmission spectroscopy. We measured planet masses of M_b=10.5 $\pm$ 3.1 $M_\oplus$ and M_c=12.0 $\pm$ 3.8 $M_\oplus$. We found that a Gaussian process activity-radial velocity decorrelation was not effective due to the reduced presence of spots and speculate that this may extend to other hot stars as well ($T_{\rm eff}$ > 6200 K). We investigated the planets' compositions through comparing their masses and radii to a range of interior models. HD 106315 b is consistent with a rocky core with moderate amounts of water or hydrogen/helium and HD 106315 c is consistent with a ∼10% hydrogen/helium envelope surrounding an Earth-like rock and iron core.

14.2 Introduction

HD 106315 (K2-109) is a bright (V=8.97 mag, K=7.85 mag) F5 dwarf star hosting two planets discovered in K2 Campaign 10 (Crossfield et al., 2017; Rodriguez et al., 2017). Planet b is a small (R_b=2.40 $\pm$ 0.20 $R_\oplus$) planet with an orbital period of 9.55 days; planet c is a warm Neptune-sized (R_c=4.379 $\pm$ 0.086 $R_\oplus$) planet with an orbital period of 21.06 days.

This system was further characterized with HARPS radial velocity observations by Barros et al. (2017) to determine the planets' masses (M_b=12.6 $\pm$ 3.2 $M_\oplus$ and M_c=15.2 $\pm$ 3.7 $M_\oplus$). They concluded that HD 106315 b likely has a rocky core and decent water mass fraction whereas HD 106315 c has a substantial hydrogen-helium envelope. Additional transits of HD 106315 c were observed with two ground based facilities: the Euler telescope (Lendl et al., 2017) and the Cerro Tololo Inter-American Observatory (CTIO, Barros et al., 2017). These measurements improved the precision on both the orbital period and the time of transit.

Later Zhou et al. (2018) investigated the system architecture through measuring the obliquity of HD 106315 c using Doppler tomography and constraining the mutual inclination of HD 106315 b through dynamical arguments. They found that these two planets both have low obliquities, consistent with the few other warm Neptunes with measured obliquities (e.g. Albrecht et al., 2013).

14.3 Radial Velocity Analysis

14.3.1 Data Collection

We obtained 352 measurements of HD 106315 with HIRES between 2016 December 23 and 2020 Febuary 1; 53 of these observations were previously published in Crossfield et al. (2017). These data were collected with the B5 decker (3.5″ x 0.861″, resolution = 50k) with a typical SNR of 200/pixel (250k on the exposure meter, median exposure time of 4.8 minutes). Data were typically taken in groups of three consecutive observations to mitigate p-mode oscillations; Barros et al. (2017) estimated p-mode periods of ∼20 minutes whereas Chaplin et al. (2019) estimates timescales to be ∼30 minutes. When possible, multiple visits separated by an hour were taken to improve precision due to the high $v \sin i$; these data were then binned in nightly bins to average over short-timescale activity. We also collected a higher resolution template observation with the B3 decker on 2016 December 24. The template was a triple exposure with a total SNR of 346/pixel (250k each on the exposure meter) without the iodine cell.

We obtained 25 measurements of HD 106315 with PFS between 2017 January 6 and 2018 June 30. Data taken prior to 2018 February were taken with the 0.5″ slit (resolution∼80k); a single observation with an exposure time of 10 to 25 minutes was taken per night. After a PFS upgrade in 2018 February, multiple exposures were taken with the 0.3″ slit (resolution∼130k). As with the HIRES data, we binned these consecutive observations for our analysis. An iodine-free template, consisting of three 1000s exposures, was taken with the 0.3″ slit on 2018 June 27. The PFS data were

Parameter	Units	Value
[Fe/H]	dex	-0.22±0.09
M_*	$M_\odot$	1.154±0.042
R_*	$R_\odot$	1.269±0.024
log g	dex	4.291±0.025
$T_{\rm eff}$	K	6364±87

Table 14.1: HD 106315 Stellar Parameters

reduced using a custom IDL pipeline and velocities extracted based on the methodology described in Butler et al. (1996).

We additionally include 84 measurements from HARPS (Barros et al., 2017), for a total of 461 measurements (160 binned points) in our HD 106315 analysis. We collected 125 measurements on the APF but do not include them in the analysis due to the high scatter (30 m/s nightly RMS, 7.3 m/s RV uncertainty).

We updated the stellar parameters for HD 106315 to incorporate the latest measurements, especially the Gaia DR2 parallaxes (Gaia Collaboration et al., 2016, 2018; Luri et al., 2018). We used multiband stellar photometry (Gaia G and 2MASS JHK), the Gaia parallax, and a stellar effective temperature and metallicity derived from Keck/HIRES spectra via the SpecMatch-Emp tool (Yee et al., 2017). The SpecMatch-Emp values are $T_{\rm eff} = 6318 \pm 110$ K and [Fe/H]$= -0.21 \pm 0.09$. We input the above values into the isoclassify tool using the grid-mode option (Huber et al., 2017b) to derive the stellar parameters listed in Table 14.1.

14.3.2 Stellar Activity Analysis

We aim to understand the stellar activity component of the radial velocity data through investigating the possible relationships between the K2 light curve, the Calcium II H&K and H-alpha stellar lines, and our radial velocity data. The projected rotational velocity measurement ($v \sin i = 13.2 \pm 1$ km s^{-1}) combined with the obliquity measurement ($\lambda = -10.9 \pm 3.7$, Zhou et al., 2018) suggests a stellar rotation period of 4.78±0.15 days.

HD 106315 was observed in K2 Campaign 10; this campaign had a 14 day data gap resulting in 49 days of contiguous data. With a 4.8 day rotation period, the shorter campaign should not impact our conclusions about stellar activity from this photometry. The K2 light curve (Figure 14.1) has low photometric variability; the periodogram shows a small peak near the stellar rotation period at 4.8 days and a larger peak at the second harmonic of the rotation period at 9.6 days.

We next investigated the potential radial velocity signal from the stellar rotation by examining the S_{HK} and H-alpha data in the HIRES spectra. We find no significant peaks near 4.8 days or elsewhere in Lomb-Scargle periodograms of the HIRES activity indicators and radial velocity data (Figure 14.1). The absence of these signals suggests that the stellar rotation is not contributing a significant stellar activity signal to the radial velocity measurements, potentially attributed to the low spot coverage of this F star ($< 1\%$, Kreidberg et al., 2020).

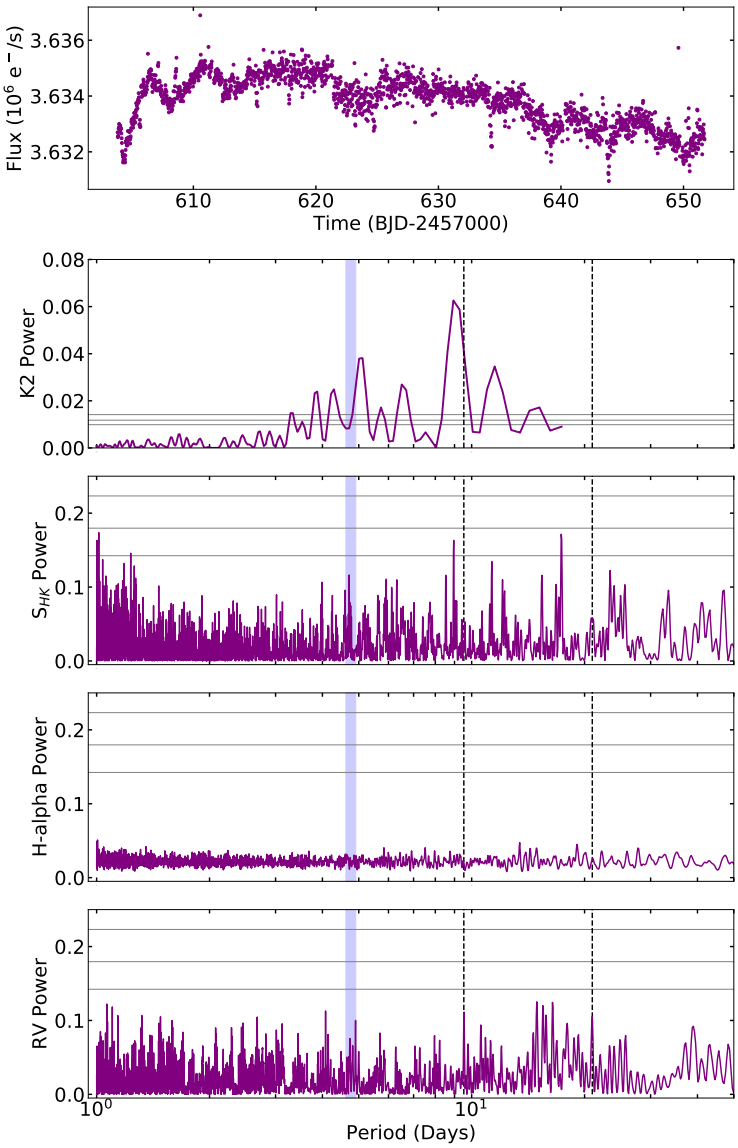

Figure 14.1: Activity analysis for HD 106315 from K2 photometry and HIRES spectroscopy. The Lomb-Scargle periodograms of the photometry, S_{HK}, H-alpha, and radial velocity data include false alarm probabilities of 0.5, 0.1, 0.01 (horizontal lines), stellar rotation period (thick blue line), and planet orbital periods (dashed lines). There are peaks near the rotation period and second harmonic in the K2 photometry, we find no similar peaks in the HIRES activity indicators or radial velocity data.

14.3.3 Radial Velocity Fit

We fit the radial velocity data using `radvel` as described in chapter 6. The circular two-planet fit is favored by the AIC over fits with a trend, curvature, or planet eccentricities; results are listed in Table 14.2 and the fit is displayed in Figure 14.2. In agreement with Barros et al. (2017), we do not see evidence of the trend suggested in Crossfield et al. (2017) with an AIC value 1.25 larger than the circular case. We determine masses for the HD 106315 system to be M_b=10.5 $\pm$ 3.1 $M_\oplus$ and M_c=12.0 $\pm$ 3.8 $M_\oplus$.

We choose not to include a Gaussian process in our HD 106315 fit as we do not see evidence for stellar rotation induced activity contamination in the activity indicators or radial velocity data. We suspect the low spot coverage of HD 106315 ($< 1\%$, Kreidberg et al., 2020) is why we see a small rotation signal in the photometry and a lack of this signal in our radial velocity data.

Barros et al. (2017) do use a Gaussian process for their analysis of HD 106315. The derived Gaussian process period is 2.8 days and their full width half maximum (FWHM) measurements also show a similar periodicity leading them to believe that this signal arises from stellar activity. At the time, Zhou et al. (2018) had not yet measured the obliquity; therefore, Barros et al. (2017) hypothesized that this 2.8 day signal was the stellar rotation period or half of the rotation period.

If this signal is associated with stellar activity, it is possible that their high cadence radial velocity run is more sensitive to this activity than our data collection

Parameter	Name (Units)	Keplerian (adopted)	Gaussian Process
Orbital Parameters			
P_b	Period (days)	9.55288 ± 0.00021	$9.55288^{+0.00019}_{-0.00021}$
$T\mathrm{conj_b}$	Time of Conjunction (BJD-2457000)	$586.5476^{+0.0024}_{-0.0025}$	$586.5479^{+0.003}_{-0.0026}$
R_b	Radius ($R_\oplus$)	$\equiv 2.40 \pm 0.20$	$\equiv 2.40 \pm 0.20$
e_b	Eccentricity	$\equiv 0.0$	$\equiv 0.0$
ω_b	Argument of Periapse	$\equiv 0.0$	$\equiv 0.0$
K_b	Semi-Amplitude (m s^{-1})	$2.88^{+0.85}_{-0.84}$	$2.91^{+0.79}_{-0.85}$
a_b	Semimajor Axis (AU)	$0.0924^{+0.0011}_{-0.0012}$	$0.0924^{+0.0011}_{-0.0012}$
M_b	Mass ($M_\oplus$)	10.5 ± 3.1	$10.6^{+2.9}_{-3.1}$
ρ_b	Density (g cm^{-3})	$4.1^{+1.9}_{-1.4}$	$4.1^{+1.8}_{-1.4}$
P_c	Period (days)	21.05652 ± 0.00012	21.05653 ± 0.00012
$T\mathrm{conj_c}$	Time of Conjunction (BJD-2457000)	$569.01767^{+0.00097}_{-0.00096}$	$569.0178^{+0.0012}_{-0.001}$
R_c	Radius ($R_\oplus$)	$\equiv 4.379 \pm 0.086$	$\equiv 4.379 \pm 0.086$
e_c	Eccentricity	$\equiv 0.0$	$\equiv 0.0$
ω_c	Argument of Periapse	$\equiv 0.0$	$\equiv 0.0$
K_c	Semi-Amplitude (m s^{-1})	2.53 ± 0.79	$2.61^{+0.74}_{-0.87}$
a_c	Semimajor Axis (AU)	$0.1565^{+0.0019}_{-0.002}$	$0.1565^{+0.0019}_{-0.002}$
M_c	Mass ($M_\oplus$)	12.0 ± 3.8	$12.4^{+3.5}_{-4.2}$
ρ_c	Density (g cm^{-3})	$0.78^{+0.26}_{-0.25}$	$0.81^{+0.24}_{-0.27}$
Instrument Parameters			
γ_{HIRES}	Center-of-mass (m s^{-1})	$-2.48^{+0.96}_{-0.97}$	$-2.7^{+1.0}_{-1.1}$
γ_{HARPS}	Center-of-mass (m s^{-1})	$-3462.94^{+0.7}_{-0.71}$	$-3462.77^{+1.1}_{-0.87}$
γ_{PFS}	Center-of-mass (m s^{-1})	$-2.9^{+2.8}_{-2.7}$	$-2.5^{+3.2}_{-3.3}$
σ_{HIRES}	Jitter (m s^{-1})	$8.33^{+0.85}_{-0.79}$	$6.4^{+1.2}_{-1.1}$
σ_{HARPS}	Jitter (m s^{-1})	$2.94^{+0.94}_{-1.0}$	$2.3^{+1.0}_{-1.4}$
σ_{PFS}	Jitter (m s^{-1})	$9.4^{+2.6}_{-2.3}$	$4.0^{+4.6}_{-2.7}$
Gaussian Process Parameters			
$\eta_{1,\mathrm{HIRES}}$	Amplitude (m s^{-1})	N/A	$5.2^{+1.1}_{-1.7}$
$\eta_{1,\mathrm{HARPS}}$	Amplitude (m s^{-1})	N/A	$2.3^{+1.0}_{-1.4}$
$\eta_{1,\mathrm{PFS}}$	Amplitude (m s^{-1})	N/A	$4.0^{+4.6}_{-2.7}$
η_2	Evolutionary Timescale (days)	N/A	$5.27^{+0.54}_{-0.65}$
η_3	Signal Period (days)	N/A	$4.5^{+0.49}_{-0.65}$
η_4	Lengthscale	N/A	$0.56^{+0.036}_{-0.04}$

Derived parameters use M_*=1.154 ± 0.043, R_*=1.269 ± 0.024 (Kosiarek et al., 2021), R_b/R_*=0.01708 ± 0.00135 (Crossfield et al., 2017), R_c/R_*=0.031636 ± 0.0001834 (Kreidberg et al., 2020).

Table 14.2: HD 106315 Radial Velocity Fit Parameters

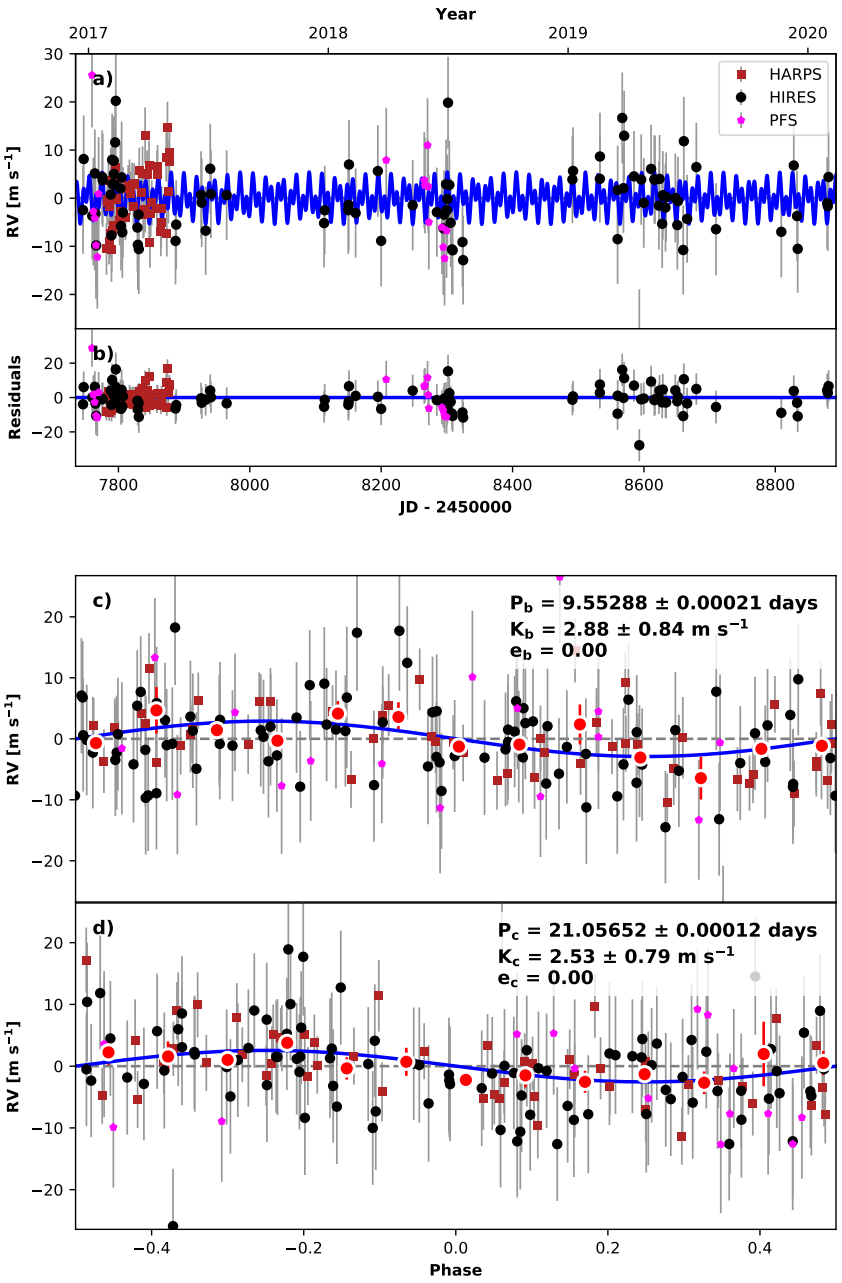

Figure 14.2: Best-fit two-planet Keplerian orbital model for HD 106315. The thin blue line is the best fit two-planet model. We add in quadrature the jitter terms listed in Table 14.2 with the measurement uncertainties for the data. **b)** Residuals to the best fit two-planet model. **c), d)** Radial velocities phase-folded to the ephemeris of planet b and c respectively. Red circles are the same velocities binned in 0.08 units of orbital phase.

spanning multiple years. The HARPS measurements were collected on 47 nights over three months, whereas we have 94 nights of HIRES measurements over three years. It is also possible that the Gaussian process used by Barros et al. (2017) had fit spurious noise instead of a stellar activity signal; the 2.8 day signal is inconsistent with the rotation period and half of the rotation period. Hotter stars (T_{eff} >6200 K) often have shallow convective envelopes and inefficient magnetic dynamos which result in fewer spots on the stellar surface (Kraft, 1967). Therefore, hotter stars like HD 106315 may not have enough starspots for this type of Gaussian process to be effective.

For completeness, we perform a Gaussian process fit on the HD 106315 radial velocity data. We first fit the K2 data using a Gaussian process as this dataset showed periodicity at the stellar rotation period; the posteriors of this fit are: $\gamma_{K2} = 3633710^{+190}_{-200}$ $e^{-}s^{-1}$, $\sigma_{K2} = 117^{+16}_{-15}$ $e^{-}s^{-1}$, $\eta_1 = 655^{+84}_{-68}$ $e^{-}s^{-1}$, $\eta_2 = 5.17^{+0.66}_{-0.64}$ days, $\eta_3 = 4.49^{+0.61}_{-0.26}$ days, $\eta_4 = 0.55^{+0.04}_{-0.044}$. We then performed a Gaussian process fit on the radial velocity data including priors on η_2, η_3, and η_4 from the K2 fit posteriors. This fit results in semi-amplitudes consistent to 1σ for both planets: the full results are shown in Table 14.2. The Gaussian process fit has a higher AIC value (ΔAIC=7.38) suggesting that Gaussian process parameters do not significantly improve the fit. For this reason, and as we do not see signs of stellar activity in our activity indicators or radial velocity data, we adopt the fit without a Gaussian process.

14.4 Composition Discussion

To further investigate the interior compositions of these planets, we compared their masses and radii with model composition grids from Zeng and Sasselov (2013); Lopez and Fortney (2014); Zeng et al. (2016). We focus on two main compositions: Earth-like rock & iron cores surrounded by H/He envelopes and mixtures of water, rock, and iron. Our results are tabulated in Table 14.3.

Planet	f_{HHe} (%)	f_{H_2O} (%)
HD 106315 b	$0.96^{+0.72}_{-0.51}$	$54.29^{+29.06}_{-30.09}$
HD 106315 c	$12.74^{+1.11}_{-1.06}$	$99.27^{+0.57}_{-1.25}$

Table 14.3: HD 106315 Planets' Potential Hydrogen/Helium and Water Mass Fraction Surrounding an Earth-like Core

To calculate potential H/He mass fractions, we use the grids of thermal evolution models provided by Lopez & Fortney (2014) which calculate the radius of a planet given varying incident fluxes relative to Earth ($S_{inc}/S_{\oplus}$), masses ($M_p/M_{\oplus}$), ages, and fractions f_{HHe} of their masses contained in H/He envelopes surrounding Earth-like rock and iron cores. We use the `smint` (Structure Model INTerpolator) interpolation and envelope mass fraction fitting package[1], in order to solve the inverse problem of inferring a planet's envelope mass fraction from its incident flux, mass, age, and radius.

`smint` performs linear interpolation over a grid of f_{HHe}, $\log_{10} M_p/M_{\oplus}$, system age and $\log_{10} S_{inc}/S_{\oplus}$ and returns the corresponding planet radius. We then run a MCMC that fits for the combination of S_{inc}, M_p, age, and f_{HHe} that best matches the

[1] `https://github.com/cpiaulet/smint`

observed planet radius. We adopt Gaussian priors on S_{inc} and M_p informed by the stellar and planetary parameters. We use a uniform prior on the planet's envelope mass fraction over the range spanned by the Lopez and Fortney (2014) grids (from 0.1 to 20%) and adopt a uniform prior on the system age from 1 to 10 Gyr. Each of the 100 chains is run for at least 10,000 steps, 60% of which are discarded as burn-in. We make sure that, in each case, the chains have run for at least 50 times the maximum autocorrelation time recorded across all parameters and thus secure that our chains are converged and well sample the posterior PDFs. HD 106315 b is consistent with a 1% H/He envelope and HD 106315 c is consistent with a 13% H/He envelope (Figure 14.3).

To fit for the water mass fractions (f_{H_2O}), we use the implementation of the Zeng et al. (2016) two-component (water+rock) model grid in `smint`. The MCMC process is analog to that used to fit for f_{HHe}, adopting a uniform prior on the water mass fraction (0–100 %) and a Gaussian prior on the planet mass. We match the observed planet radius via a Gaussian likelihood. To further investigate the potential f_{H_2O} for HD 106315 b, we explore three component models of H_2O, $MgSiO_3$, and Fe; we exclude HD 106315 c as its low density is inconsistent with these models. We use a numerical tool[2] in order to solve for the interior structure of each planet and produce ternary diagrams (Figure 14.4) of the range of combinations of $MgSiO_3$, Fe, and H_2O mass fractions that are compatible with the observed mass and radius (Zeng and Sasselov, 2013; Zeng et al., 2016). HD 106315 b is consistent with a wide range for all three components (10–100% H_2O, 0–90% $MgSiO_3$, and 0–60% Fe).

[2] `https://www.cfa.harvard.edu/~lzeng`

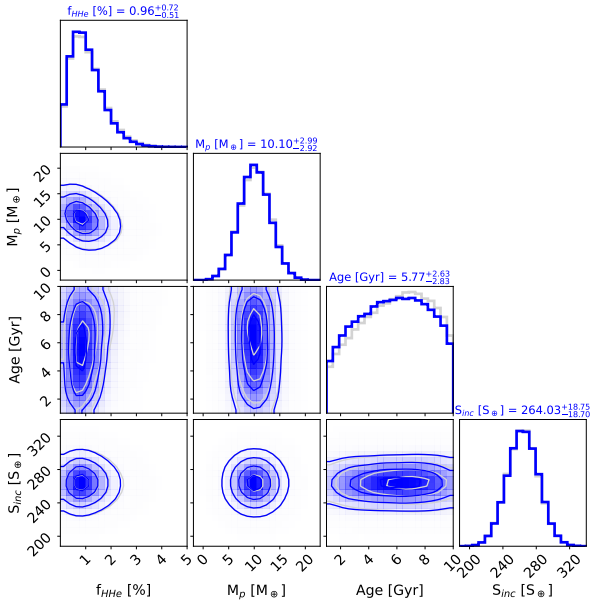

(a) HD 106315 b

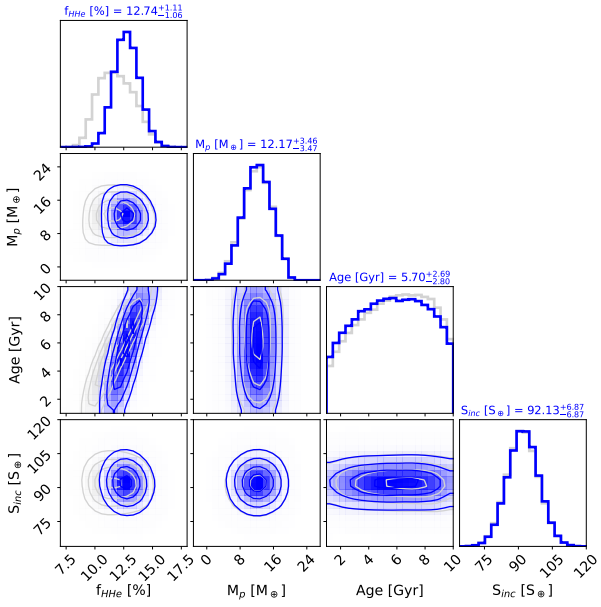

(b) HD 106315 c

Figure 14.3: H_2/He Composition Models for HD 106315. Joint and marginalized posterior distributions on the fitted parameters for a 1× (50×) solar metallicity H_2/He envelope atop an Earth-like core are shown in blue (gray). The median and $\pm 1\sigma$ constraints on the parameters for the 1× solar metallicity case are quoted above each marginalized distribution.

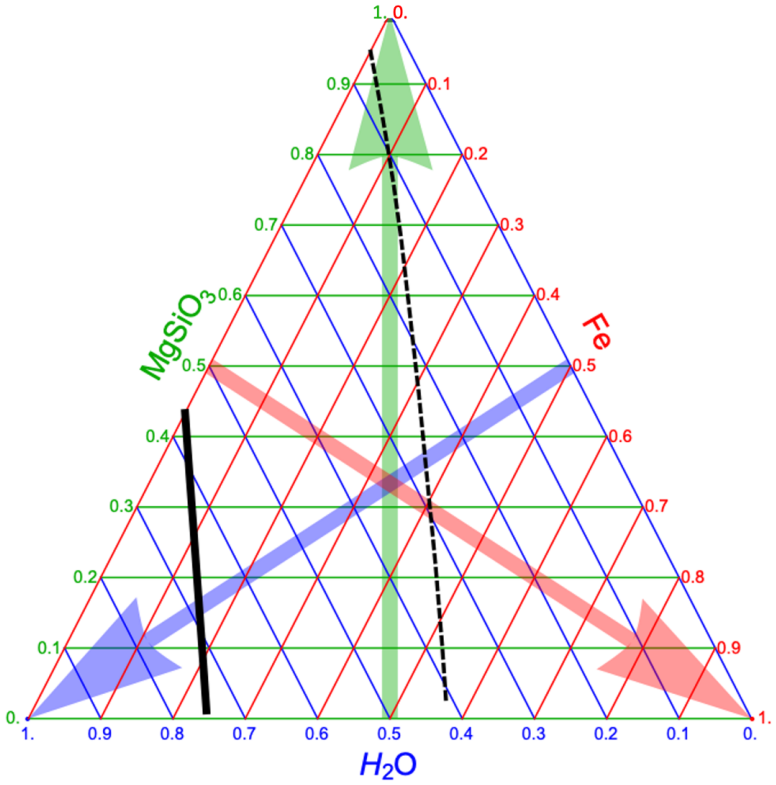

(a) HD 106315 b

Figure 14.4: Ternary diagram for HD 106315 b using a 3-component H_2O/$MgSiO_3$/Fe model (Zeng and Sasselov, 2013; Zeng et al., 2016). The solid line outlines the median mass and radius of each planet, while the dashed line(s) delineate the 1σ contours. At any point in the diagram the mass fractions can be found by following the three thin colored lines towards their respective side.

14.5 Conclusion

This bright host star hosts two small planets well suited for atmospheric characterization, one with an observed HST transmission spectrum (Kreidberg et al., 2020). As the results of a multi-year high-cadence observing campaign with Keck/HIRES and Magellan/PFS, we improved the planets' mass measurements in preparation for the interpretation of this HST transmission spectrum.

We found planet masses of M_b=10.5 $\pm$ 3.1 $M_\oplus$ and M_c=12.0 $\pm$ 3.8 $M_\oplus$. We achieved a 4σ mass for HD 106315 c, critical for the characterization of its HST transmission spectrum. We did not include a Gaussian process in our adopted HD 106315 fit due to the higher AIC value and the lack of activity signatures seen in the Calcium II H&K lines and radial velocity data. Hotter stars (T_{eff} >6200 K) often have shallow convective envelopes and inefficient magnetic dynamos which result in fewer spots on the stellar surface (Kraft, 1967). Therefore, hotter stars like HD 106315 may not have enough starspots for this type of Gaussian process to be effective.

Through our interior composition analysis, we found HD 106315 b requires additional volatiles, consistent with either a 1% hydrogen helium envelope or a moderate water envelope surrounding and Earth-like core. HD 106315 c is consistent with a 13% by mass hydrogen/helium envelope surrounding an Earth-like core.

Part V

Discussion

Chapter 15

Bulk Composition

In this chapter, we provide a summary of the derived properties of each of the planets discussed in Part IV and compare their parameters to those of the confirmed exoplanet sample. The planet parameters are summarized in Table 15.1 and the stellar paramters are summarized in Table 15.2.

We begin by examining the bulk compositions of these eleven planets in the context of other super-Earth and sub-Neptune planets (Figure 15.1). A more detailed composition analysis for each planet is described in its respective section including interpolating over theoretical composition models, photoevaporation timescale calculations, and simulated transmission spectra, as relevant.

The planets in this dissertation fall into three primary groups, those consistent with an Earth-like composition, those consistent with a moderate water envelope or small Hydrogen/Helium envelope, and those similar (in terms of mass and radius) to our Neptune and Uranus. The three planets consistent with an Earth-like composition are

Planet	Period (days)	Radius ($R_\oplus$)	Mass ($M_\oplus$)	Density (g cm^{-3})
K2-291 b	2.225172 ± 0.000070	$1.589^{+0.095}_{-0.072}$	6.49 ± 1.16	$8.8^{+2.5}_{-2.0}$
GJ 3470 b	3.3366413 ± 0.0000060	3.88 ± 0.32	12.6 ± 1.3	$0.93^{+0.56}_{-0.31}$
K2-3 b	10.054626 ± 0.000010	2.13 ± 0.23	6.48 ± 0.99	$3.7^{+1.7}_{-1.1}$
K2-3 c	24.646582 ± 0.000039	1.57 ± 0.14	2.14 ± 1.08	$3.0^{+2.0}_{-1.5}$
K2-3 d	44.556456 ± 0.000097	1.39 ± 0.21	$-0.5^{+1.1}_{-1.2}$	$-1.0^{+2.2}_{-2.8}$
HD 97658 b	9.489295 ± 0.0000050	$2.30^{+0.07}_{-0.14}$	$7.81^{+0.55}_{-0.44}$	$3.78^{+0.61}_{-0.51}$
GJ 9827 b	1.2089765 ± 0.0000023	1.529 ± 0.058	4.87 ± 0.37	$7.47^{+1.1}_{-0.95}$
GJ 9827 c	3.648095 ± 0.000024	1.201 ± 0.046	1.92 ± 0.49	$6.1^{+1.8}_{-1.6}$
GJ 9827 d	6.20183 ± 0.000010	1.955 ± 0.075	3.42 ± 0.62	2.51 ± 0.57
HD 106315 b	9.55288 ± 0.00021	2.40 ± 0.20	10.5 ± 3.1	$4.1^{+1.9}_{-1.4}$
HD 106315 c	21.05652 ± 0.00012	4.379 ± 0.086	12.0 ± 3.8	0.78 ± 0.26

Table 15.1: Summary of Planet Parameters

Star	Mass (M_*)	Radius (R_*)	Temperature	R'$_{HK}$
K2-291	0.934 ± 0.038	0.899 ± 0.035	5520 ± 60	-4.7260
GJ 3470	0.51 ± 0.06	0.48 ± 0.04	3652 ± 50	-4.9000
K2-3	0.601 ± 0.089	0.561 ± 0.068	3900 ± 190	-4.9495
HD 97658	0.77 ± 0.05	$0.746^{+0.016}_{-0.034}$	5192^{+120}_{-55}	-4.9346
GJ 9827	0.593 ± 0.018	0.579 ± 0.019	4294 ± 52	-5.2166
HD 106315	1.154 ± 0.043	1.269 ± 0.024	6364 ± 87	-5.1545

Table 15.2: Summary of Stellar Parameters

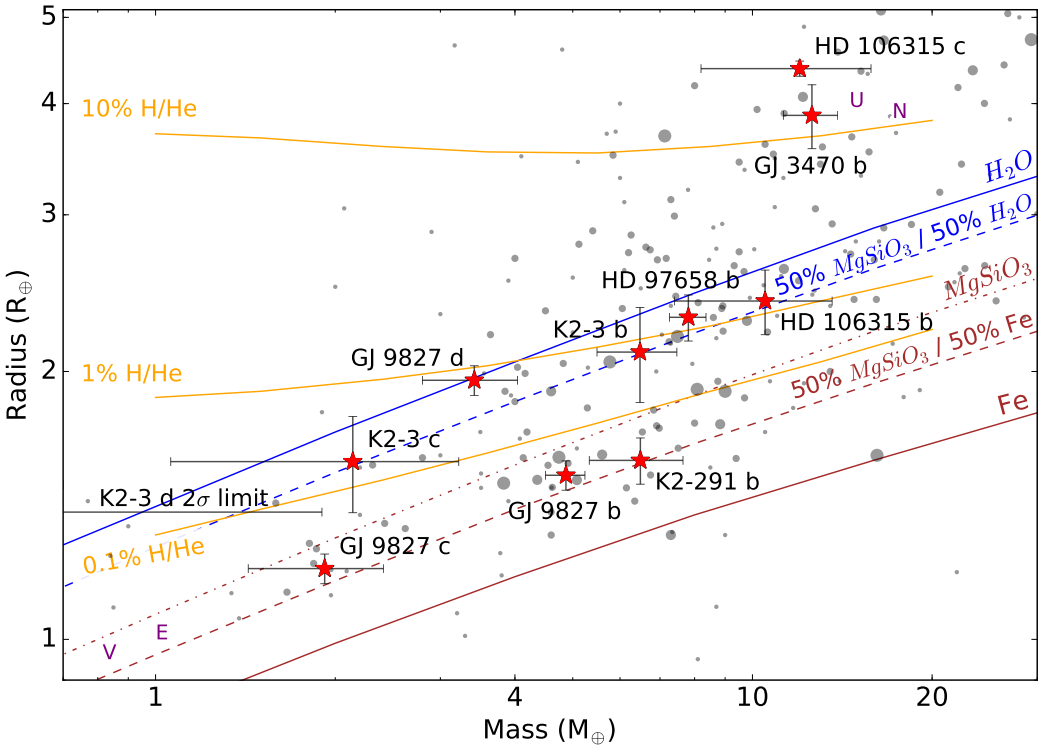

Figure 15.1: Mass-radius diagram for planets between the size of Earth and Neptune (larger points for lower error). The lines show models of different compositions (Zeng et al., 2016; Lopez and Fortney, 2014). The eleven planets highlighted in this dissertation are shown as a red stars along with their 1-σ uncertainties.

K2-291 b (ρ=8.8 g cm^{-3}), GJ 9827 b (ρ=7.5 g cm^{-3}), and GJ 9827 c (ρ=6.1 g cm^{-3}), the smallest planets in our sample. These planets fall between the 100% $MgSiO_3$ and 100% Fe composition curves. They all require heavy element cores and less than a 0.1% H/He envelope.

The group of planets requiring some volatile elements are K2-3 b (ρ=3.7 g cm^{-3}), K2-3 c (ρ=3.0 g cm^{-3}), HD 97658 b (ρ=3.8 g cm^{-3}), GJ 9827 d (ρ=2.5 g cm^{-3}), and HD 106315 b (ρ=4.1 g cm^{-3}). These planets are all consistent with a large mass fraction of water or a small ($\leq$2%) H/He envelope. GJ 9827 d is consistent with either 100% water or a rocky core with a 1% H/He envelope. HD 97658 b, HD 106315 b, and K2-3 b all fall in a very similar space and are consistent with either a 50% water or 1% H/He envelope. K2-3 c falls on the same 50% water line but is consistent with a smaller amount of H/He ($\sim$0.5%) due to its smaller radius.

Lastly, two planets occupy the same mass-radius space as our solar system ice giants, GJ 3470 b (ρ=0.9 g cm^{-3}) and HD 106315 c (ρ=0.8 g cm^{-3}). However, these planets orbit much closer to their host stars than Uranus & Neptune and receive significantly more stellar insolation (GJ 3470 b: 30 $S_\oplus$, HD 106315 c: 96 $S_\oplus$, Uranus: 0.0027 $S_\oplus$, Neptune: 0.0011 $S_\oplus$). Their densities are too low to be explained by water alone; they are consistent with a large (>10%) H/He envelope surrounding an Earth-like core.

Chapter 16

Compositions across the Radius Valley

The planets in this work span a large stellar mass, planet radius, and planet insolation space including multiple planets in or near the radius valley. We compare these planets with the full exoplanet population and find their bulk densities agree with trends found in the literature.

We first compare the seven planets orbiting FGK stars with those discussed in Fulton et al. (2017). Overall, these seven planets follow the trend of decreasing densities with increasing radius (Figure 16.1). The three densest planets, K2-291 b, GJ 9827 b, and GJ 9827 c, all fall below both photoevaporation scaling models of the radius valley (atmospheric loss and gas-poor formation, Lopez and Rice, 2018). These planets orbit within 4 days therefore their high densities are not surprising as their small masses should be unable to maintain a substantial envelope at this insolation flux. The three 2–3 $R_\oplus$ planets all have intermediate densities of 2-3 g cm^{-3}; they occupy a tight orbital period space (5–10 days) however they orbit a wide range of stellar types (F–K stars)

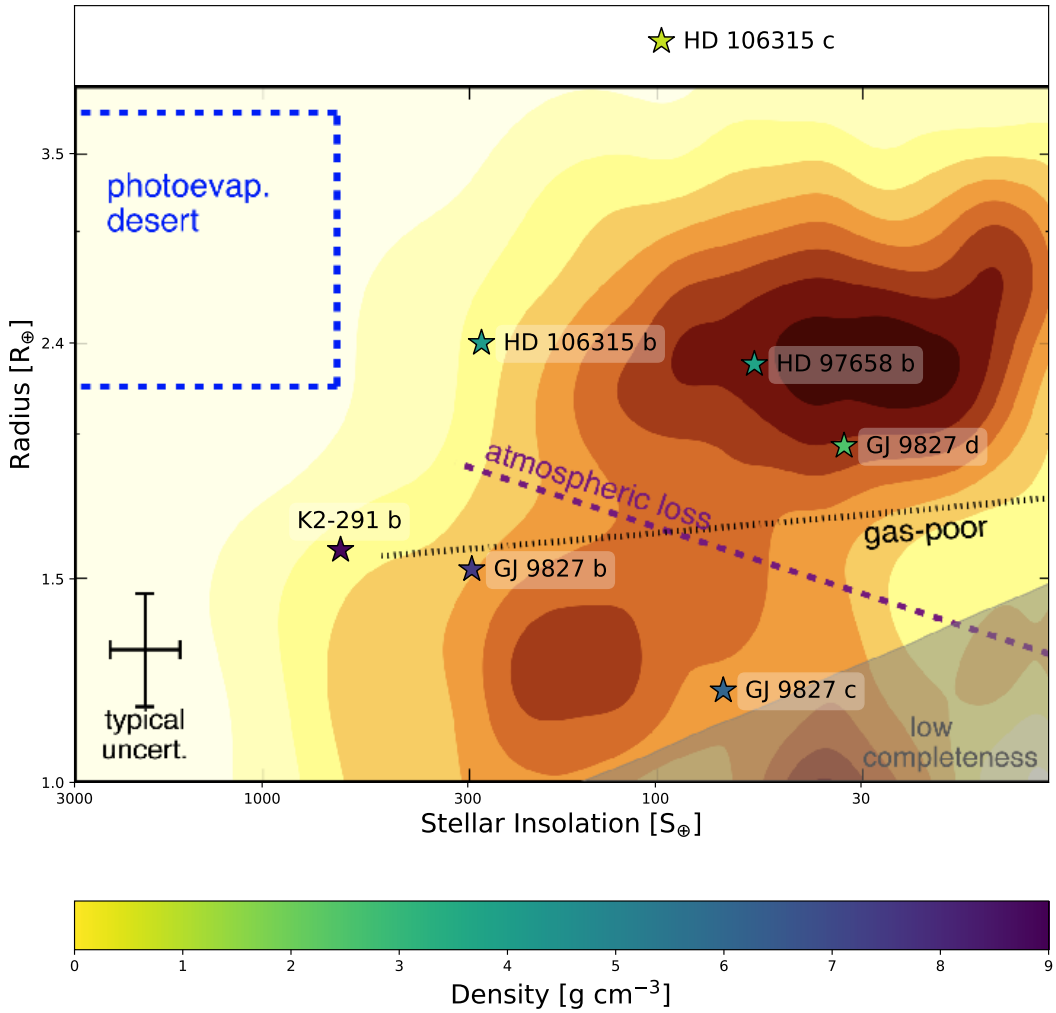

Figure 16.1: Stellar insolation vs. radius diagram with contours and model designations reproduced from Fulton et al. (2017). The seven planets orbiting FGJ stars discussed in this paper are shown as stars colored by their density. The purple and black dashed lines indicate two radius valley predictions from Lopez and Rice (2018) describing atmospheric loss and gas-poor formation. The blue dashed region indicates the photoevaporation desert (Lundkvist et al., 2016). See Fulton et al. (2017) for more details.

resulting in a spread of stellar insolation fluxes from 30–300 $S_\oplus$. The largest planet, HD 106315 c, has the lowest density (<1 g cm^{-3}).

Multiplanet systems offer a unique opportunity to examine trends in planet properties while controlling for stellar properties. Two of our FGK systems are multiplanet systems: GJ 9827 and HD 106315. The three GJ 9827 planets span the radius valley; the inner two planets are high density and smaller than the radius valley (R_b=1.5$R_\oplus$, R_c=1.2$R_\oplus$) whereas the outer planet is lower density and larger than the radius valley (R_d=2.0$R_\oplus$). HD 106315 b and c are both lower density and larger than the radius valley (R_b=2.4$R_\oplus$, R_c=4.4$R_\oplus$). The five planets in these systems agree with the theory that planets smaller than 1.7$R_\oplus$ are primarily composed of rocky cores and larger planets have additional volatile material that contributes to their radii (Weiss et al., 2016; Fulton et al., 2017).

The two main theories for the creation of the radius valley are photoevaporation and core-powered mass-loss, as discussed in Chapter 1. Photoevaporation occurs when stellar radiation heats and ionizes planet hydrogen/helium envelopes resulting in atmospheric loss. Core-powered mass-loss describes how planets start with an initial heat of formation and the cooling process can cause atmospheric loss. Both of these processes result in small rocky planets, larger volatile rich planets, and a lack of planets between the two. These two theories can be tested through measuring the radius valley dependence on other system parameters such as the stellar mass and stellar age. The location of the radius valley depends on the stellar mass (Fulton and Petigura, 2018; Wu, 2019; Berger et al., 2020). Core-powered mass-loss theory suggests that increasing

stellar mass will change the radius valley location as the higher stellar luminosity will increase planet temperatures enabling more massive planets to lose their atmospheres, therefore the radius valley location will move outwards. Gupta and Schlichting (2020) simulates planetary formation including core-powered mass-loss and finds a radius valley slope consistent with the observations. Wu (2019) suggests that photoevaporation can also explain this observation if the characteristic planet mass scales with stellar mass, therefore the radius gap would move larger with increasing stellar mass as observed.

We examine our planet densities as a function of radius and stellar type using the results of Berger et al. (2020) in Figure 16.2. We measured the masses of planets orbiting M, K, G, and F stars therefore the planets span a wide range of the studied stellar mass space. Our five planets with intermediate densities fall near the 1σ range of the measured radius valley from Berger et al. (2020). These planets may be transitioning across the radius valley and therefore losing mass. One could test this theory by looking for signs of atmospheric mass loss for the planets in the radius valley. Kasper et al. (2020) set limits on the atmospheric loss rates for both GJ 9827 d and HD 97658 b through measuring high-resolution transit spectroscopy of the 10833 Å He triplet. As these two planets are not rapidly losing mass, perhaps they are instead stable on an edge of the radius valley.

The slope of the radius valley location in radius-insolation space also changes as a function of stellar type; Martinez et al. (2019) finds a negative slope (-0.11$\pm$0.03) for FGK stars whereas Cloutier and Menou (2020) finds a positive slope for mid K through early M stars (0.058$\pm$0.022). This slope change suggests that the dominant process for

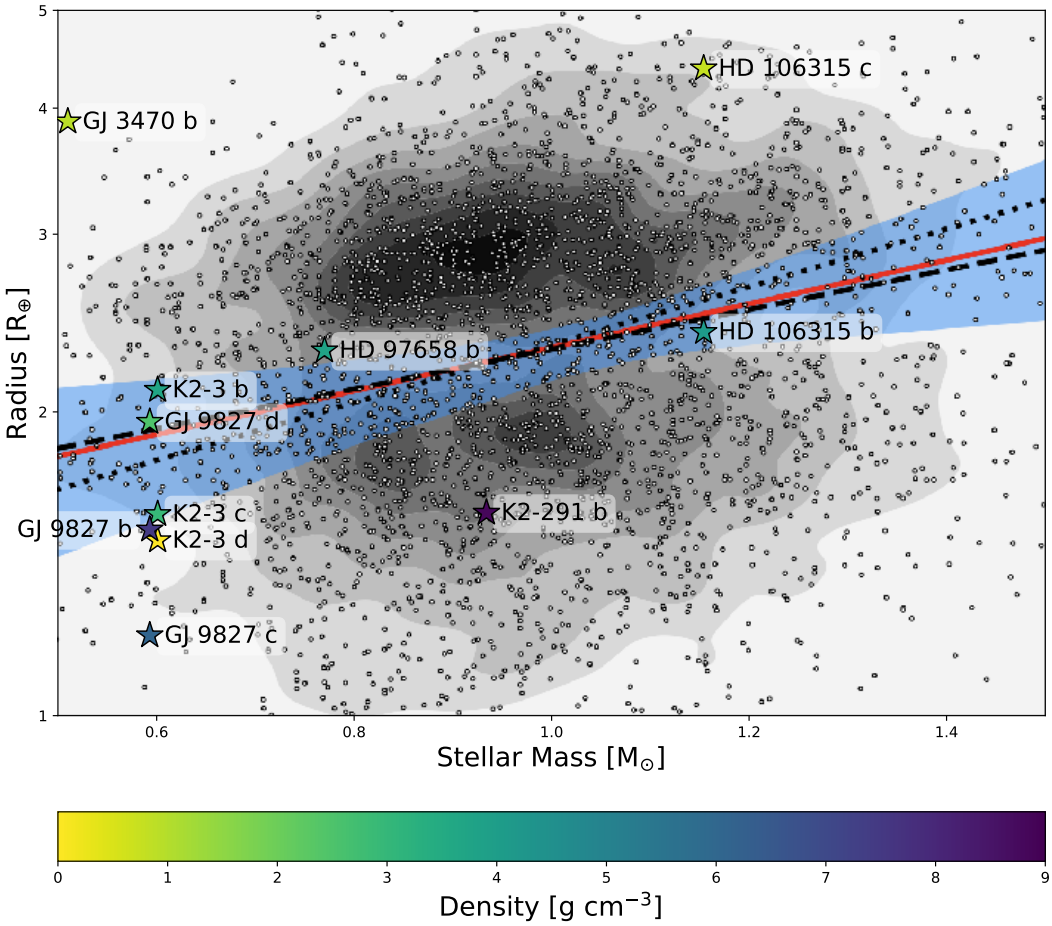

Figure 16.2: Radius valley as a function of stellar mass reproduced from Berger et al. (2020). The eleven planets discussed in this paper are shown as stars colored by their density. As described in Berger et al. (2020), the line of best fit (red line) and 1σ bounds (blue shaded region) is shown along with two model relations between the planet mass and stellar mass (black dashed and black dotted lines, Wu, 2019).

the formation of the radius gap is stellar mass dependent and perhaps that thermally driven mass loss becomes less efficient with lower mass stars. As we measured the masses of eight planets orbiting M and K dwarfs, we additionally examine where these planets fall in comparison to others orbiting small stars (Figure 16.3).

The measured slope from the Cloutier and Menou (2020) sample follows the radius valley as predicted by gas-poor formation (Lopez and Rice, 2018). Perhaps photoevaporation better describes the evolution of planets orbiting hotter stars (Figure 16.1) and gas-poor formation better describes planets orbiting cooler stars (Figure 16.3). Our two densest planets, GJ 9827 b (ρ_b = 7.5 g cm^{-3}) and GJ 9827 c (ρ_b = 6.1 g cm^{-3}), occupy the same space as the other known rocky planets below this measured slope. Our intermediate density planets are clustered around the radius valley as predicted by photoevaporation (Lopez and Rice, 2018) and impact erosion theories (Wu, 2019). Half of these planets, HD 97658 b, GJ 9827 d, and K2-3 b, are above the measured slope along the gas-poor formation radius valley. The other intermediate density planets, K2-3 c and d, fall below the radius valley as predicted by gas-poor formation. GJ 3470 b is larger than the majority of the planets in this sample as a low-density Neptune-sized planet.

The K2-3 planets are of particular interest as their radius and stellar insolation places them near the occurrence peaks of this planet population. Although K2-3 b (R_b = 2.1 $R_\oplus$) and K2-3 c (R_c = 1.6 $R_\oplus$) span across the measured radius valley, they have similar intermediate densities. K2-3 d (R_d = 1.4 $R_\oplus$), the smallest planet in this system, has the lowest inferred density from its non-detection in our radial velocity

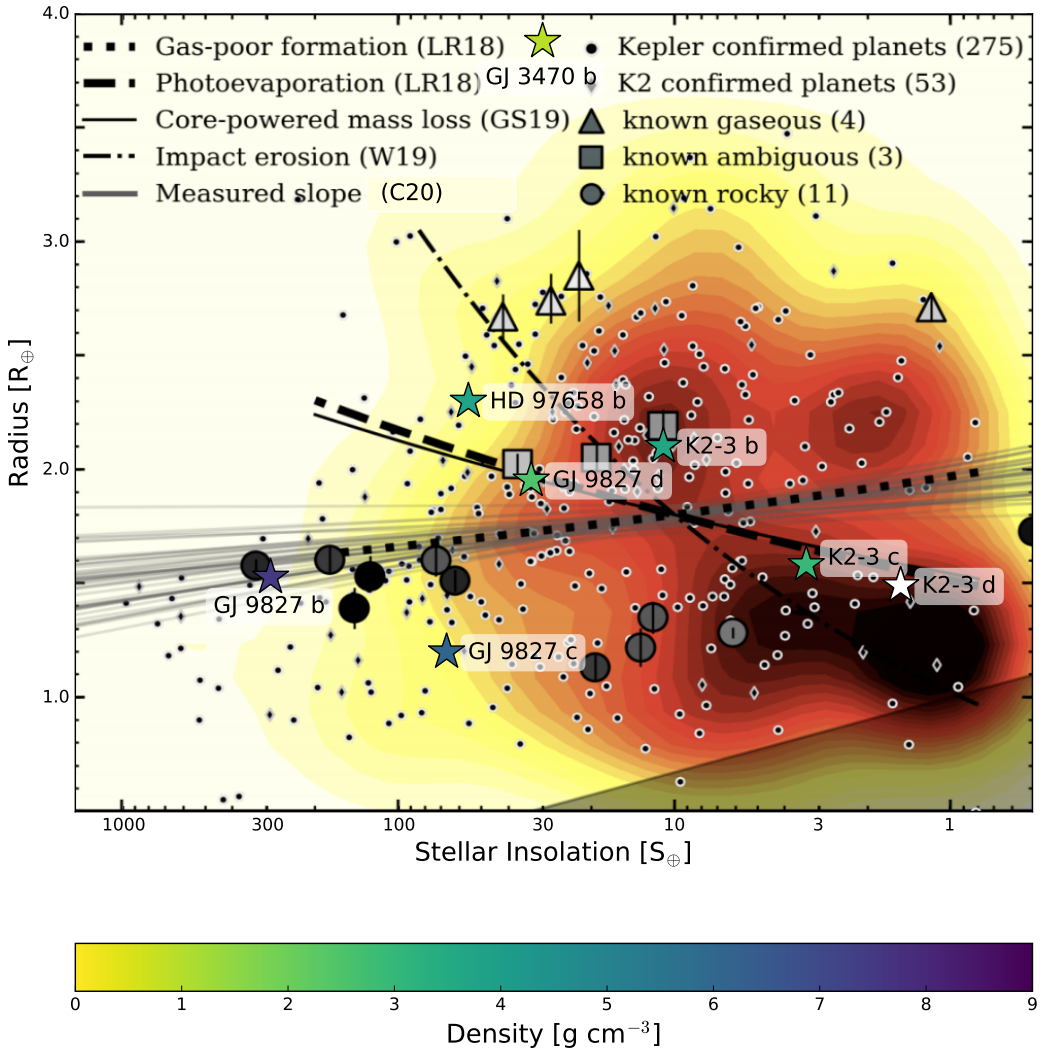

Figure 16.3: Radius valley for mid K through early M stars reproduced from Cloutier and Menou (2020). The eight planets orbiting M and K stars discussed in this paper are shown as stars colored by their density (excluding our non-detection of K2-3 d). As described in Cloutier and Menou (2020), the measured slope (solid grey lines) are shown along with model predictions for the radius valley: gas-poor formation (small dashes, Lopez and Rice, 2018), photoevaporation (large dashes, Lopez and Rice, 2018), core-powered mass-loss (solid line, Gupta and Schlichting, 2019), and impact erosion (dot-dashed line, Wu, 2019).

analysis. Perhaps the masses presented for the K2-3 system are inaccurate due to complicated stellar activity present in the radial velocity data, especially as the stellar rotation period is near the orbital period of K2-3 d. Alternatively, the stellar insolation received by these planets is relatively low (1-15 $S_{\oplus}$); K2-3 c and d are very close to the radius valley as predicted by photoevaporation (Lopez and Rice, 2018). If these planets had a gas-rich formation, they may have been able to retain their hydrogen/helium envelopes and maintain a low density.

Berger et al. (2020) additionally measure the relative occurrences of super-Earths and sub-Neptunes in the two peaks surrounding the radius valley as a function of stellar age. They find their older planet sample (stellar age $>$ 1 Gyr) have a similar relative occurrence between the two peaks and their younger planet sample (stellar age $<$ 1 Gyr) the super-Earth peak is 60% as high as their sub-Neptune peak and the sub-Neptune peak is wider. This height change suggests that sub-Neptunes transition across the radius valley to super-Earth sizes on Gyr timescales. This timescale agrees with core-powered mass-loss theories (Gupta and Schlichting, 2020) and has been shown to match results from photoevaporation simulations also (Rogers and Owen, 2021).

The location of the radius valley can additionally inform our understanding of planetary core compositions. If the valley is caused primarily by core-powered mass-loss, then the location of the two peaks is consistent with rock dominated cores (Gupta and Schlichting, 2019). However, formation models suggest that sub-Neptunes are formed outside of the snow line which would result in water rich planets (e.g. Alibert et al., 2013; Coleman and Nelson, 2014; Bitsch et al., 2019). Through additional formation

simulations, Venturini et al. (2020a,b) are unable to match the radius valley location and relative occurrences with only rocky material. They find rocky cores are able to form and populate the smaller peak in the radius distribution however rocky sub-Neptunes are an uncommon result of their simulation. The water rich cores form larger than the rocky cores, however they accrete a significant atmosphere which substantially increases their radius and initially broadens the sub-Neptune distribution peak, creating a substantial number of Neptune-sized planets inconsistent with observations. These larger planets require evolutionary processes to reduce their atmosphere sizes, such as photoevaporation or giant impacts (e.g. Inamdar and Schlichting, 2015), to match the radius distribution. Perhaps the radius valley observations require a combination of both core-powered mass-loss and photoevaporation processes.

Chapter 17

Gaussian Processes in Literature Radial Velocity Analyses

Many of the systems discussed in this work showed clear stellar activity contamination in the radial velocity data which we accounted for using a Gaussian process informed from either Calcium II H & K line measurements or additional photometry.

The solar data work (Chapter 8) provides evidence that the solar activity present in radial velocity data can be well characterized by solar photometry and the timescales can be accurately described through a Gaussian process. Stellar activity in radial velocity data is produced by various stellar surface processes; the types and strength of activity present varies with stellar type. To investigate whether these findings can be applied to other stellar types, we performed an extensive literature search on the use of Gaussian processes in radial velocity analyses to investigate the stellar types used with this method thus far.

Host Star	Effective Temperature (K)	Source
Proxima Centauri	3050 ± 100	Damasso and Del Sordo (2017); Suárez Mascareño et al. (2020)
YZ Ceti	3056 ± 60	Stock et al. (2020)
GJ 876	3129 ± 19	Millholland et al. (2018)
GJ 1132	3270 ± 140	Cloutier et al. (2017)
L 98-59	3412 ± 49	Cloutier et al. (2019)
GJ 251	3451 ± 51	Stock et al. (2020)
GJ 3470	3600 ± 100	Kosiarek et al. (2019a)
GL 411	3601 ± 51	Díaz et al. (2019); Stock et al. (2020)
GJ 15A	3607 ± 68	Pinamonti et al. (2018)
Gl 686	3663 ± 68	Affer et al. (2019)
AU Mic	3700 ± 100	Klein et al. (2021)
GJ 685	3816 ± 69	Pinamonti et al. (2019)
GJ 3942	3867 ± 69	Perger et al. (2017)
K2-3	3896 ± 189	Damasso et al. (2018); Kosiarek et al. (2019a)
γ Draconis	3990 ± 42	Hatzes et al. (2018); Ramirez Delgado and Dodson-Robinson (2020)
HD 238090	3933 ± 51	Stock et al. (2020)
V830 Tau	4250 ± 50	Donati et al. (2017)
GJ 9827	4340 ± 50	Dai et al. (2019); Kosiarek et al. (2021)
K2-216	4503 ± 69	Persson et al. (2018)
K2-141	4599 ± 79	Malavolta et al. (2018); Dai et al. (2019)
K2-36	4916 ± 36	Damasso et al. (2019)
HD 13808	5035 ± 50	Ahrer et al. (2021)
Kepler-78	5089 ± 50	Grunblatt et al. (2015); Dai et al. (2019)
HD 15337	5125 ± 50	Dumusque et al. (2019)

Table 17.1: Literature Radial Velocity Analyses with Gaussian Processes Part 1

Host Star	Effective Temperature (K)	Source
55 Cnc	5196 ± 24	Dai et al. (2019)
K2-131	5245 ± 50	Dai et al. (2017, 2019)
CoRoT-7	5275 ± 75	Haywood et al. (2014); Dai et al. (2019)
K2-229	5315 ± 33	Santerne et al. (2018); Dai et al. (2019)
K2-263	5368 ± 44	Mortier et al. (2018)
HD 164922	5390 ± 30	Benatti et al. (2020)
K2-106	5496 ± 46	Dai et al. (2019)
HD 3167	5528 ± 162	Dai et al. (2019)
Kepler 538	5547 ± 50	Mayo et al. (2019)
Wasp-47	5552 ± 75	Dai et al. (2019)
Kepler-10	5708 ± 28	Haywood (2015); Dai et al. (2019)
HD 110113	5732 ± 50	Osborn et al. (2021)
K2-291	5753 ± 50	Kosiarek et al. (2019b); Dai et al. (2019)
Sun	5780	Kosiarek and Crossfield (2020); Langellier et al. (2020)
K2-100	6168 ± 62	Barragán et al. (2019)
HD 106315	6364 ± 87	Barros et al. (2017)
β Pictoris	7100 ± 285	Vandal et al. (2020)
Vega	9660 ± 90	Hurt et al. (2021)

Table 17.2: Literature Radial Velocity Analyses with Gaussian Processes Part 2

We find that 42 systems have used Gaussian processes so far, a full list is located in Table 17.1. This analysis includes all papers listed on `https://ui.adsabs.harvard.edu/` published before February 2021 including "Gaussian process" and "radial velocity" in their abstract that perform a fit on radial velocity data including a Gaussian process in the paper. We also include papers found while performing general literature searches for this thesis without the abstract terms if the paper performs a Gaussian process analysis on radial velocity data.

The stars in this list span a wide range of temperatures: from 3050 K (M5V) to 9660 K (A0V, Table 4 in Pecaut and Mamajek, 2013). The sample has a mean of 4788 K and standard deviation of 1265 K (Figure 17.1). There is a sharp reduction of systems studied with a Gaussian process around the temperature of the Sun ($T_{\rm eff} = 5780$ K) and the Kraft break ($T_{\rm eff} > 6200$ K), perhaps suggesting that this analysis is best suited for cool stars.

The three stars hotter than the Kraft break with published Gaussian process analyses all have unique situations. For the hottest star, Vega, Hurt et al. (2021) note that the model is over-fitting the data and therefore the Gaussian process model is likely too complex for their needs. For β Pictoris, the Gaussian process model was used to mitigate the δ Scuti pulsations, which is a different stellar surface process than the Gaussian process is aiming to characterize for the other systems (Vandal et al., 2020). And finally, Barros et al. (2017) uses a Gaussian process to analyse HD 106315 radial velocity data however our independent analysis of this system does not find that the use a Gaussian process is statistically justified (Kosiarek et al., 2021).

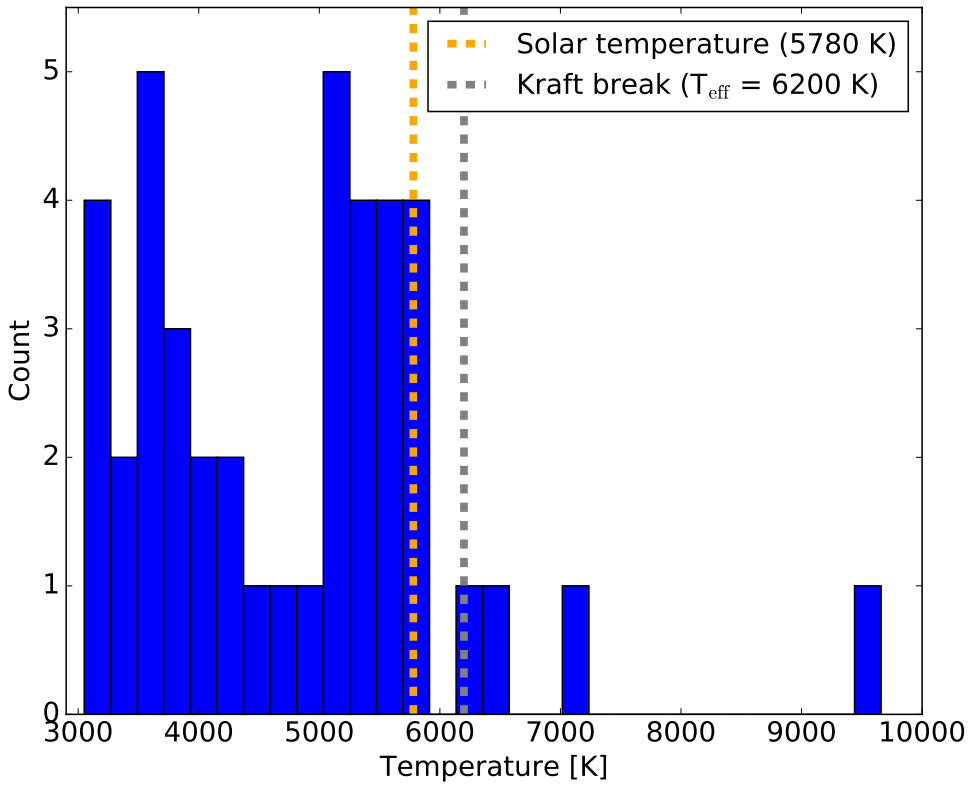

Figure 17.1: Temperature histogram of literature systems using a Gaussian process in their radial velocity analysis. There are very few hot stars in this sample; only three have temperatures higher than the Kraft break.

These systems have selection effects influenced from transiting planet searches and radial velocity data collection feasibility. The transit depth of a particular size planet increases as stellar radius decreases, therefore it is easier to detect planets around smaller stars. The Kepler mission focused on solar-type stars and the TESS mission is surveying M–F stars. Collecting radial velocity data for measuring planet masses is easiest for less active stars and bright stars. The amplitude of the planet signal depends on the planet mass relative to the stellar mass and the orbital period; radial velocity analyses are more sensitive to larger planets, planets orbiting small stars, and plants with low orbital periods. These factors would result in a larger sample of planets orbiting cool stars.

However, there are also reasons that Gaussian process analyses would be less effective for hotter stars. The quasi-period kernel (Equation 7.1) used in many radial velocity analyses well fits stellar rotation with slowly evolving surface features such as star spots. Gaussian processes are often informed from additional data sources such as stellar photometry, in order for this to work there must be clear activity signals in both types of datasets. The shallow convective envelopes and inefficient magnetic dynamos of hotter stars results in less star spots than cooler stars, therefore there may not be clear rotation signals for the Gaussian process to model.

Gaussian processes seem to be an effective way to characterize stellar activity in the Sun and simulated solar data (Kosiarek and Crossfield, 2020; Langellier et al., 2020). For a simulated M dwarf star, Perger et al. (2021) finds that the quasi-periodic kernel is able to determine the injected stellar rotation period and spot lifetime. This

suggests that Gaussian process analyses on observed radial velocity data from M dwarf stars will effectively account for the stellar activity. They additionally find that adding an additional cosine term improves the parameter recovery, therefore suggest using a quasi-period with cosine kernel in the future. Further work is needed to determine the effectiveness of Gaussian process analysis on radial velocity data for other stellar types.

Part VI

Conclusion

Chapter 18

Conclusions

In this dissertation, we examined the effectiveness of using a Gaussian process to characterize stellar activity in solar photometry and radial velocity data. Using this technique, we performed radial velocity analyses for six exoplanet systems hosting eleven transiting planets to improve their mass measurements and infer their compositions.

Our solar work (Chapter 8) focused on determining the ability of a Gaussian process to characterize stellar activity in photometry and radial velocity data. We found that a Gaussian process could provide more reliable estimates of the solar rotation period than a periodogram or autocorrelation analysis. For simultaneous photometry, activity indicators, and radial velocity data, we found similar Gaussian process posteriors suggesting that both photometry and activity indicators can provide useful information on stellar activity present in radial velocity data.

We measured the masses of eleven planets in six exoplanet systems to inform models on their compositions and prepare for atmospheric characterization. In summary,

four of the systems, K2-291 (Chapter 9), GJ 3470 (Chapter 10), K2-3 (Chapter 11), and GJ 9827 (Chapter 13), displayed signs of stellar activity influence in the radial velocity data at the stellar rotation period and we therefore mitigated this activity through a Gaussian process. One of the systems, HD 97658 (Chapter 12), had a clear stellar signal which we associated with the star's magnetic cycle and mitigated through an additional sinusoid. The final system, HD 106315 (Chapter 14), had a high jitter term which implies additional activity in the system, however the high stellar temperature and low spot coverage challenged our ability to use a Gaussian process for this analysis and we therefore adopted the Keplerian-only fit. We predict that this Gaussian process method is applicable to spot-dominated stellar surfaces and therefore not advisable for stars hotter than the Kraft break ($T_{eff} > 6200$ K, Chapter 17).

These planets range from Earth-sized to Neptune-sized, the majority cluster around the radius valley. Their compositions are consistent with photoevaporation and core-powered mass-loss theories suggesting that small planets are primarily rocky, larger planets have a volatile envelope, and that the transition between the two groups is within 1.5–2.0 $R_\oplus$ (Chapters 15 and 16). Many properties of exoplanet atmospheres for planets on either side of the radius valley are still open questions. There is much to learn about atmospheric composition, role and compositions of clouds, planetary albedo, and atmospheric evolution. Multiple planets in this sample are excellent targets for atmospheric characterization including six with completed or planned transmission spectra observations with HST or JWST. These planets will be valuable towards understanding atmospheric physical and chemical processes.

Bibliography

Affer, L., Damasso, M., Micela, G., Poretti, E., Scand ariato, G., Maldonado, J., Lanza, A. F., Covino, E., Garrido Rubio, A., González Hernández, J. I., Gratton, R., Leto, G., Maggio, A., Perger, M., Sozzetti, A., Suárez Mascareño, A., Bonomo, A. S., Borsa, F., Claudi, R., Cosentino, R., Desidera, S., Giacobbe, P., Molinari, E., Pedani, M., Pinamonti, M., Rebolo, R., Ribas, I., and Toledo-Padrón, B. (2019). HADES RV program with HARPS-N at the TNG. IX. A super-Earth around the M dwarf Gl 686. *A&A*, 622:A193.

Ahrer, E., Queloz, D., Rajpaul, V. M., Ségransan, D., Bouchy, F., Hall, R., Handley, W., Lovis, C., Mayor, M., Mortier, A., Pepe, F., Thompson, S., Udry, S., and Unger, N. (2021). The HARPS search for southern extra-solar planets XLV. Two Neptune mass planets orbiting HD13808: a study of stellar activity modelling's impact on planet detection. *MNRAS*.

Aigrain, S., Parviainen, H., and Pope, B. J. S. (2016). K2SC: flexible systematics correction and detrending of K2 light curves using Gaussian process regression. *MNRAS*, 459:2408–2419.

Aigrain, S., Pont, F., and Zucker, S. (2012). A simple method to estimate radial velocity variations due to stellar activity using photometry. *MNRAS*, 419(4):3147–3158.

Albrecht, S., Winn, J. N., Marcy, G. W., Howard, A. W., Isaacson, H., and Johnson, J. A. (2013). Low Stellar Obliquities in Compact Multiplanet Systems. *ApJ*, 771(1):11.

Alibert, Y., Carron, F., Fortier, A., Pfyffer, S., Benz, W., Mordasini, C., and Swoboda, D. (2013). Theoretical models of planetary system formation: mass vs. semi-major axis. *A&A*, 558:A109.

Almenara, J. M., Astudillo-Defru, N., Bonfils, X., Forveille, T., Santerne, A., Albrecht, S., Barros, S. C. C., Bouchy, F., Delfosse, X., Demangeon, O., Diaz, R. F., Hébrard, G., Mayor, M., Neves, V., Rojo, P., Santos, N. C., and Wünsche, A. (2015). A HARPS view on K2-3. *A&A*, 581:L7.

Angus, R., Morton, T., Aigrain, S., Foreman-Mackey, D., and Rajpaul, V. (2018). Inferring probabilistic stellar rotation periods using Gaussian processes. *MNRAS*, 474(2):2094–2108.

Astudillo-Defru, N., Bonfils, X., Delfosse, X., Ségransan, D., Forveille, T., Bouchy, F., Gillon, M., Lovis, C., Mayor, M., Neves, V., Pepe, F., Perrier, C., Queloz, D., Rojo, P., Santos, N. C., and Udry, S. (2015). The HARPS search for southern extra-solar planets. XXXVI. Planetary systems and stellar activity of the M dwarfs GJ 3293, GJ 3341, and GJ 3543. *A&A*, 575:A119.

Astudillo-Defru, N., Forveille, T., Bonfils, X., Ségransan, D., Bouchy, F., Delfosse, X., Lovis, C., Mayor, M., Murgas, F., Pepe, F., Santos, N. C., Udry, S., and Wünsche, A. (2017). The HARPS search for southern extra-solar planets. XLI. A dozen planets around the M dwarfs GJ 3138, GJ 3323, GJ 273, GJ 628, and GJ 3293. *A&A*, 602:A88.

Ballard, S. (2019). Predicted Number, Multiplicity, and Orbital Dynamics of TESS M-dwarf Exoplanets. *AJ*, 157(3):113.

Baranne, A., Queloz, D., Mayor, M., Adrianzyk, G., Knispel, G., Kohler, D., Lacroix, D., Meunier, J.-P., Rimbaud, G., and Vin, A. (1996). ELODIE: A spectrograph for accurate radial velocity measurements. *A&AS*, 119:373–390.

Barragán, O., Aigrain, S., Kubyshkina, D., Gand olfi, D., Livingston, J., Fridlund, M. C. V., Fossati, L., Korth, J., Parviainen, H., Malavolta, L., Palle, E., Deeg, H. J., Nowak, G., Rajpaul, V. M., Zicher, N., Antoniciello, G., Narita, N., Albrecht, S., Bedin, L. R., Cabrera, J., Cochran, W. D., de Leon, J., Eigmüller, P., Fukui, A., Granata, V., Grziwa, S., Guenther, E., Hatzes, A. P., Kusakabe, N., Latham, D. W., Libralato, M., Luque, R., Montañés-Rodríguez, P., Murgas, F., Nardiello, D., Pagano, I., Piotto, G., Persson, C. M., Redfield, S., and Tamura, M. (2019). Radial velocity confirmation of K2-100b: a young, highly irradiated, and low-density transiting hot Neptune. *MNRAS*, 490(1):698–708.

Barros, S. C. C., Gosselin, H., Lillo-Box, J., Bayliss, D., Delgado Mena, E., Brugger, B., Santerne, A., Armstrong, D. J., Adibekyan, V., Armstrong, J. D., Barrado, D., Bento, J., Boisse, I., Bonomo, A. S., Bouchy, F., Brown, D. J. A., Cochran, W. D., Collier

Cameron, A., Deleuil, M., Demangeon, O., Díaz, R. F., Doyle, A., Dumusque, X., Ehrenreich, D., Espinoza, N., Faedi, F., Faria, J. P., Figueira, P., Foxell, E., Hébrard, G., Hojjatpanah, S., Jackman, J., Lendl, M., Ligi, R., Lovis, C., Melo, C., Mousis, O., Neal, J. J., Osborn, H. P., Pollacco, D., Santos, N. C., Sefako, R., Shporer, A., Sousa, S. G., Triaud, A. H. M. J., Udry, S., Vigan, A., and Wyttenbach, A. (2017). Precise masses for the transiting planetary system HD 106315 with HARPS. *A&A*, 608:A25.

Batalha, N. E., Kempton, E. M.-R., and Mbarek, R. (2017a). Challenges to Constraining Exoplanet Masses via Transmission Spectroscopy. *ApJ*, 836:L5.

Batalha, N. E., Lewis, T., Fortney, J. J., Batalha, N. M., Kempton, E., Lewis, N. K., and Line, M. R. (2019). The Precision of Mass Measurements Required for Robust Atmospheric Characterization of Transiting Exoplanets. *ApJ*, 885(1):L25.

Batalha, N. E., Mandell, A., Pontoppidan, K., Stevenson, K. B., Lewis, N. K., Kalirai, J., Earl, N., Greene, T., Albert, L., and Nielsen, L. D. (2017b). PandExo: A Community Tool for Transiting Exoplanet Science with JWST & HST. *PASP*, 129(6):064501.

Beichman, C., Livingston, J., Werner, M., Gorjian, V., Krick, J., Deck, K., Knutson, H., Wong, I., Petigura, E., Christiansen, J., Ciardi, D., Greene, T. P., Schlieder, J. E., Line, M., Crossfield, I., Howard, A., and Sinukoff, E. (2016). Spitzer Observations of Exoplanets Discovered with the Kepler K2 Mission. *ApJ*, 822:39.

Benatti, S., Damasso, M., Desidera, S., Marzari, F., Biazzo, K., Claudi, R., Di Mauro, M. P., Lanza, A. F., Pinamonti, M., Barbato, D., Malavolta, L., Poretti, E., Sozzetti,

A., Affer, L., Bignamini, A., Bonomo, A. S., Borsa, F., Brogi, M., Bruno, G., Carleo, I., Cosentino, R., Covino, E., Frustagli, G., Giacobbe, P., Gonzalez, M., Gratton, R., Harutyunyan, A., Knapic, C., Leto, G., Lodi, M., Maggio, A., Maldonado, J., Mancini, L., Martinez Fiorenzano, A., Micela, G., Molinari, E., Molinaro, M., Nardiello, D., Nascimbeni, V., Pagano, I., Pedani, M., Piotto, G., Rainer, M., and Scandariato, G. (2020). The GAPS programme at TNG. XXIII. HD 164922 d: close-in super-Earth discovered with HARPS-N in a system with a long-period Saturn mass companion. *A&A*, 639:A50.

Benneke, B., Knutson, H. A., Lothringer, J., Crossfield, I. J. M., Moses, J. I., Morley, C., Kreidberg, L., Fulton, B. J., Dragomir, D., Howard, A. W., Wong, I., Désert, J.-M., McCullough, P. R., Kempton, E. M. R., Fortney, J., Gilliland, R., Deming, D., and Kammer, J. (2019). A sub-Neptune exoplanet with a low-metallicity methane-depleted atmosphere and Mie-scattering clouds. *Nature Astronomy*, 3:813–821.

Benneke, B. and Seager, S. (2013). How to Distinguish between Cloudy Mini-Neptunes and Water/Volatile-dominated Super-Earths. *ApJ*, 778(2):153.

Berger, T. A., Huber, D., Gaidos, E., van Saders, J. L., and Weiss, L. M. (2020). The Gaia-Kepler Stellar Properties Catalog. II. Planet Radius Demographics as a Function of Stellar Mass and Age. *AJ*, 160(3):108.

Biddle, L. I., Pearson, K. A., Crossfield, I. J. M., Fulton, B. J., Ciceri, S., Eastman, J., Barman, T., Mann, A. W., Henry, G. W., Howard, A. W., Williamson, M. H., Sinukoff, E., Dragomir, D., Vican, L., Mancini, L., Southworth, J., Greenberg, A.,

Turner, J. D., Thompson, R., Taylor, B. W., Levine, S. E., and Webber, M. W. (2014). Warm ice giant GJ 3470b - II. Revised planetary and stellar parameters from optical to near-infrared transit photometry. *MNRAS*, 443:1810–1820.

Birkby, J. L., de Kok, R. J., Brogi, M., de Mooij, E. J. W., Schwarz, H., Albrecht, S., and Snellen, I. A. G. (2013). Detection of water absorption in the day side atmosphere of HD 189733 b using ground-based high-resolution spectroscopy at 3.2μm. *MNRAS*, 436:L35–L39.

Bitsch, B., Raymond, S. N., and Izidoro, A. (2019). Rocky super-Earths or waterworlds: the interplay of planet migration, pebble accretion, and disc evolution. *A&A*, 624:A109.

Blackman, R. T., Fischer, D. A., Jurgenson, C. A., Sawyer, D., McCracken, T. M., Szymkowiak, A. E., Petersburg, R. R., Ong, J. M. J., Brewer, J. M., Zhao, L. L., Leet, C., Buchhave, L. A., Tronsgaard, R., Llama, J., Sawyer, T., Davis, A. B., Cabot, S. H. C., Shao, M., Trahan, R., Nemati, B., Genoni, M., Pariani, G., Riva, M., Fournier, P., and Pawluczyk, R. (2020). Performance Verification of the EXtreme PREcision Spectrograph. *AJ*, 159(5):238.

Boisse, I., Bouchy, F., Hébrard, G., Bonfils, X., Santos, N., and Vauclair, S. (2011). Disentangling between stellar activity and planetary signals. *A&A*, 528:A4.

Bonfils, X., Gillon, M., Udry, S., Armstrong, D., Bouchy, F., Delfosse, X., Forveille, T., Fumel, A., Jehin, E., Lendl, M., Lovis, C., Mayor, M., McCormac, J., Neves, V., Pepe, F., Perrier, C., Pollaco, D., Queloz, D., and Santos, N. C. (2012). A hot Uranus

transiting the nearby M dwarf GJ 3470. Detected with HARPS velocimetry. Captured in transit with TRAPPIST photometry. *A&A*, 546:A27.

Brewer, J. M., Fischer, D. A., Valenti, J. A., and Piskunov, N. (2016). Spectral Properties of Cool Stars: Extended Abundance Analysis of 1,617 Planet-search Stars. *ApJS*, 225:32.

Buccino, A. P., Díaz, R. F., Luoni, M. L., Abrevaya, X. C., and Mauas, P. J. D. (2011). Long-term Chromospheric Activity in Southern M Dwarfs: Gl 229 a and Gl 752 A. *AJ*, 141:34.

Butler, R. P., Marcy, G. W., Williams, E., McCarthy, C., Dosanjh, P., and Vogt, S. S. (1996). Attaining Doppler Precision of 3 M s-1. *PASP*, 108:500.

Cegla, H. M., Watson, C. A., Shelyag, S., Mathioudakis, M., and Moutari, S. (2019). Stellar Surface Magnetoconvection as a Source of Astrophysical Noise. III. Sun-as-a-Star Simulations and Optimal Noise Diagnostics. *ApJ*, 879(1):55.

Chaplin, W. J., Cegla, H. M., Watson, C. A., Davies, G. R., and Ball, W. H. (2019). Filtering Solar-Like Oscillations for Exoplanet Detection in Radial Velocity Observations. *AJ*, 157(4):163.

Charbonneau, D., Brown, T. M., Noyes, R. W., and Gilliland, R. L. (2002). Detection of an Extrasolar Planet Atmosphere. *ApJ*, 568(1):377–384.

Chen, H. and Rogers, L. A. (2016). Evolutionary Analysis of Gaseous Sub-Neptune-mass Planets with MESA. *ApJ*, 831(2):180.

Cincunegui, C., Díaz, R. F., and Mauas, P. J. D. (2007). Hα and the Ca II H and K lines as activity proxies for late-type stars. *A&A*, 469:309–317.

Cloutier, R., Astudillo-Defru, N., Bonfils, X., Jenkins, J. S., Berdiñas, Z., Ricker, G., Vand erspek, R., Latham, D. W., Seager, S., Winn, J., Jenkins, J. M., Almenara, J. M., Bouchy, F., Delfosse, X., Díaz, M. R., Díaz, R. F., Doyon, R., Figueira, P., Forveille, T., Kurtovic, N. T., Lovis, C., Mayor, M., Menou, K., Morgan, E., Morris, R., Muirhead, P., Murgas, F., Pepe, F., Santos, N. C., Ségransan, D., Smith, J. C., Tenenbaum, P., Torres, G., Udry, S., Vezie, M., and Villasenor, J. (2019). Characterization of the L 98-59 multi-planetary system with HARPS. Mass characterization of a hot super-Earth, a sub-Neptune, and a mass upper limit on the third planet. *A&A*, 629:A111.

Cloutier, R., Doyon, R., Menou, K., Delfosse, X., Dumusque, X., and Artigau, É. (2017). On the Radial Velocity Detection of Additional Planets in Transiting, Slowly Rotating M-dwarf Systems: The Case of GJ 1132. *AJ*, 153(1):9.

Cloutier, R. and Menou, K. (2020). Evolution of the Radius Valley around Low-mass Stars from Kepler and K2. *AJ*, 159(5):211.

Coleman, G. A. L. and Nelson, R. P. (2014). On the formation of planetary systems via oligarchic growth in thermally evolving viscous discs. *MNRAS*, 445(1):479–499.

Collier Cameron, A., Mortier, A., Phillips, D., Dumusque, X., Haywood, R. D., Langellier, N., Watson, C. A., Cegla, H. M., Costes, J., Charbonneau, D., Coffinet, A., Latham, D. W., Lopez-Morales, M., Malavolta, L., Maldonado, J., Micela, G., Milbourne, T.,

Molinari, E., Saar, S. H., Thompson, S., Buchschacher, N., Cecconi, M., Cosentino, R., Ghedina, A., Glenday, A., Gonzalez, M., Li, C.-H., Lodi, M., Lovis, C., Pepe, F., Poretti, E., Rice, K., Sasselov, D., Sozzetti, A., Szentgyorgyi, A., Udry, S., and Walsworth, R. (2019). Three years of Sun-as-a-star radial-velocity observations on the approach to solar minimum. *MNRAS*, 487:1082–1100.

Cosentino, R., Lovis, C., Pepe, F., Cameron, A. C., Latham, D. W., Molinari, E., Udry, S., Bezawada, N., Buchschacher, N., Figueira, P., Fleury, M., Ghedina, A., Glenday, A. G., Gonzalez, M., Guerra, J., Henry, D., Hughes, I., Maire, C., Motalebi, F., and Phillips, D. F. (2014). HARPS-N @ TNG, two year harvesting data: performances and results. In *Ground-based and Airborne Instrumentation for Astronomy V*, volume 9147 of *Proc. SPIE*, page 91478C.

Cosentino, R., Lovis, C., Pepe, F., Collier Cameron, A., Latham, D. W., Molinari, E., Udry, S., Bezawada, N., Black, M., Born, A., Buchschacher, N., Charbonneau, D., Figueira, P., Fleury, M., Galli, A., Gallie, A., Gao, X., Ghedina, A., Gonzalez, C., Gonzalez, M., Guerra, J., Henry, D., Horne, K., Hughes, I., Kelly, D., Lodi, M., Lunney, D., Maire, C., Mayor, M., Micela, G., Ordway, M. P., Peacock, J., Phillips, D., Piotto, G., Pollacco, D., Queloz, D., Rice, K., Riverol, C., Riverol, L., San Juan, J., Sasselov, D., Segransan, D., Sozzetti, A., Sosnowska, D., Stobie, B., Szentgyorgyi, A., Vick, A., and Weber, L. (2012). Harps-N: the new planet hunter at TNG. In *Ground-based and Airborne Instrumentation for Astronomy IV*, volume 8446 of *Proc. SPIE*, page 84461V.

Crane, J. D., Shectman, S. A., and Butler, R. P. (2006). The Carnegie Planet Finder Spectrograph. In *Society of Photo-Optical Instrumentation Engineers (SPIE) Conference Series*, volume 6269 of *Society of Photo-Optical Instrumentation Engineers (SPIE) Conference Series*, page 626931.

Crane, J. D., Shectman, S. A., Butler, R. P., Thompson, I. B., Birk, C., Jones, P., and Burley, G. S. (2010). The Carnegie Planet Finder Spectrograph: integration and commissioning. In *Ground-based and Airborne Instrumentation for Astronomy III*, volume 7735 of *Society of Photo-Optical Instrumentation Engineers (SPIE) Conference Series*, page 773553.

Crane, J. D., Shectman, S. A., Butler, R. P., Thompson, I. B., and Burley, G. S. (2008). The Carnegie Planet Finder Spectrograph: a status report. In *Ground-based and Airborne Instrumentation for Astronomy II*, volume 7014 of *Society of Photo-Optical Instrumentation Engineers (SPIE) Conference Series*, page 701479.

Crossfield, I. J. M., Barman, T., Hansen, B. M. S., and Howard, A. W. (2013). Warm ice giant GJ 3470b. I. A flat transmission spectrum indicates a hazy, low-methane, and/or metal-rich atmosphere. *A&A*, 559:A33.

Crossfield, I. J. M., Ciardi, D. R., Isaacson, H., Howard, A. W., Petigura, E. A., Weiss, L. M., Fulton, B. J., Sinukoff, E., Schlieder, J. E., Mawet, D., Ruane, G., de Pater, I., de Kleer, K., Davies, A. G., Christiansen, J. L., Dressing, C. D., Hirsch, L., Benneke, B., Crepp, J. R., Kosiarek, M., Livingston, J., Gonzales, E., Beichman, C. A., and

Knutson, H. A. (2017). Two Small Transiting Planets and a Possible Third Body Orbiting HD 106315. *AJ*, 153(6):255.

Crossfield, I. J. M., Ciardi, D. R., Petigura, E. A., Sinukoff, E., Schlieder, J. E., Howard, A. W., Beichman, C. A., Isaacson, H., Dressing, C. D., Christiansen, J. L., Fulton, B. J., Lépine, S., Weiss, L., Hirsch, L., Livingston, J., Baranec, C., Law, N. M., Riddle, R., Ziegler, C., Howell, S. B., Horch, E., Everett, M., Teske, J., Martinez, A. O., Obermeier, C., Benneke, B., Scott, N., Deacon, N., Aller, K. M., Hansen, B. M. S., Mancini, L., Ciceri, S., Brahm, R., Jordán, A., Knutson, H. A., Henning, T., Bonnefoy, M., Liu, M. C., Crepp, J. R., Lothringer, J., Hinz, P., Bailey, V., Skemer, A., and Defrere, D. (2016). 197 Candidates and 104 Validated Planets in K2's First Five Fields. *ApJS*, 226:7.

Crossfield, I. J. M., Petigura, E., Schlieder, J. E., Howard, A. W., Fulton, B. J., Aller, K. M., Ciardi, D. R., Lépine, S., Barclay, T., de Pater, I., de Kleer, K., Quintana, E. V., Christiansen, J. L., Schlafly, E., Kaltenegger, L., Crepp, J. R., Henning, T., Obermeier, C., Deacon, N., Weiss, L. M., Isaacson, H. T., Hansen, B. M. S., Liu, M. C., Greene, T., Howell, S. B., Barman, T., and Mordasini, C. (2015). A Nearby M Star with Three Transiting Super-Earths Discovered by K2. *ApJ*, 804:10.

Cutri, R. M., Skrutskie, M. F., van Dyk, S., Beichman, C. A., Carpenter, J. M., Chester, T., Cambresy, L., Evans, T., Fowler, J., Gizis, J., Howard, E., Huchra, J., Jarrett, T., Kopan, E. L., Kirkpatrick, J. D., Light, R. M., Marsh, K. A., McCallon, H., Schneider, S., Stiening, R., Sykes, M., Weinberg, M., Wheaton, W. A., Wheelock, S.,

and Zacarias, N. (2003). *VizieR Online Data Catalog: 2MASS All-Sky Catalog of Point Sources (Cutri+ 2003)*, volume 2246.

Dai, F., Masuda, K., Winn, J. N., and Zeng, L. (2019). Homogeneous Analysis of Hot Earths: Masses, Sizes, and Compositions. *ApJ*, 883(1):79.

Dai, F., Winn, J. N., Albrecht, S., Arriagada, P., Bieryla, A., Butler, R. P., Crane, J. D., Hirano, T., Johnson, J. A., Kiilerich, A., Latham, D. W., Narita, N., Nowak, G., Palle, E., Ribas, I., Rogers, L. A., Sanchis-Ojeda, R., Shectman, S. A., Teske, J. K., Thompson, I. B., Van Eylen, V., Vanderburg, A., Wittenmyer, R. A., and Yu, L. (2016). Doppler Monitoring of Five K2 Transiting Planetary Systems. *ApJ*, 823:115.

Dai, F., Winn, J. N., Gandolfi, D., Wang, S. X., Teske, J. K., Burt, J., Albrecht, S., Barragán, O., Cochran, W. D., Endl, M., Fridlund, M., Hatzes, A. P., Hirano, T., Hirsch, L. A., Johnson, M. C., Bo Justesen, A., Livingston, J., Persson, C. M., Prieto-Arranz, J., Vanderburg, A., Alonso, R., Antoniciello, G., Arriagada, P., Butler, R. P., Cabrera, J., Crane, J. D., Cusano, F., Csizmadia, S., Deeg, H., Dieterich, S. B., Eigmüller, P., Erikson, A., Everett, M. E., Fukui, A., Grziwa, S., Guenther, E. W., Henry, G. W., Howell, S. B., Johnson, J. A., Korth, J., Kuzuhara, M., Narita, N., Nespral, D., Nowak, G., Palle, E., Pätzold, M., Rauer, H., Rodríguez, P. M., Shectman, S. A., Smith, A. M. S., Thompson, I. B., Eylen, V. V., Williamson, M. W., and Wittenmyer, R. A. (2017). The Discovery and Mass Measurement of a New Ultra-short-period Planet: K2-131b. *AJ*, 154(6):226.

Damasso, M., Bonomo, A. S., Astudillo-Defru, N., Bonfils, X., Malavolta, L., Sozzetti, A., Lopez, E., Zeng, L., Haywood, R. D., Irwin, J. M., Mortier, A., Vanderburg, A., Maldonado, J., Lanza, A. F., Affer, L., Almenara, J. M., Benatti, S., Biazzo, K., Bignamini, A., Borsa, F., Bouchy, F., Buchhave, L. A., Cameron, A. C., Carleo, I., Charbonneau, D., Claudi, R., Cosentino, R., Covino, E., Delfosse, X., Desidera, S., Di Fabrizio, L., Dressing, C., Esposito, M., Fares, R., Figueira, P., Fiorenzano, A. F. M., Forveille, T., Giacobbe, P., González-Álvarez, E., Gratton, R., Harutyunyan, A., Johnson, J. A., Latham, D. W., Leto, G., Lopez-Morales, M., Lovis, C., Maggio, A., Mancini, L., Masiero, S., Mayor, M., Micela, G., Molinari, E., Motalebi, F., Murgas, F., Nascimbeni, V., Pagano, I., Pepe, F., Phillips, D. F., Piotto, G., Poretti, E., Rainer, M., Rice, K., Santos, N. C., Sasselov, D., Scandariato, G., Ségransan, D., Smareglia, R., Udry, S., Watson, C., and Wünsche, A. (2018). Eyes on K2-3: A system of three likely sub-Neptunes characterized with HARPS-N and HARPS. *A&A*, 615:A69.

Damasso, M. and Del Sordo, F. (2017). Proxima Centauri reloaded: Unravelling the stellar noise in radial velocities. *A&A*, 599:A126.

Damasso, M., Zeng, L., Malavolta, L., Mayo, A., Sozzetti, A., Mortier, A., Buchhave, L. A., Vand erburg, A., Lopez-Morales, M., Bonomo, A. S., Cameron, A. C., Coffinet, A., Figueira, P., Latham, D. W., Mayor, M., Molinari, E., Pepe, F., Phillips, D. F., Poretti, E., Rice, K., Udry, S., and Watson, C. A. (2019). So close, so different: characterization of the K2-36 planetary system with HARPS-N. *A&A*, 624:A38.

de Wit, J. and Seager, S. (2013). Constraining Exoplanet Mass from Transmission

Spectroscopy. *Science*, 342:1473–1477.

Deming, D., Harrington, J., Laughlin, G., Seager, S., Navarro, S. B., Bowman, W. C., and Horning, K. (2007). Spitzer Transit and Secondary Eclipse Photometry of GJ 436b. *ApJ*, 667:L199–L202.

Demory, B.-O., Torres, G., Neves, V., Rogers, L., Gillon, M., Horch, E., Sullivan, P., Bonfils, X., Delfosse, X., Forveille, T., Lovis, C., Mayor, M., Santos, N., Seager, S., Smalley, B., and Udry, S. (2013). Spitzer Observations of GJ 3470 b: A Very Low-density Neptune-size Planet Orbiting a Metal-rich M Dwarf. *ApJ*, 768:154.

Díaz, R. F., Delfosse, X., Hobson, M. J., Boisse, I., Astudillo-Defru, N., Bonfils, X., Henry, G. W., Arnold, L., Bouchy, F., Bourrier, V., Brugger, B., Dalal, S., Deleuil, M., Demangeon, O., Dolon, F., Dumusque, X., Forveille, T., Hara, N., Hébrard, G., Kiefer, F., Lopez, T., Mignon, L., Moreau, F., Mousis, O., Moutou, C., Pepe, F., Perruchot, S., Richaud, Y., Santerne, A., Santos, N. C., Sottile, R., Stalport, M., Ségransan, D., Udry, S., Unger, N., and Wilson, P. A. (2019). The SOPHIE search for northern extrasolar planets. XIV. A temperate (T_{eq} 300 K) super-earth around the nearby star Gliese 411. *A&A*, 625:A17.

Donahue, R. A., Dobson, A. K., and Baliunas, S. L. (1997). Stellar active region evolution – i. estimated lifetimes of chromospheric active regions and active region complexes. *Solar Physics*, 171(1):191–209.

Donati, J. F., Yu, L., Moutou, C., Cameron, A. C., Malo, L., Grankin, K., Hébrard, E.,

Hussain, G. A. J., Vidotto, A. A., Alencar, S. H. P., Haywood, R. D., Bouvier, J., Petit, P., Takami, M., Herczeg, G. J., Gregory, S. G., Jardine, M. M., Morin, J., and MaTYSSE Collaboration (2017). The hot Jupiter of the magnetically active weak-line T Tauri star V830 Tau. *MNRAS*, 465(3):3343–3360.

Dragomir, D., Benneke, B., Pearson, K. A., Crossfield, I. J. M., Eastman, J., Barman, T., and Biddle, L. I. (2015). Rayleigh Scattering in the Atmosphere of the Warm Exo-Neptune GJ 3470b. *ApJ*, 814:102.

Dragomir, D., Matthews, J. M., Eastman, J. D., Cameron, C., Howard, A. W., Guenther, D. B., Kuschnig, R., Moffat, A. F. J., Rowe, J. F., Rucinski, S. M., Sasselov, D., and Weiss, W. W. (2013). MOST Detects Transits of HD 97658b, a Warm, Likely Volatile-rich Super-Earth. *ApJ*, 772:L2.

Dressing, C. D. and Charbonneau, D. (2013). The Occurrence Rate of Small Planets around Small Stars. *ApJ*, 767:95.

Dressing, C. D. and Charbonneau, D. (2015). The Occurrence of Potentially Habitable Planets Orbiting M Dwarfs Estimated from the Full Kepler Dataset and an Empirical Measurement of the Detection Sensitivity. *ApJ*, 807:45.

Dressing, C. D., Vanderburg, A., Schlieder, J. E., Crossfield, I. J. M., Knutson, H. A., Newton, E. R., Ciardi, D. R., Fulton, B. J., Gonzales, E. J., Howard, A. W., Isaacson, H., Livingston, J., Petigura, E. A., Sinukoff, E., Everett, M., Horch, E., and Howell,

S. B. (2017). Characterizing K2 Candidate Planetary Systems Orbiting Low-mass Stars. II. Planetary Systems Observed During Campaigns 1-7. *AJ*, 154:207.

Dumusque, X., Turner, O., Dorn, C., Eastman, J. D., Allart, R., Adibekyan, V., Sousa, S., Santos, N. C., Mordasini, C., Bourrier, V., Bouchy, F., Coffinet, A., Davies, M. D., Díaz, R. F., Fausnaugh, M. M., Glidden, A., Guerrero, N., Henze, C. E., Jenkins, J. M., Latham, D. W., Lovis, C., Mayor, M., Pepe, F., Quintana, E. V., Ricker, G. R., Rowden, P., Segransan, D., Mascareño, A. S., Seager, S., Twicken, J. D., Udry, S., Vand erspek, R. K., and Winn, J. N. (2019). Hot, rocky and warm, puffy super-Earths orbiting TOI-402 (HD 15337). *A&A*, 627:A43.

Dumusque, X., Udry, S., Lovis, C., Santos, N. C., and Monteiro, M. J. P. F. G. (2011). Planetary detection limits taking into account stellar noise. I. Observational strategies to reduce stellar oscillation and granulation effects. *A&A*, 525:A140.

Eaton, J. A., Henry, G. W., and Fekel, F. C. (2003). Advantages of Automated Observing with Small Telescopes. In Oswalt, T. D., editor, *Astrophysics and Space Science Library*, volume 288 of *Astrophysics and Space Science Library*, page 189.

Faria, J. P., Haywood, R. D., Brewer, B. J., Figueira, P., Oshagh, M., Santerne, A., and Santos, N. C. (2016). Uncovering the planets and stellar activity of CoRoT-7 using only radial velocities. *A&A*, 588:A31.

Figueira, P., Pont, F., Mordasini, C., Alibert, Y., Georgy, C., and Benz, W. (2009). Bulk composition of the transiting hot Neptune around GJ 436. *A&A*, 493(2):671–676.

Foreman-Mackey, D., Hogg, D. W., Lang, D., and Goodman, J. (2013). emcee: The MCMC Hammer. *PASP*, 125:306.

Fortney, J. J., Marley, M. S., and Barnes, J. W. (2007). Planetary Radii across Five Orders of Magnitude in Mass and Stellar Insolation: Application to Transits. *ApJ*, 659:1661–1672.

Frandsen, S. and Lindberg, B. (1999). FIES: A high resolution FIber fed Echelle Spectrograph for the NOT (poster). In Karttunen, H. and Piirola, V., editors, *Astrophysics with the NOT*, page 71.

Fressin, F., Torres, G., Charbonneau, D., Bryson, S. T., Christiansen, J., Dressing, C. D., Jenkins, J. M., Walkowicz, L. M., and Batalha, N. M. (2013). The False Positive Rate of Kepler and the Occurrence of Planets. *ApJ*, 766:81.

Fukui, A., Livingston, J., Narita, N., Hirano, T., Onitsuka, M., Ryu, T., and Kusakabe, N. (2016). Ground-based Transit Observation of the Habitable-zone Super-Earth K2-3d. *AJ*, 152:171.

Fukui, A., Narita, N., Kurosaki, K., Ikoma, M., Yanagisawa, K., Kuroda, D., Shimizu, Y., Takahashi, Y. H., Ohnuki, H., Onitsuka, M., Hirano, T., Suenaga, T., Kawauchi, K., Nagayama, S., Ohta, K., Yoshida, M., Kawai, N., and Izumiura, H. (2013). Optical-to-near-infrared Simultaneous Observations for the Hot Uranus GJ3470b: A Hint of a Cloud-free Atmosphere. *ApJ*, 770:95.

Fulton, B. J. and Petigura, E. A. (2018). The California-Kepler Survey. VII. Precise

Planet Radii Leveraging Gaia DR2 Reveal the Stellar Mass Dependence of the Planet Radius Gap. *AJ*, 156(6):264.

Fulton, B. J., Petigura, E. A., Blunt, S., and Sinukoff, E. (2018). RadVel: The Radial Velocity Modeling Toolkit. *PASP*, 130(4):044504.

Fulton, B. J., Petigura, E. A., Howard, A. W., Isaacson, H., Marcy, G. W., Cargile, P. A., Hebb, L., Weiss, L. M., Johnson, J. A., Morton, T. D., Sinukoff, E., Crossfield, I. J. M., and Hirsch, L. A. (2017). The California-Kepler Survey. III. A Gap in the Radius Distribution of Small Planets. *AJ*, 154:109.

Fulton, B. J., Weiss, L. M., Sinukoff, E., Isaacson, H., Howard, A. W., Marcy, G. W., Henry, G. W., Holden, B. P., and Kibrick, R. I. (2015). Three Super-Earths Orbiting HD 7924. *ApJ*, 805(2):175.

Gaia Collaboration, Brown, A. G. A., Vallenari, A., Prusti, T., de Bruijne, J. H. J., Babusiaux, C., Bailer-Jones, C. A. L., Biermann, M., Evans, D. W., Eyer, L., Jansen, F., Jordi, C., Klioner, S. A., Lammers, U., Lindegren, L., Luri, X., Mignard, F., Panem, C., Pourbaix, D., Randich, S., Sartoretti, P., Siddiqui, H. I., Soubiran, C., van Leeuwen, F., Walton, N. A., Arenou, F., Bastian, U., Cropper, M., Drimmel, R., Katz, D., Lattanzi, M. G., Bakker, J., Cacciari, C., Castañeda, J., Chaoul, L., Cheek, N., De Angeli, F., Fabricius, C., Guerra, R., Holl, B., Masana, E., Messineo, R., Mowlavi, N., Nienartowicz, K., Panuzzo, P., Portell, J., Riello, M., Seabroke, G. M., Tanga, P., Thévenin, F., Gracia-Abril, G., Comoretto, G., Garcia-Reinaldos, M., Teyssier, D., Altmann, M., Andrae, R., Audard, M., Bellas-Velidis, I., Benson, K.,

Berthier, J., Blomme, R., Burgess, P., Busso, G., Carry, B., Cellino, A., Clementini, G., Clotet, M., Creevey, O., Davidson, M., De Ridder, J., Delchambre, L., Dell'Oro, A., Ducourant, C., Fernández-Hernández, J., Fouesneau, M., Frémat, Y., Galluccio, L., García-Torres, M., González-Núñez, J., González-Vidal, J. J., Gosset, E., Guy, L. P., Halbwachs, J. L., Hambly, N. C., Harrison, D. L., Hernández, J., Hestroffer, D., Hodgkin, S. T., Hutton, A., Jasniewicz, G., Jean-Antoine-Piccolo, A., Jordan, S., Korn, A. J., Krone-Martins, A., Lanzafame, A. C., Lebzelter, T., Löffler, W., Manteiga, M., Marrese, P. M., Martín-Fleitas, J. M., Moitinho, A., Mora, A., Muinonen, K., Osinde, J., Pancino, E., Pauwels, T., Petit, J. M., Recio-Blanco, A., Richards, P. J., Rimoldini, L., Robin, A. C., Sarro, L. M., Siopis, C., Smith, M., Sozzetti, A., Süveges, M., Torra, J., van Reeven, W., Abbas, U., Abreu Aramburu, A., Accart, S., Aerts, C., Altavilla, G., Álvarez, M. A., Alvarez, R., Alves, J., Anderson, R. I., Andrei, A. H., Anglada Varela, E., Antiche, E., Antoja, T., Arcay, B., Astraatmadja, T. L., Bach, N., Baker, S. G., Balaguer-Núñez, L., Balm, P., Barache, C., Barata, C., Barbato, D., Barblan, F., Barklem, P. S., Barrado, D., Barros, M., Barstow, M. A., Bartholomé Muñoz, S., Bassilana, J. L., Becciani, U., Bellazzini, M., Berihuete, A., Bertone, S., Bianchi, L., Bienaymé, O., Blanco-Cuaresma, S., Boch, T., Boeche, C., Bombrun, A., Borrachero, R., Bossini, D., Bouquillon, S., Bourda, G., Bragaglia, A., Bramante, L., Breddels, M. A., Bressan, A., Brouillet, N., Brüsemeister, T., Brugaletta, E., Bucciarelli, B., Burlacu, A., Busonero, D., Butkevich, A. G., Buzzi, R., Caffau, E., Cancelliere, R., Cannizzaro, G., Cantat-Gaudin, T., Carballo, R., Carlucci, T., Carrasco, J. M., Casamiquela, L., Castellani, M., Castro-Ginard, A., Charlot, P.,

Chemin, L., Chiavassa, A., Cocozza, G., Costigan, G., Cowell, S., Crifo, F., Crosta, M., Crowley, C., Cuypers, J., Dafonte, C., Damerdji, Y., Dapergolas, A., David, P., David, M., de Laverny, P., De Luise, F., De March, R., de Martino, D., de Souza, R., de Torres, A., Debosscher, J., del Pozo, E., Delbo, M., Delgado, A., Delgado, H. E., Di Matteo, P., Diakite, S., Diener, C., Distefano, E., Dolding, C., Drazinos, P., Durán, J., Edvardsson, B., Enke, H., Eriksson, K., Esquej, P., Eynard Bontemps, G., Fabre, C., Fabrizio, M., Faigler, S., Falcão, A. J., Farràs Casas, M., Federici, L., Fedorets, G., Fernique, P., Figueras, F., Filippi, F., Findeisen, K., Fonti, A., Fraile, E., Fraser, M., Frézouls, B., Gai, M., Galleti, S., Garabato, D., García-Sedano, F., Garofalo, A., Garralda, N., Gavel, A., Gavras, P., Gerssen, J., Geyer, R., Giacobbe, P., Gilmore, G., Girona, S., Giuffrida, G., Glass, F., Gomes, M., Granvik, M., Gueguen, A., Guerrier, A., Guiraud, J., Gutiérrez-Sánchez, R., Haigron, R., Hatzidimitriou, D., Hauser, M., Haywood, M., Heiter, U., Helmi, A., Heu, J., Hilger, T., Hobbs, D., Hofmann, W., Holland, G., Huckle, H. E., Hypki, A., Icardi, V., Janßen, K., Jevardat de Fombelle, G., Jonker, P. G., Juhász, Á. L., Julbe, F., Karampelas, A., Kewley, A., Klar, J., Kochoska, A., Kohley, R., Kolenberg, K., Kontizas, M., Kontizas, E., Koposov, S. E., Kordopatis, G., Kostrzewa-Rutkowska, Z., Koubsky, P., Lambert, S., Lanza, A. F., Lasne, Y., Lavigne, J. B., Le Fustec, Y., Le Poncin-Lafitte, C., Lebreton, Y., Leccia, S., Leclerc, N., Lecoeur-Taibi, I., Lenhardt, H., Leroux, F., Liao, S., Licata, E., Lindstrøm, H. E. P., Lister, T. A., Livanou, E., Lobel, A., López, M., Managau, S., Mann, R. G., Mantelet, G., Marchal, O., Marchant, J. M., Marconi, M., Marinoni, S., Marschalkó, G., Marshall, D. J., Martino, M., Marton, G., Mary, N., Massari,

D., Matijevič, G., Mazeh, T., McMillan, P. J., Messina, S., Michalik, D., Millar, N. R., Molina, D., Molinaro, R., Molnár, L., Montegriffo, P., Mor, R., Morbidelli, R., Morel, T., Morris, D., Mulone, A. F., Muraveva, T., Musella, I., Nelemans, G., Nicastro, L., Noval, L., O'Mullane, W., Ordénovic, C., Ordóñez-Blanco, D., Osborne, P., Pagani, C., Pagano, I., Pailler, F., Palacin, H., Palaversa, L., Panahi, A., Pawlak, M., Piersimoni, A. M., Pineau, F. X., Plachy, E., Plum, G., Poggio, E., Poujoulet, E., Prša, A., Pulone, L., Racero, E., Ragaini, S., Rambaux, N., Ramos-Lerate, M., Regibo, S., Reylé, C., Riclet, F., Ripepi, V., Riva, A., Rivard, A., Rixon, G., Roegiers, T., Roelens, M., Romero-Gómez, M., Rowell, N., Royer, F., Ruiz-Dern, L., Sadowski, G., Sagristà Sellés, T., Sahlmann, J., Salgado, J., Salguero, E., Sanna, N., Santana-Ros, T., Sarasso, M., Savietto, H., Schultheis, M., Sciacca, E., Segol, M., Segovia, J. C., Ségransan, D., Shih, I. C., Siltala, L., Silva, A. F., Smart, R. L., Smith, K. W., Solano, E., Solitro, F., Sordo, R., Soria Nieto, S., Souchay, J., Spagna, A., Spoto, F., Stampa, U., Steele, I. A., Steidelmüller, H., Stephenson, C. A., Stoev, H., Suess, F. F., Surdej, J., Szabados, L., Szegedi-Elek, E., Tapiador, D., Taris, F., Tauran, G., Taylor, M. B., Teixeira, R., Terrett, D., Teyssand ier, P., Thuillot, W., Titarenko, A., Torra Clotet, F., Turon, C., Ulla, A., Utrilla, E., Uzzi, S., Vaillant, M., Valentini, G., Valette, V., van Elteren, A., Van Hemelryck, E., van Leeuwen, M., Vaschetto, M., Vecchiato, A., Veljanoski, J., Viala, Y., Vicente, D., Vogt, S., von Essen, C., Voss, H., Votruba, V., Voutsinas, S., Walmsley, G., Weiler, M., Wertz, O., Wevers, T., Wyrzykowski, Ł., Yoldas, A., Žerjal, M., Ziaeepour, H., Zorec, J., Zschocke, S., Zucker, S., Zurbach, C., and Zwitter, T. (2018). Gaia Data Release 2. Summary of the contents and survey

properties. *A&A*, 616:A1.

Gaia Collaboration, Prusti, T., de Bruijne, J. H. J., Brown, A. G. A., Vallenari, A., Babusiaux, C., Bailer-Jones, C. A. L., Bastian, U., Biermann, M., Evans, D. W., Eyer, L., Jansen, F., Jordi, C., Klioner, S. A., Lammers, U., Lindegren, L., Luri, X., Mignard, F., Milligan, D. J., Panem, C., Poinsignon, V., Pourbaix, D., Randich, S., Sarri, G., Sartoretti, P., Siddiqui, H. I., Soubiran, C., Valette, V., van Leeuwen, F., Walton, N. A., Aerts, C., Arenou, F., Cropper, M., Drimmel, R., Høg, E., Katz, D., Lattanzi, M. G., O'Mullane, W., Grebel, E. K., Holland, A. D., Huc, C., Passot, X., Bramante, L., Cacciari, C., Castañeda, J., Chaoul, L., Cheek, N., De Angeli, F., Fabricius, C., Guerra, R., Hernández, J., Jean-Antoine-Piccolo, A., Masana, E., Messineo, R., Mowlavi, N., Nienartowicz, K., Ordóñez-Blanco, D., Panuzzo, P., Portell, J., Richards, P. J., Riello, M., Seabroke, G. M., Tanga, P., Thévenin, F., Torra, J., Els, S. G., Gracia-Abril, G., Comoretto, G., Garcia-Reinaldos, M., Lock, T., Mercier, E., Altmann, M., Andrae, R., Astraatmadja, T. L., Bellas-Velidis, I., Benson, K., Berthier, J., Blomme, R., Busso, G., Carry, B., Cellino, A., Clementini, G., Cowell, S., Creevey, O., Cuypers, J., Davidson, M., De Ridder, J., de Torres, A., Delchambre, L., Dell'Oro, A., Ducourant, C., Frémat, Y., García-Torres, M., Gosset, E., Halbwachs, J. L., Hambly, N. C., Harrison, D. L., Hauser, M., Hestroffer, D., Hodgkin, S. T., Huckle, H. E., Hutton, A., Jasniewicz, G., Jordan, S., Kontizas, M., Korn, A. J., Lanzafame, A. C., Manteiga, M., Moitinho, A., Muinonen, K., Osinde, J., Pancino, E., Pauwels, T., Petit, J. M., Recio-Blanco, A., Robin, A. C., Sarro, L. M., Siopis,

C., Smith, M., Smith, K. W., Sozzetti, A., Thuillot, W., van Reeven, W., Viala, Y., Abbas, U., Abreu Aramburu, A., Accart, S., Aguado, J. J., Allan, P. M., Allasia, W., Altavilla, G., Álvarez, M. A., Alves, J., Anderson, R. I., Andrei, A. H., Anglada Varela, E., Antiche, E., Antoja, T., Antón, S., Arcay, B., Atzei, A., Ayache, L., Bach, N., Baker, S. G., Balaguer-Núñez, L., Barache, C., Barata, C., Barbier, A., Barblan, F., Baroni, M., Barrado y Navascués, D., Barros, M., Barstow, M. A., Becciani, U., Bellazzini, M., Bellei, G., Bello García, A., Belokurov, V., Bendjoya, P., Berihuete, A., Bianchi, L., Bienaymé, O., Billebaud, F., Blagorodnova, N., Blanco-Cuaresma, S., Boch, T., Bombrun, A., Borrachero, R., Bouquillon, S., Bourda, G., Bouy, H., Bragaglia, A., Breddels, M. A., Brouillet, N., Brüsemeister, T., Bucciarelli, B., Budnik, F., Burgess, P., Burgon, R., Burlacu, A., Busonero, D., Buzzi, R., Caffau, E., Cambras, J., Campbell, H., Cancelliere, R., Cantat-Gaudin, T., Carlucci, T., Carrasco, J. M., Castellani, M., Charlot, P., Charnas, J., Charvet, P., Chassat, F., Chiavassa, A., Clotet, M., Cocozza, G., Collins, R. S., Collins, P., Costigan, G., Crifo, F., Cross, N. J. G., Crosta, M., Crowley, C., Dafonte, C., Damerdji, Y., Dapergolas, A., David, P., David, M., De Cat, P., de Felice, F., de Laverny, P., De Luise, F., De March, R., de Martino, D., de Souza, R., Debosscher, J., del Pozo, E., Delbo, M., Delgado, A., Delgado, H. E., di Marco, F., Di Matteo, P., Diakite, S., Distefano, E., Dolding, C., Dos Anjos, S., Drazinos, P., Durán, J., Dzigan, Y., Ecale, E., Edvardsson, B., Enke, H., Erdmann, M., Escolar, D., Espina, M., Evans, N. W., Eynard Bontemps, G., Fabre, C., Fabrizio, M., Faigler, S., Falcão, A. J., Farràs Casas, M., Faye, F., Federici, L., Fedorets, G., Fernández-Hernández, J., Fernique, P., Fienga, A., Figueras, F., Filippi, F., Findeisen,

K., Fonti, A., Fouesneau, M., Fraile, E., Fraser, M., Fuchs, J., Furnell, R., Gai, M., Galleti, S., Galluccio, L., Garabato, D., García-Sedano, F., Garé, P., Garofalo, A., Garralda, N., Gavras, P., Gerssen, J., Geyer, R., Gilmore, G., Girona, S., Giuffrida, G., Gomes, M., González-Marcos, A., González-Núñez, J., González-Vidal, J. J., Granvik, M., Guerrier, A., Guillout, P., Guiraud, J., Gúrpide, A., Gutiérrez-Sánchez, R., Guy, L. P., Haigron, R., Hatzidimitriou, D., Haywood, M., Heiter, U., Helmi, A., Hobbs, D., Hofmann, W., Holl, B., Holland , G., Hunt, J. A. S., Hypki, A., Icardi, V., Irwin, M., Jevardat de Fombelle, G., Jofré, P., Jonker, P. G., Jorissen, A., Julbe, F., Karampelas, A., Kochoska, A., Kohley, R., Kolenberg, K., Kontizas, E., Koposov, S. E., Kordopatis, G., Koubsky, P., Kowalczyk, A., Krone-Martins, A., Kudryashova, M., Kull, I., Bachchan, R. K., Lacoste-Seris, F., Lanza, A. F., Lavigne, J. B., Le Poncin-Lafitte, C., Lebreton, Y., Lebzelter, T., Leccia, S., Leclerc, N., Lecoeur-Taibi, I., Lemaitre, V., Lenhardt, H., Leroux, F., Liao, S., Licata, E., Lindstrøm, H. E. P., Lister, T. A., Livanou, E., Lobel, A., Löffler, W., López, M., Lopez-Lozano, A., Lorenz, D., Loureiro, T., MacDonald, I., Magalhães Fernandes, T., Managau, S., Mann, R. G., Mantelet, G., Marchal, O., Marchant, J. M., Marconi, M., Marie, J., Marinoni, S., Marrese, P. M., Marschalkó, G., Marshall, D. J., Martín-Fleitas, J. M., Martino, M., Mary, N., Matijevič, G., Mazeh, T., McMillan, P. J., Messina, S., Mestre, A., Michalik, D., Millar, N. R., Miranda, B. M. H., Molina, D., Molinaro, R., Molinaro, M., Molnár, L., Moniez, M., Montegriffo, P., Monteiro, D., Mor, R., Mora, A., Morbidelli, R., Morel, T., Morgenthaler, S., Morley, T., Morris, D., Mulone, A. F., Muraveva, T., Musella, I., Narbonne, J., Nelemans, G., Nicastro, L., Noval, L., Ordénovic, C., Ordieres-Meré,

J., Osborne, P., Pagani, C., Pagano, I., Pailler, F., Palacin, H., Palaversa, L., Parsons, P., Paulsen, T., Pecoraro, M., Pedrosa, R., Pentikäinen, H., Pereira, J., Pichon, B., Piersimoni, A. M., Pineau, F. X., Plachy, E., Plum, G., Poujoulet, E., Prša, A., Pulone, L., Ragaini, S., Rago, S., Rambaux, N., Ramos-Lerate, M., Ranalli, P., Rauw, G., Read, A., Regibo, S., Renk, F., Reylé, C., Ribeiro, R. A., Rimoldini, L., Ripepi, V., Riva, A., Rixon, G., Roelens, M., Romero-Gómez, M., Rowell, N., Royer, F., Rudolph, A., Ruiz-Dern, L., Sadowski, G., Sagristà Sellés, T., Sahlmann, J., Salgado, J., Salguero, E., Sarasso, M., Savietto, H., Schnorhk, A., Schultheis, M., Sciacca, E., Segol, M., Segovia, J. C., Segransan, D., Serpell, E., Shih, I. C., Smareglia, R., Smart, R. L., Smith, C., Solano, E., Solitro, F., Sordo, R., Soria Nieto, S., Souchay, J., Spagna, A., Spoto, F., Stampa, U., Steele, I. A., Steidelmüller, H., Stephenson, C. A., Stoev, H., Suess, F. F., Süveges, M., Surdej, J., Szabados, L., Szegedi-Elek, E., Tapiador, D., Taris, F., Tauran, G., Taylor, M. B., Teixeira, R., Terrett, D., Tingley, B., Trager, S. C., Turon, C., Ulla, A., Utrilla, E., Valentini, G., van Elteren, A., Van Hemelryck, E., van Leeuwen, M., Varadi, M., Vecchiato, A., Veljanoski, J., Via, T., Vicente, D., Vogt, S., Voss, H., Votruba, V., Voutsinas, S., Walmsley, G., Weiler, M., Weingrill, K., Werner, D., Wevers, T., Whitehead, G., Wyrzykowski, Ł., Yoldas, A., Žerjal, M., Zucker, S., Zurbach, C., Zwitter, T., Alecu, A., Allen, M., Allende Prieto, C., Amorim, A., Anglada-Escudé, G., Arsenijevic, V., Azaz, S., Balm, P., Beck, M., Bernstein, H. H., Bigot, L., Bijaoui, A., Blasco, C., Bonfigli, M., Bono, G., Boudreault, S., Bressan, A., Brown, S., Brunet, P. M., Bunclark, P., Buonanno, R., Butkevich, A. G., Carret, C., Carrion, C., Chemin, L., Chéreau, F., Corcione, L., Darmigny,

E., de Boer, K. S., de Teodoro, P., de Zeeuw, P. T., Delle Luche, C., Domingues, C. D., Dubath, P., Fodor, F., Frézouls, B., Fries, A., Fustes, D., Fyfe, D., Gallardo, E., Gallegos, J., Gardiol, D., Gebran, M., Gomboc, A., Gómez, A., Grux, E., Gueguen, A., Heyrovsky, A., Hoar, J., Iannicola, G., Isasi Parache, Y., Janotto, A. M., Joliet, E., Jonckheere, A., Keil, R., Kim, D. W., Klagyivik, P., Klar, J., Knude, J., Kochukhov, O., Kolka, I., Kos, J., Kutka, A., Lainey, V., LeBouquin, D., Liu, C., Loreggia, D., Makarov, V. V., Marseille, M. G., Martayan, C., Martinez-Rubi, O., Massart, B., Meynadier, F., Mignot, S., Munari, U., Nguyen, A. T., Nordlander, T., Ocvirk, P., O'Flaherty, K. S., Olias Sanz, A., Ortiz, P., Osorio, J., Oszkiewicz, D., Ouzounis, A., Palmer, M., Park, P., Pasquato, E., Peltzer, C., Peralta, J., Péturaud, F., Pieniluoma, T., Pigozzi, E., Poels, J., Prat, G., Prod'homme, T., Raison, F., Rebordao, J. M., Risquez, D., Rocca-Volmerange, B., Rosen, S., Ruiz-Fuertes, M. I., Russo, F., Sembay, S., Serraller Vizcaino, I., Short, A., Siebert, A., Silva, H., Sinachopoulos, D., Slezak, E., Soffel, M., Sosnowska, D., Straižys, V., ter Linden, M., Terrell, D., Theil, S., Tiede, C., Troisi, L., Tsalmantza, P., Tur, D., Vaccari, M., Vachier, F., Valles, P., Van Hamme, W., Veltz, L., Virtanen, J., Wallut, J. M., Wichmann, R., Wilkinson, M. I., Ziaeepour, H., and Zschocke, S. (2016). The Gaia mission. *A&A*, 595:A1.

Ginzburg, S., Schlichting, H. E., and Sari, R. (2018). Core-powered mass-loss and the radius distribution of small exoplanets. *MNRAS*, 476(1):759–765.

Gnevyshev, M. N. (1938). On the nature of solar activity. *Izvestiya Glavnoj Astronomicheskoj Observatorii v Pulkove*, 16:36–45.

Gomes da Silva, J., Santos, N. C., Bonfils, X., Delfosse, X., Forveille, T., Udry, S., Dumusque, X., and Lovis, C. (2012). Long-term magnetic activity of a sample of M-dwarf stars from the HARPS program . II. Activity and radial velocity. *A&A*, 541:A9.

Green, G. M., Schlafly, E. F., Finkbeiner, D., Rix, H.-W., Martin, N., Burgett, W., Draper, P. W., Flewelling, H., Hodapp, K., Kaiser, N., Kudritzki, R.-P., Magnier, E. A., Metcalfe, N., Tonry, J. L., Wainscoat, R., and Waters, C. (2018). Galactic reddening in 3D from stellar photometry - an improved map. *MNRAS*, 478:651–666.

Greene, T. P., Line, M. R., Montero, C., Fortney, J. J., Lustig-Yaeger, J., and Luther, K. (2016). Characterizing Transiting Exoplanet Atmospheres with JWST. *ApJ*, 817:17.

Grunblatt, S. K., Howard, A. W., and Haywood, R. D. (2015). Determining the Mass of Kepler-78b with Nonparametric Gaussian Process Estimation. *ApJ*, 808:127.

Guerrero, N. M., Seager, S., Huang, C. X., Vanderburg, A., Garcia Soto, A., Mireles, I., Hesse, K., Fong, W., Glidden, A., Shporer, A., Latham, D. W., Collins, K. A., Quinn, S. N., Burt, J., Dragomir, D., Crossfield, I., Vanderspek, R., Fausnaugh, M., Burke, C. J., Ricker, G., Daylan, T., Essack, Z., Günther, M. N., Osborn, H. P., Pepper, J., Rowden, P., Sha, L., Villanueva, Steven, J., Yahalomi, D. A., Yu, L., Ballard, S., Batalha, N. M., Berardo, D., Chontos, A., Dittmann, J. A., Esquerdo, G. A., Mikal-Evans, T., Jayaraman, R., Krishnamurthy, A., Louie, D. R., Mehrle, N., Niraula, P., Rackham, B. V., Rodriguez, J. E., Rowden, S. J. L., Sousa-Silva, C., Watanabe, D., Wong, I., Zhan, Z., Zivanovic, G., Christiansen, J. L., Ciardi, D. R.,

Swain, M. A., Lund, M. B., Mullally, S. E., Fleming, S. W., Rodriguez, D. R., Boyd, P. T., Quintana, E. V., Barclay, T., Colón, K. D., Rinehart, S. A., Schlieder, J. E., Clampin, M., Jenkins, J. M., Twicken, J. D., Caldwell, D. A., Coughlin, J. L., Henze, C., Lissauer, J. J., Morris, R. L., Rose, M. E., Smith, J. C., Tenenbaum, P., Ting, E. B., Wohler, B., Bakos, G. Á., Bean, J. L., Berta-Thompson, Z. K., Bieryla, A., Bouma, L. G., Buchhave, L. A., Butler, N., Charbonneau, D., Doty, J. P., Ge, J., Holman, M. J., Howard, A. W., Kaltenegger, L., Kane, S. R., Kjeldsen, H., Kreidberg, L., Lin, D. N. C., Minsky, C., Narita, N., Paegert, M., Pál, A., Palle, E., Sasselov, D. D., Spencer, A., Sozzetti, A., Stassun, K. G., Torres, G., Udry, S., and Winn, J. N. (2021). The TESS Objects of Interest Catalog from the TESS Prime Mission. *arXiv e-prints*, page arXiv:2103.12538.

Guo, X., Crossfield, I. J. M., Dragomir, D., Kosiarek, M. R., Lothringer, J., Mikal-Evans, T., Rosenthal, L., Benneke, B., Knutson, H. A., Dalba, P. A., Kempton, E. M. R., Henry, G. W., McCullough, P. R., Barman, T., Blunt, S., Chontos, A., Fortney, J., Fulton, B. J., Hirsch, L., Howard, A. W., Isaacson, H., Matthews, J., Mocnik, T., Morley, C., Petigura, E. A., and Weiss, L. M. (2020). Updated Parameters and a New Transmission Spectrum of HD 97658b. *AJ*, 159(5):239.

Gupta, A. and Schlichting, H. E. (2019). Sculpting the valley in the radius distribution of small exoplanets as a by-product of planet formation: the core-powered mass-loss mechanism. *MNRAS*, 487(1):24–33.

Gupta, A. and Schlichting, H. E. (2020). Signatures of the core-powered mass-loss mech-

anism in the exoplanet population: dependence on stellar properties and observational predictions. *MNRAS*, 493(1):792–806.

Halverson, S., Terrien, R., Mahadevan, S., Roy, A., Bender, C., Stefánsson, G. K., Monson, A., Levi, E., Hearty, F., Blake, C., McElwain, M., Schwab, C., Ramsey, L., Wright, J., Wang, S., Gong, Q., and Roberston, P. (2016). A comprehensive radial velocity error budget for next generation Doppler spectrometers. In *Ground-based and Airborne Instrumentation for Astronomy VI*, volume 9908 of *Proc. SPIE*, page 99086P.

Hatzes, A. P., Endl, M., Cochran, W. D., MacQueen, P. J., Han, I., Lee, B. C., Kim, K. M., Mkrtichian, D., Döllinger, M., Hartmann, M., Karjalainen, M., and Dreizler, S. (2018). The Radial Velocity Variability of the K-giant γ Draconis: Stellar Variability Masquerading as a Planet. *AJ*, 155(3):120.

Haywood, R. D. (2015). *Hide and Seek: Radial-Velocity Searches for Planets around Active Stars*. PhD thesis, University of St Andrews.

Haywood, R. D., Collier Cameron, A., Queloz, D., Barros, S. C. C., Deleuil, M., Fares, R., Gillon, M., Lanza, A. F., Lovis, C., Moutou, C., Pepe, F., Pollacco, D., Santerne, A., Ségransan, D., and Unruh, Y. C. (2014). Planets and stellar activity: hide and seek in the CoRoT-7 system. *MNRAS*, 443:2517–2531.

Haywood, R. D., Vanderburg, A., Mortier, A., Giles, H. A. C., López-Morales, M., Lopez, E. D., Malavolta, L., Charbonneau, D., Collier Cameron, A., Coughlin, J. L., Dressing,

C. D., Nava, C., Latham, D. W., Dumusque, X., Lovis, C., Molinari, E., Pepe, F., Sozzetti, A., Udry, S., Bouchy, F., Johnson, J. A., Mayor, M., Micela, G., Phillips, D., Piotto, G., Rice, K., Sasselov, D., Ségransan, D., Watson, C., Affer, L., Bonomo, A. S., Buchhave, L. A., Ciardi, D. R., Fiorenzano, A. F., and Harutyunyan, A. (2018). An Accurate Mass Determination for Kepler-1655b, a Moderately Irradiated World with a Significant Volatile Envelope. *AJ*, 155:203.

Henry, G. W. (1999). Techniques for Automated High-Precision Photometry of Sun-like Stars. *PASP*, 111:845–860.

Henwood, R., Chapman, S. C., and Willis, D. M. (2010). Increasing Lifetime of Recurrent Sunspot Groups Within the Greenwich Photoheliographic Results. *Solar Physics*, 262(2):299–313.

Howard, A. W., Johnson, J. A., Marcy, G. W., Fischer, D. A., Wright, J. T., Bernat, D., Henry, G. W., Peek, K. M. G., Isaacson, H., Apps, K., Endl, M., Cochran, W. D., Valenti, J. A., Anderson, J., and Piskunov, N. E. (2010). The California Planet Survey. I. Four New Giant Exoplanets. *ApJ*, 721:1467–1481.

Howard, A. W., Johnson, J. A., Marcy, G. W., Fischer, D. A., Wright, J. T., Henry, G. W., Isaacson, H., Valenti, J. A., Anderson, J., and Piskunov, N. E. (2011). The NASA-UC Eta-Earth Program. III. A Super-Earth Orbiting HD 97658 and a Neptune-mass Planet Orbiting Gl 785. *ApJ*, 730:10.

Howard, A. W., Marcy, G. W., Bryson, S. T., Jenkins, J. M., Rowe, J. F., Batalha,

N. M., Borucki, W. J., Koch, D. G., Dunham, E. W., Gautier, III, T. N., Van Cleve, J., Cochran, W. D., Latham, D. W., Lissauer, J. J., Torres, G., Brown, T. M., Gilliland, R. L., Buchhave, L. A., Caldwell, D. A., Christensen-Dalsgaard, J., Ciardi, D., Fressin, F., Haas, M. R., Howell, S. B., Kjeldsen, H., Seager, S., Rogers, L., Sasselov, D. D., Steffen, J. H., Basri, G. S., Charbonneau, D., Christiansen, J., Clarke, B., Dupree, A., Fabrycky, D. C., Fischer, D. A., Ford, E. B., Fortney, J. J., Tarter, J., Girouard, F. R., Holman, M. J., Johnson, J. A., Klaus, T. C., Machalek, P., Moorhead, A. V., Morehead, R. C., Ragozzine, D., Tenenbaum, P., Twicken, J. D., Quinn, S. N., Isaacson, H., Shporer, A., Lucas, P. W., Walkowicz, L. M., Welsh, W. F., Boss, A., Devore, E., Gould, A., Smith, J. C., Morris, R. L., Prsa, A., Morton, T. D., Still, M., Thompson, S. E., Mullally, F., Endl, M., and MacQueen, P. J. (2012). Planet Occurrence within 0.25 AU of Solar-type Stars from Kepler. *ApJS*, 201:15.

Huber, D., Bryson, S. T., Haas, M. R., Barclay, T., Barentsen, G., Howell, S. B., Sharma, S., Stello, D., and Thompson, S. E. (2016). The K2 Ecliptic Plane Input Catalog (EPIC) and Stellar Classifications of 138,600 Targets in Campaigns 1-8. *ApJS*, 224:2.

Huber, D., Zinn, J., Bojsen-Hansen, M., Pinsonneault, M., Sahlholdt, C., Serenelli, A., Silva Aguirre, V., Stassun, K., Stello, D., Tayar, J., Bastien, F., Bedding, T. R., Buchhave, L. A., Chaplin, W. J., Davies, G. R., García, R. A., Latham, D. W., Mathur, S., Mosser, B., and Sharma, S. (2017a). Asteroseismology and Gaia: Testing Scaling Relations Using 2200 Kepler Stars with TGAS Parallaxes. *ApJ*, 844:102.

Huber, D., Zinn, J., Bojsen-Hansen, M., Pinsonneault, M., Sahlholdt, C., Serenelli,

A., Silva Aguirre, V., Stassun, K., Stello, D., Tayar, J., Bastien, F., Bedding, T. R., Buchhave, L. A., Chaplin, W. J., Davies, G. R., García, R. A., Latham, D. W., Mathur, S., Mosser, B., and Sharma, S. (2017b). Asteroseismology and Gaia: Testing Scaling Relations Using 2200 Kepler Stars with TGAS Parallaxes. *ApJ*, 844(2):102.

Hurt, S. A., Quinn, S. N., Latham, D. W., Vanderburg, A., Esquerdo, G. A., Calkins, M. L., Berlind, P., Angus, R., Latham, C. A., and Zhou, G. (2021). A Decade of Radial-velocity Monitoring of Vega and New Limits on the Presence of Planets. *AJ*, 161(4):157.

Inamdar, N. K. and Schlichting, H. E. (2015). The formation of super-Earths and mini-Neptunes with giant impacts. *MNRAS*, 448:1751–1760.

Isaacson, H. and Fischer, D. (2010). Chromospheric Activity and Jitter Measurements for 2630 Stars on the California Planet Search. *ApJ*, 725:875–885.

Jeffers, S. V. and Keller, C. U. (2009). An analytical model to demonstrate the reliability of reconstructed 'active longitudes'. In Stempels, E., editor, *15th Cambridge Workshop on Cool Stars, Stellar Systems, and the Sun*, volume 1094 of *American Institute of Physics Conference Series*, pages 664–667.

Jin, S., Mordasini, C., Parmentier, V., van Boekel, R., Henning, T., and Ji, J. (2014). Planetary Population Synthesis Coupled with Atmospheric Escape: A Statistical View of Evaporation. *ApJ*, 795(1):65.

Jones, E., Oliphant, T., Peterson, P., et al. (2001). SciPy: Open source scientific tools for Python.

Kasper, D., Bean, J. L., Oklopčić, A., Malsky, I., Kempton, E. M. R., Désert, J.-M., Rogers, L. A., and Mansfield, M. (2020). Nondetection of Helium in the Upper Atmospheres of Three Sub-Neptune Exoplanets. *AJ*, 160(6):258.

Kempton, E. M.-R., Lupu, R., Owusu-Asare, A., Slough, P., and Cale, B. (2017). Exo-Transmit: An Open-Source Code for Calculating Transmission Spectra for Exoplanet Atmospheres of Varied Composition. *PASP*, 129(4):044402.

Klein, B., Donati, J.-F., Moutou, C., Delfosse, X., Bonfils, X., Martioli, E., Fouqué, P., Cloutier, R., Artigau, É., Doyon, R., Hébrard, G., Morin, J., Rameau, J., Plavchan, P., and Gaidos, E. (2021). Investigating the young AU Mic system with SPIRou: large-scale stellar magnetic field and close-in planet mass. *MNRAS*, 502(1):188–205.

Kosiarek, M. R., Berardo, D. A., Crossfield, I. J. M., Laguna, C., Piaulet, C., Akana Murphy, J. M., Howell, S. B., Henry, G. W., Isaacson, H., Fulton, B., Weiss, L. M., Petigura, E. A., Behmard, A., Hirsch, L. A., Teske, J., Burt, J. A., Mills, S. M., Chontos, A., Močnik, T., Howard, A. W., Werner, M., Livingston, J. H., Krick, J., Beichman, C., Gorjian, V., Kreidberg, L., Morley, C., Christiansen, J. L., Morales, F. Y., Scott, N. J., Crane, J. D., Wang, S. X., Shectman, S. A., Rosenthal, L. J., Grunblatt, S. K., Rubenzahl, R. A., Dalba, P. A., Giacalone, S., Villanueva, C. D., Liu, Q., Dai, F., Hill, M. L., Rice, M., Kane, S. R., and Mayo, A. W. (2021). Physical Parameters of the Multiplanet Systems HD 106315 and GJ 9827. *AJ*, 161(1):47.

Kosiarek, M. R., Blunt, S., López-Morales, M., Crossfield, I. J. M., Sinukoff, E., Petigura, E. A., Gonzales, E. J., Poretti, E., Malavolta, L., Howard, A. W., Isaacson, H., Haywood, R. D., Ciardi, D. R., Bristow, M., Collier Cameron, A., Charbonneau, D., Dressing, C. D., Figueira, P., Fulton, B. J., Hardee, B. J., Hirsch, L. A., Latham, D. W., Mortier, A., Nava, C., Schlieder, J. E., Vanderburg, A., Weiss, L., Bonomo, A. S., Bouchy, F., Buchhave, L. A., Coffinet, A., Damasso, M., Dumusque, X., Lovis, C., Mayor, M., Micela, G., Molinari, E., Pepe, F., Phillips, D., Piotto, G., Rice, K., Sasselov, D., Ségransan, D., Sozzetti, A., Udry, S., and Watson, C. (2019a). K2-291b: A Rocky Super-Earth in a 2.2 day Orbit. *AJ*, 157(3):116.

Kosiarek, M. R. and Crossfield, I. J. M. (2020). Photometry as a Proxy for Stellar Activity in Radial Velocity Analyses. *AJ*, 159(6):271.

Kosiarek, M. R., Crossfield, I. J. M., Hardegree-Ullman, K. K., Livingston, J. H., Benneke, B., Henry, G. W., Howard, W. S., Berardo, D., Blunt, S., Fulton, B. J., Hirsch, L. A., Howard, A. W., Isaacson, H., Petigura, E. A., Sinukoff, E., Weiss, L., Bonfils, X., Dressing, C. D., Knutson, H. A., Schlieder, J. E., Werner, M., Gorjian, V., Krick, J., Morales, F. Y., Astudillo-Defru, N., Almenara, J. M., Delfosse, X., Forveille, T., Lovis, C., Mayor, M., Murgas, F., Pepe, F., Santos, N. C., Udry, S., Corbett, H. T., Fors, O., Law, N. M., Ratzloff, J. K., and del Ser, D. (2019b). Bright Opportunities for Atmospheric Characterization of Small Planets: Masses and Radii of K2-3 b, c, and d and GJ3470 b from Radial Velocity Measurements and Spitzer Transits. *AJ*, 157(3):97.

Kraft, R. P. (1967). Studies of Stellar Rotation. V. The Dependence of Rotation on Age among Solar-Type Stars. *ApJ*, 150:551.

Kreidberg, L. (2015). batman: BAsic Transit Model cAlculatioN in Python. *PASP*, 127:1161.

Kreidberg, L., Mollière, P., Crossfield, I. J. M., Thorngren, D. P., Kawashima, Y., Morley, C. V., Benneke, B., Mikal-Evans, T., Berardo, D., Kosiarek, M., Gorjian, V., Ciardi, D. R., Christiansen, J. L., Dragomir, D., Dressing, C. D., Fortney, J. J., Fulton, B. J., Greene, T. P., Hardegree-Ullman, K. K., Howard, A. W., Howell, S. B., Isaacson, H., Krick, J. E., Livingston, J. H., Lothringer, J. D., Morales, F. Y., Petigura, E. A., Rodriguez, J. E., Schlieder, J. E., and Weiss, L. M. (2020). Tentative Evidence for Water Vapor in the Atmosphere of the Neptune-Size Exoplanet HD 106315 c. *arXiv e-prints*, page arXiv:2006.07444.

Langellier, N., Milbourne, T. W., Phillips, D. F., Haywood, R. D., Saar, S. H., Mortier, A., Malavolta, L., Thompson, S., Collier Cameron, A., Dumusque, X., Cegla, H. M., Latham, D. W., Maldonado, J., Watson, C. A., Cecconi, M., Charbonneau, D., Cosentino, R., Ghedina, A., Gonzalez, M., Li, C.-H., Lodi, M., López-Morales, M., Micela, G., Molinari, E., Pepe, F., Poretti, E., Rice, K., Sasselov, D., Sozzetti, A., Udry, S., and Walsworth, R. L. (2020). Detection Limits of Low-mass, Long-period Exoplanets Using Gaussian Processes Applied to HARPS-N Solar RVs. *arXiv e-prints*, page arXiv:2008.05970.

Law, N. M., Fors, O., Ratzloff, J., Wulfken, P., Kavanaugh, D., Sitar, D. J., Pruett, Z.,

Birchard, M. N., Barlow, B. N., Cannon, K., Cenko, S. B., Dunlap, B., Kraus, A., and Maccarone, T. J. (2015). Evryscope Science: Exploring the Potential of All-Sky Gigapixel-Scale Telescopes. *PASP*, 127:234.

Lawrence, G. M., Rottman, G. J., Kopp, G. A., Harder, J. W., McClintock, W. E., and Woods, T. N. (2000). Total Irradiance Monitor (TIM) for the EOS SORCE mission. In Barnes, W. L., editor, *Earth Observing Systems V*, volume 4135 of *Proc. SPIE*, pages 215–224.

Lendl, M., Ehrenreich, D., Turner, O. D., Bayliss, D., Blanco-Cuaresma, S., Giles, H., Bouchy, F., Marmier, M., and Udry, S. (2017). Ground-based photometry of the 21-day Neptune HD 106315c. *A&A*, 603:L5.

Lopez, E. D. and Fortney, J. J. (2013). The Role of Core Mass in Controlling Evaporation: The Kepler Radius Distribution and the Kepler-36 Density Dichotomy. *ApJ*, 776:2.

Lopez, E. D. and Fortney, J. J. (2014). Understanding the Mass-Radius Relation for Sub-neptunes: Radius as a Proxy for Composition. *ApJ*, 792:1.

Lopez, E. D. and Rice, K. (2018). How formation time-scales affect the period dependence of the transition between rocky super-Earths and gaseous sub-Neptunesand implications for $\eta_{\oplus}$. *MNRAS*, 479(4):5303–5311.

López-Morales, M., Haywood, R. D., Coughlin, J. L., Zeng, L., Buchhave, L. A., Giles, H. A. C., Affer, L., Bonomo, A. S., Charbonneau, D., Collier Cameron, A., Consentino, R., Dressing, C. D., Dumusque, X., Figueira, P., Fiorenzano, A. F. M., Harutyunyan,

A., Johnson, J. A., Latham, D. W., Lopez, E. D., Lovis, C., Malavolta, L., Mayor, M., Micela, G., Molinari, E., Mortier, A., Motalebi, F., Nascimbeni, V., Pepe, F., Phillips, D. F., Piotto, G., Pollacco, D., Queloz, D., Rice, K., Sasselov, D., Segransan, D., Sozzetti, A., Udry, S., Vanderburg, A., and Watson, C. (2016). Kepler-21b: A Rocky Planet Around a V = 8.25 Magnitude Star. *AJ*, 152:204.

Lundkvist, M. S., Kjeldsen, H., Albrecht, S., Davies, G. R., Basu, S., Huber, D., Justesen, A. B., Karoff, C., Silva Aguirre, V., van Eylen, V., Vang, C., Arentoft, T., Barclay, T., Bedding, T. R., Campante, T. L., Chaplin, W. J., Christensen-Dalsgaard, J., Elsworth, Y. P., Gilliland, R. L., Handberg, R., Hekker, S., Kawaler, S. D., Lund, M. N., Metcalfe, T. S., Miglio, A., Rowe, J. F., Stello, D., Tingley, B., and White, T. R. (2016). Hot super-Earths stripped by their host stars. *Nature Communications*, 7:11201.

Luri, X., Brown, A. G. A., Sarro, L. M., Arenou, F., Bailer-Jones, C. A. L., Castro-Ginard, A., de Bruijne, J., Prusti, T., Babusiaux, C., and Delgado, H. E. (2018). Gaia Data Release 2. Using Gaia parallaxes. *A&A*, 616:A9.

Malavolta, L., Mayo, A. W., Louden, T., Rajpaul, V. M., Bonomo, A. S., Buchhave, L. A., Kreidberg, L., Kristiansen, M. H., Lopez-Morales, M., Mortier, A., Vand erburg, A., Coffinet, A., Ehrenreich, D., Lovis, C., Bouchy, F., Charbonneau, D., Ciardi, D. R., Collier Cameron, A., Cosentino, R., Crossfield, I. J. M., Damasso, M., Dressing, C. D., Dumusque, X., Everett, M. E., Figueira, P., Fiorenzano, A. F. M., Gonzales, E. J., Haywood, R. D., Harutyunyan, A., Hirsch, L., Howell, S. B., Johnson, J. A., Latham,

D. W., Lopez, E., Mayor, M., Micela, G., Molinari, E., Nascimbeni, V., Pepe, F., Phillips, D. F., Piotto, G., Rice, K., Sasselov, D., Ségransan, D., Sozzetti, A., Udry, S., and Watson, C. (2018). An Ultra-short Period Rocky Super-Earth with a Secondary Eclipse and a Neptune-like Companion around K2-141. *AJ*, 155(3):107.

Marcy, G. W., Isaacson, H., Howard, A. W., Rowe, J. F., Jenkins, J. M., Bryson, S. T., Latham, D. W., Howell, S. B., Gautier, III, T. N., Batalha, N. M., Rogers, L., Ciardi, D., Fischer, D. A., Gilliland, R. L., Kjeldsen, H., Christensen-Dalsgaard, J., Huber, D., Chaplin, W. J., Basu, S., Buchhave, L. A., Quinn, S. N., Borucki, W. J., Koch, D. G., Hunter, R., Caldwell, D. A., Van Cleve, J., Kolbl, R., Weiss, L. M., Petigura, E., Seager, S., Morton, T., Johnson, J. A., Ballard, S., Burke, C., Cochran, W. D., Endl, M., MacQueen, P., Everett, M. E., Lissauer, J. J., Ford, E. B., Torres, G., Fressin, F., Brown, T. M., Steffen, J. H., Charbonneau, D., Basri, G. S., Sasselov, D. D., Winn, J., Sanchis-Ojeda, R., Christiansen, J., Adams, E., Henze, C., Dupree, A., Fabrycky, D. C., Fortney, J. J., Tarter, J., Holman, M. J., Tenenbaum, P., Shporer, A., Lucas, P. W., Welsh, W. F., Orosz, J. A., Bedding, T. R., Campante, T. L., Davies, G. R., Elsworth, Y., Handberg, R., Hekker, S., Karoff, C., Kawaler, S. D., Lund, M. N., Lundkvist, M., Metcalfe, T. S., Miglio, A., Silva Aguirre, V., Stello, D., White, T. R., Boss, A., Devore, E., Gould, A., Prsa, A., Agol, E., Barclay, T., Coughlin, J., Brugamyer, E., Mullally, F., Quintana, E. V., Still, M., Thompson, S. E., Morrison, D., Twicken, J. D., Désert, J.-M., Carter, J., Crepp, J. R., Hébrard, G., Santerne, A., Moutou, C., Sobeck, C., Hudgins, D., Haas, M. R., Robertson, P., Lillo-Box, J.,

and Barrado, D. (2014). Masses, Radii, and Orbits of Small Kepler Planets: The Transition from Gaseous to Rocky Planets. *ApJS*, 210:20.

Martinez, C. F., Cunha, K., Ghezzi, L., and Smith, V. V. (2019). A Spectroscopic Analysis of the California-Kepler Survey Sample. I. Stellar Parameters, Planetary Radii, and a Slope in the Radius Gap. *ApJ*, 875(1):29.

Mayo, A. W., Rajpaul, V. M., Buchhave, L. A., Dressing, C. D., Mortier, A., Zeng, L., Fortenbach, C. D., Aigrain, S., Bonomo, A. S., Collier Cameron, A., Charbonneau, D., Coffinet, A., Cosentino, R., Damasso, M., Dumusque, X., Martinez Fiorenzano, A. F., Haywood, R. D., Latham, D. W., López-Morales, M., Malavolta, L., Micela, G., Molinari, E., Pearce, L., Pepe, F., Phillips, D., Piotto, G., Poretti, E., Rice, K., Sozzetti, A., and Udry, S. (2019). An 11 Earth-mass, Long-period Sub-Neptune Orbiting a Sun-like Star. *AJ*, 158(4):165.

Mayo, A. W., Vanderburg, A., Latham, D. W., Bieryla, A., Morton, T. D., Buchhave, L. A., Dressing, C. D., Beichman, C., Berlind, P., Calkins, M. L., Ciardi, D. R., Crossfield, I. J. M., Esquerdo, G. A., Everett, M. E., Gonzales, E. J., Hirsch, L. A., Horch, E. P., Howard, A. W., Howell, S. B., Livingston, J., Patel, R., Petigura, E. A., Schlieder, J. E., Scott, N. J., Schumer, C. F., Sinukoff, E., Teske, J., and Winters, J. G. (2018). 275 Candidates and 149 Validated Planets Orbiting Bright Stars in K2 Campaigns 0-10. *AJ*, 155(3):136.

Mayor, M., Pepe, F., Queloz, D., Bouchy, F., Rupprecht, G., Lo Curto, G., Avila, G., Benz, W., Bertaux, J.-L., Bonfils, X., Dall, T., Dekker, H., Delabre, B., Eckert, W.,

Fleury, M., Gilliotte, A., Gojak, D., Guzman, J. C., Kohler, D., Lizon, J.-L., Longinotti, A., Lovis, C., Megevand, D., Pasquini, L., Reyes, J., Sivan, J.-P., Sosnowska, D., Soto, R., Udry, S., van Kesteren, A., Weber, L., and Weilenmann, U. (2003). Setting New Standards with HARPS. *The Messenger*, 114:20–24.

McQuillan, A., Aigrain, S., and Mazeh, T. (2013). Measuring the rotation period distribution of field M dwarfs with Kepler. *MNRAS*, 432:1203–1216.

Mikal-Evans, T., Crossfield, I. J. M., Benneke, B., Kreidberg, L., Moses, J., Morley, C. V., Thorngren, D., Mollière, P., Hardegree-Ullman, K. K., Brewer, J., Christiansen, J. L., Ciardi, D. R., Dragomir, D., Dressing, C., Fortney, J. J., Gorjian, V., Greene, T. P., Hirsch, L. A., Howard, A. W., Howell, S. B., Isaacson, H., Kosiarek, M. R., Krick, J., Livingston, J. H., Lothringer, J. D., Morales, F. Y., Petigura, E. A., Schlieder, J. E., and Werner, M. (2021). Transmission Spectroscopy for the Warm Sub-Neptune HD 3167c: Evidence for Molecular Absorption and a Possible High-metallicity Atmosphere. *AJ*, 161(1):18.

Miller-Ricci, E., Seager, S., and Sasselov, D. (2009). The Atmospheric Signatures of Super-Earths: How to Distinguish Between Hydrogen-Rich and Hydrogen-Poor Atmospheres. *ApJ*, 690(2):1056–1067.

Millholland, S., Laughlin, G., Teske, J., Butler, R. P., Burt, J., Holden, B., Vogt, S., Crane, J., Shectman, S., and Thompson, I. (2018). New Constraints on Gliese 876—Exemplar of Mean-motion Resonance. *AJ*, 155(3):106.

Montet, B. T., Morton, T. D., Foreman-Mackey, D., Johnson, J. A., Hogg, D. W., Bowler, B. P., Latham, D. W., Bieryla, A., and Mann, A. W. (2015). Stellar and Planetary Properties of K2 Campaign 1 Candidates and Validation of 17 Planets, Including a Planet Receiving Earth-like Insolation. *ApJ*, 809:25.

Mortier, A., Bonomo, A. S., Rajpaul, V. M., Buchhave, L. A., Vanderburg, A., Zeng, L., López-Morales, M., Malavolta, L., Collier Cameron, A., Dressing, C. D., Figueira, P., Nascimbeni, V., Rice, K., Sozzetti, A., Watson, C., Affer, L., Bouchy, F., Charbonneau, D., Harutyunyan, A., Haywood, R. D., Johnson, J. A., Latham, D. W., Lovis, C., Martinez Fiorenzano, A. F., Mayor, M., Micela, G., Molinari, E., Motalebi, F., Pepe, F., Piotto, G., Phillips, D., Poretti, E., Sasselov, D., Ségransan, D., and Udry, S. (2018). K2-263 b: a 50 d period sub-Neptune with a mass measurement using HARPS-N. *MNRAS*, 481(2):1839–1847.

Mortier, A. and Collier Cameron, A. (2017). Stacked Bayesian general Lomb-Scargle periodogram: Identifying stellar activity signals. *A&A*, 601:A110.

Nascimbeni, V., Piotto, G., Pagano, I., Scandariato, G., Sani, E., and Fumana, M. (2013). The blue sky of GJ3470b: the atmosphere of a low-mass planet unveiled by ground-based photometry. *A&A*, 559:A32.

Nava, C., López-Morales, M., Haywood, R. D., and Giles, H. A. C. (2019). Exoplanet Imitators: A test of stellar activity behavior in radial velocity signals. *arXiv e-prints*, page arXiv:1911.04106.

Newton, E. R., Irwin, J., Charbonneau, D., Berlind, P., Calkins, M. L., and Mink, J. (2017). The Hα Emission of Nearby M Dwarfs and its Relation to Stellar Rotation. *ApJ*, 834:85.

Newton, E. R., Irwin, J., Charbonneau, D., Berta-Thompson, Z. K., and Dittmann, J. A. (2016). The Impact of Stellar Rotation on the Detectability of Habitable Planets around M Dwarfs. *ApJ*, 821:L19.

Ning, B., Wolfgang, A., and Ghosh, S. (2018). Predicting Exoplanet Masses and Radii: A Nonparametric Approach. *ApJ*, 869(1):5.

Niraula, P., Redfield, S., Dai, F., Barragán, O., Gandolfi, D., Cauley, P. W., Hirano, T., Korth, J., Smith, A. M. S., Prieto-Arranz, J., Grziwa, S., Fridlund, M., Persson, C. M., Justesen, A. B., Winn, J. N., Albrecht, S., Cochran, W. D., Csizmadia, S., Duvvuri, G. M., Endl, M., Hatzes, A. P., Livingston, J. H., Narita, N., Nespral, D., Nowak, G., Pätzold, M., Palle, E., and Van Eylen, V. (2017). Three Super-Earths Transiting the Nearby Star GJ 9827. *AJ*, 154(6):266.

Osborn, H. P., Armstrong, D. J., Adibekyan, V., Collins, K. A., Delgado-Mena, E., Howell, S. B., Hellier, C., King, G. W., Lillo-Box, J., Nielsen, L. D., Otegi, J. F., Santos, N. C., Ziegler, C., Anderson, D. R., Briceño, C., Burke, C., Bayliss, D., Barrado, D., Bryant, E. M., Brown, D. J. A., Barros, S. C. C., Bouchy, F., Caldwell, D. A., Conti, D. M., Díaz, R. F., Dragomir, D., Deleuil, M., Demangeon, O. D. S., Dorn, C., Daylan, T., Figueira, P., Helled, R., Hoyer, S., Jenkins, J. M., Jensen, E. L. N., Latham, D. W., Law, N., Louie, D. R., Mann, A. W., Osborn, A., Pollacco,

D. L., Rodriguez, D. R., Rackham, B. V., Ricker, G., Scott, N. J., Sousa, S. G., Seager, S., Stassun, K. G., Smith, J. C., Strøm, P., Udry, S., Villase nor, J., Vanderspek, R., West, R., Wheatley, P. J., and Winn, J. N. (2021). A hot mini-Neptune in the radius valley orbiting solar analogue HD 110113. *MNRAS*.

Owen, J. E. and Campos Estrada, B. (2019). Testing exoplanet evaporation with multi-transiting systems. *Monthly Notices of the Royal Astronomical Society*, 491(4):5287–5297.

Owen, J. E. and Wu, Y. (2013). Kepler Planets: A Tale of Evaporation. *ApJ*, 775:105.

Owen, J. E. and Wu, Y. (2017). The Evaporation Valley in the Kepler Planets. *ApJ*, 847(1):29.

Pecaut, M. J. and Mamajek, E. E. (2013). Intrinsic Colors, Temperatures, and Bolometric Corrections of Pre-main-sequence Stars. *ApJS*, 208(1):9.

Pepe, F., ESPRESSO Project Team, and Science Team (2019). ESPRESSO At the level of 10 cm/s. In *Extreme Precision in Radial Velocity Conference IV*.

Pepe, F., Mayor, M., Rupprecht, G., Avila, G., Ballester, P., Beckers, J.-L., Benz, W., Bertaux, J.-L., Bouchy, F., Buzzoni, B., Cavadore, C., Deiries, S., Dekker, H., Delabre, B., D'Odorico, S., Eckert, W., Fischer, J., Fleury, M., George, M., Gilliotte, A., Gojak, D., Guzman, J.-C., Koch, F., Kohler, D., Kotzlowski, H., Lacroix, D., Le Merrer, J., Lizon, J.-L., Lo Curto, G., Longinotti, A., Megevand, D., Pasquini, L., Petitpas, P., Pichard, M., Queloz, D., Reyes, J., Richaud, P., Sivan, J.-P., Sosnowska, D., Soto,

R., Udry, S., Ureta, E., van Kesteren, A., Weber, L., Weilenmann, U., Wicenec, A., Wieland, G., Christensen-Dalsgaard, J., Dravins, D., Hatzes, A., Kürster, M., Paresce, F., and Penny, A. (2002). HARPS: ESO's coming planet searcher. Chasing exoplanets with the La Silla 3.6-m telescope. *The Messenger*, 110:9–14.

Pepe, F., Molaro, P., Cristiani, S., Rebolo, R., Santos, N. C., Dekker, H., Mégevand, D., Zerbi, F. M., Cabral, A., Di Marcantonio, P., Abreu, M., Affolter, M., Aliverti, M., Allende Prieto, C., Amate, M., Avila, G., Baldini, V., Bristow, P., Broeg, C., Cirami, R., Coelho, J., Conconi, P., Coretti, I., Cupani, G., D'Odorico, V., De Caprio, V., Delabre, B., Dorn, R., Figueira, P., Fragoso, A., Galeotta, S., Genolet, L., Gomes, R., González Hernández, J. I., Hughes, I., Iwert, O., Kerber, F., Landoni, M., Lizon, J.-L., Lovis, C., Maire, C., Mannetta, M., Martins, C., Monteiro, M., Oliveira, A., Poretti, E., Rasilla, J. L., Riva, M., Santana Tschudi, S., Santos, P., Sosnowska, D., Sousa, S., Spanó, P., Tenegi, F., Toso, G., Vanzella, E., Viel, M., and Zapatero Osorio, M. R. (2014). ESPRESSO: The next European exoplanet hunter. *Astronomische Nachrichten*, 335:8.

Perger, M., Anglada-Escudé, G., Ribas, I., Rosich, A., Herrero, E., and Morales, J. C. (2021). Auto-correlation functions of astrophysical processes, and their relation to Gaussian processes. Application to radial velocities of different starspot configurations. *A&A*, 645:A58.

Perger, M., Ribas, I., Damasso, M., Morales, J. C., Affer, L., Suárez Mascareño, A., Micela, G., Maldonado, J., González Hernández, J. I., Rebolo, R., Scandariato, G.,

Leto, G., Zanmar Sanchez, R., Benatti, S., Bignamini, A., Borsa, F., Carbognani, A., Claudi, R., Desidera, S., Esposito, M., Lafarga, M., Martinez Fiorenzano, A. F., Herrero, E., Molinari, E., Nascimbeni, V., Pagano, I., Pedani, M., Poretti, E., Rainer, M., Rosich, A., Sozzetti, A., and Toledo-Padrón, B. (2017). HADES RV Programme with HARPS-N at TNG. VI. GJ 3942 b behind dominant activity signals. *A&A*, 608:A63.

Persson, C. M., Fridlund, M., Barragán, O., Dai, F., Gandolfi, D., Hatzes, A. P., Hirano, T., Grziwa, S., Korth, J., Prieto-Arranz, J., Fossati, L., Van Eylen, V., Justesen, A. B., Livingston, J., Kubyshkina, D., Deeg, H. J., Guenther, E. W., Nowak, G., Cabrera, J., Eigmüller, P., Csizmadia, S., Smith, A. M. S., Erikson, A., Albrecht, S., Sobrino, A., Cochran, W. D., Endl, M., Esposito, M., Fukui, A., Heeren, P., Hidalgo, D., Hjorth, M., Kuzuhara, M., Narita, N., Nespral, D., Palle, E., Pätzold, M., Rauer, H., Rodler, F., and Winn, J. N. (2018). Super-Earth of 8 $M_{\oplus}$ in a 2.2-day orbit around the K5V star K2-216. *A&A*, 618:A33.

Petersburg, R. R., Joel Ong, J. M., Zhao, L. L., Blackman, R. T., Brewer, J. M., Buchhave, L. A., Cabot, S. H. C., Davis, A. B., Jurgenson, C. A., Leet, C., McCracken, T. M., Sawyer, D., Sharov, M., Tronsgaard, R., Szymkowiak, A. E., and Fischer, D. A. (2020). An Extreme-precision Radial-velocity Pipeline: First Radial Velocities from EXPRES. *AJ*, 159(5):187.

Petigura, E. A. (2015). Prevalence of Earth-size Planets Orbiting Sun-like Stars. *ArXiv e-prints*.

Petigura, E. A., Crossfield, I. J. M., Isaacson, H., Beichman, C. A., Christiansen, J. L., Dressing, C. D., Fulton, B. J., Howard, A. W., Kosiarek, M. R., Lépine, S., Schlieder, J. E., Sinukoff, E., and Yee, S. W. (2018). Planet Candidates from K2 Campaigns 5-8 and Follow-up Optical Spectroscopy. *AJ*, 155:21.

Petigura, E. A., Howard, A. W., and Marcy, G. W. (2013). Prevalence of Earth-size planets orbiting Sun-like stars. *Proceedings of the National Academy of Science*, 110:19273–19278.

Petigura, E. A., Howard, A. W., Marcy, G. W., Johnson, J. A., Isaacson, H., Cargile, P. A., Hebb, L., Fulton, B. J., Weiss, L. M., Morton, T. D., Winn, J. N., Rogers, L. A., Sinukoff, E., Hirsch, L. A., and Crossfield, I. J. M. (2017). The California-Kepler Survey. I. High-resolution Spectroscopy of 1305 Stars Hosting Kepler Transiting Planets. *AJ*, 154(3):107.

Petigura, E. A., Schlieder, J. E., Crossfield, I. J. M., Howard, A. W., Deck, K. M., Ciardi, D. R., Sinukoff, E., Allers, K. N., Best, W. M. J., Liu, M. C., Beichman, C. A., Isaacson, H., Hansen, B. M. S., and Lépine, S. (2015). Two Transiting Earth-size Planets Near Resonance Orbiting a Nearby Cool Star. *ApJ*, 811:102.

Petrovay, K. and van Driel-Gesztelyi, L. (1997). Making Sense of Sunspot Decay. I. Parabolic Decay Law and Gnevyshev-Waldmeier Relation. *Solar Physics*, 176(2):249–266.

Pinamonti, M., Damasso, M., Marzari, F., Sozzetti, A., Desidera, S., Maldonado, J.,

Scandariato, G., Affer, L., Lanza, A. F., Bignamini, A., Bonomo, A. S., Borsa, F., Claudi, R., Cosentino, R., Giacobbe, P., González-Álvarez, E., González Hernández, J. I., Gratton, R., Leto, G., Malavolta, L., Martinez Fiorenzano, A., Micela, G., Molinari, E., Pagano, I., Pedani, M., Perger, M., Piotto, G., Rebolo, R., Ribas, I., Suárez Mascareño, A., and Toledo-Padrón, B. (2018). The HADES RV Programme with HARPS-N at TNG. VIII. GJ15A: a multiple wide planetary system sculpted by binary interaction. *A&A*, 617:A104.

Pinamonti, M., Sozzetti, A., Giacobbe, P., Damasso, M., Scandariato, G., Perger, M., González Hernández, J. I., Lanza, A. F., Maldonado, J., Micela, G., Suárez Mascareño, A., Toledo-Padrón, B., Affer, L., Benatti, S., Bignamini, A., Bonomo, A. S., Claudi, R., Cosentino, R., Desidera, S., Maggio, A., Martinez Fiorenzano, A., Pagano, I., Piotto, G., Rainer, M., Rebolo, R., and Ribas, I. (2019). The HADES RV programme with HARPS-N at TNG. XI. GJ 685 b: a warm super-Earth around an active M dwarf. *A&A*, 625:A126.

Prieto-Arranz, J., Palle, E., Gandolfi, D., Barragán, O., Guenther, E. W., Dai, F., Fridlund, M., Hirano, T., Livingston, J., Luque, R., Niraula, P., Persson, C. M., Redfield, S., Albrecht, S., Alonso, R., Antoniciello, G., Cabrera, J., Cochran, W. D., Csizmadia, S., Deeg, H., Eigmüller, P., Endl, M., Erikson, A., Everett, M. E., Fukui, A., Grziwa, S., Hatzes, A. P., Hidalgo, D., Hjorth, M., Korth, J., Lorenzo-Oliveira, D., Murgas, F., Narita, N., Nespral, D., Nowak, G., Pätzold, M., Montañez Rodríguez, P., Rauer, H., Ribas, I., Smith, A. M. S., Trifonov, T., Van Eylen, V., and Winn,

J. N. (2018). Mass determination of the 1:3:5 near-resonant planets transiting GJ 9827 (K2-135). *A&A*, 618:A116.

Radovan, M. V., Lanclos, K., Holden, B. P., Kibrick, R. I., Allen, S. L., Deich, W. T. S., Rivera, E., Burt, J., Fulton, B., Butler, P., and Vogt, S. S. (2014). The automated planet finder at Lick Observatory. In *Proc. SPIE*, volume 9145 of *Society of Photo-Optical Instrumentation Engineers (SPIE) Conference Series*, page 91452B.

Rajpaul, V., Aigrain, S., Osborne, M. A., Reece, S., and Roberts, S. (2015). A Gaussian process framework for modelling stellar activity signals in radial velocity data. *MNRAS*, 452:2269–2291.

Ramirez Delgado, V. and Dodson-Robinson, S. (2020). Modeling the Quasiperiodic Radial Velocity Variations of γ Draconis. *Research Notes of the American Astronomical Society*, 4(9):153.

Reid, I. N., Hawley, S. L., and Gizis, J. E. (1997). VizieR Online Data Catalog: Palomar/MSU nearby star spectroscopic survey (Hawley+ 1997). *VizieR Online Data Catalog*, 3198.

Rice, K., Malavolta, L., Mayo, A., Mortier, A., Buchhave, L. A., Affer, L., Vanderburg, A., Lopez-Morales, M., Poretti, E., Zeng, L., Collier Cameron, A., Damasso, M., Coffinet, A., Latham, D. W., Bonomo, A. S., Bouchy, F., Charbonneau, D., Dumusque, X., Figueira, P., Martinez Fiorenzano, A. F., Haywood, R. D., Johnson, J. A., Lopez, E., Lovis, C., Mayor, M., Micela, G., Molinari, E., Nascimbeni, V., Nava, C., Pepe, F.,

Phillips, D. F., Piotto, G., Sasselov, D., Ségransan, D., Sozzetti, A., Udry, S., and Watson, C. (2019). Masses and radii for the three super-Earths orbiting GJ 9827, and implications for the composition of small exoplanets. *MNRAS*, 484(3):3731–3745.

Ricker, G. R., Winn, J. N., Vanderspek, R., Latham, D. W., Bakos, G. Á., Bean, J. L., Berta-Thompson, Z. K., Brown, T. M., Buchhave, L., Butler, N. R., Butler, R. P., Chaplin, W. J., Charbonneau, D., Christensen-Dalsgaard, J., Clampin, M., Deming, D., Doty, J., De Lee, N., Dressing, C., Dunham, E. W., Endl, M., Fressin, F., Ge, J., Henning, T., Holman, M. J., Howard, A. W., Ida, S., Jenkins, J., Jernigan, G., Johnson, J. A., Kaltenegger, L., Kawai, N., Kjeldsen, H., Laughlin, G., Levine, A. M., Lin, D., Lissauer, J. J., MacQueen, P., Marcy, G., McCullough, P. R., Morton, T. D., Narita, N., Paegert, M., Palle, E., Pepe, F., Pepper, J., Quirrenbach, A., Rinehart, S. A., Sasselov, D., Sato, B., Seager, S., Sozzetti, A., Stassun, K. G., Sullivan, P., Szentgyorgyi, A., Torres, G., Udry, S., and Villasenor, J. (2014). Transiting Exoplanet Survey Satellite (TESS). In *Space Telescopes and Instrumentation 2014: Optical, Infrared, and Millimeter Wave*, volume 9143 of *Proc. SPIE*, page 914320.

Robertson, P., Endl, M., Cochran, W. D., and Dodson-Robinson, S. E. (2013). Hα Activity of Old M Dwarfs: Stellar Cycles and Mean Activity Levels for 93 Low-mass Stars in the Solar Neighborhood. *ApJ*, 764(1):3.

Robertson, P., Mahadevan, S., Endl, M., and Roy, A. (2014). Stellar activity masquerading as planets in the habitable zone of the M dwarf Gliese 581. *Science*, 345:440–444.

Robertson, P., Roy, A., and Mahadevan, S. (2015). Stellar Activity Mimics a Habitable-zone Planet around Kapteyn's Star. *ApJ*, 805:L22.

Rodriguez, J. E., Vanderburg, A., Eastman, J. D., Mann, A. W., Crossfield, I. J. M., Ciardi, D. R., Latham, D. W., and Quinn, S. N. (2018). A System of Three Super Earths Transiting the Late K-Dwarf GJ 9827 at 30 pc. *AJ*, 155(2):72.

Rodriguez, J. E., Zhou, G., Vanderburg, A., Eastman, J. D., Kreidberg, L., Cargile, P. A., Bieryla, A., Latham, D. W., Irwin, J., Mayo, A. W., Calkins, M. L., Esquerdo, G. A., and Mink, J. (2017). A Multi-planet System Transiting the V = 9 Rapidly Rotating F-Star HD 106315. *AJ*, 153(6):256.

Rogers, J. G. and Owen, J. E. (2021). Unveiling the planet population at birth. *MNRAS*, 503(1):1526–1542.

Rogers, L. A. (2015). Most 1.6 Earth-radius Planets are Not Rocky. *ApJ*, 801:41.

Rogers, L. A. and Seager, S. (2010). A Framework for Quantifying the Degeneracies of Exoplanet Interior Compositions. *ApJ*, 712(2):974–991.

Santerne, A., Brugger, B., Armstrong, D. J., Adibekyan, V., Lillo-Box, J., Gosselin, H., Aguichine, A., Almenara, J. M., Barrado, D., Barros, S. C. C., Bayliss, D., Boisse, I., Bonomo, A. S., Bouchy, F., Brown, D. J. A., Deleuil, M., Delgado Mena, E., Demangeon, O., Díaz, R. F., Doyle, A., Dumusque, X., Faedi, F., Faria, J. P., Figueira, P., Foxell, E., Giles, H., Hébrard, G., Hojjatpanah, S., Hobson, M., Jackman, J., King, G., Kirk, J., Lam, K. W. F., Ligi, R., Lovis, C., Louden, T., McCormac, J., Mousis, O.,

Neal, J. J., Osborn, H. P., Pepe, F., Pollacco, D., Santos, N. C., Sousa, S. G., Udry, S., and Vigan, A. (2018). An Earth-sized exoplanet with a Mercury-like composition. *Nature Astronomy*, 2:393–400.

Schlafly, E. F., Green, G. M., Lang, D., Daylan, T., Finkbeiner, D. P., Lee, A., Meisner, A. M., Schlegel, D., and Valdes, F. (2018). The DECam Plane Survey: Optical Photometry of Two Billion Objects in the Southern Galactic Plane. *ApJS*, 234:39.

Schrijver, C. J. and Zwaan, C. (2000). *Solar and Stellar Magnetic Activity*.

Sing, D. K., Fortney, J. J., Nikolov, N., Wakeford, H. R., Kataria, T., Evans, T. M., Aigrain, S., Ballester, G. E., Burrows, A. S., Deming, D., Désert, J.-M., Gibson, N. P., Henry, G. W., Huitson, C. M., Knutson, H. A., Lecavelier Des Etangs, A., Pont, F., Showman, A. P., Vidal-Madjar, A., Williamson, M. H., and Wilson, P. A. (2016). A continuum from clear to cloudy hot-Jupiter exoplanets without primordial water depletion. *Nature*, 529:59–62.

Skrutskie, M. F., Cutri, R. M., Stiening, R., Weinberg, M. D., Schneider, S., Carpenter, J. M., Beichman, C., Capps, R., Chester, T., Elias, J., Huchra, J., Liebert, J., Lonsdale, C., Monet, D. G., Price, S., Seitzer, P., Jarrett, T., Kirkpatrick, J. D., Gizis, J. E., Howard, E., Evans, T., Fowler, J., Fullmer, L., Hurt, R., Light, R., Kopan, E. L., Marsh, K. A., McCallon, H. L., Tam, R., Van Dyk, S., and Wheelock, S. (2006). The Two Micron All Sky Survey (2MASS). *AJ*, 131:1163–1183.

Stock, S., Kemmer, J., Reffert, S., Trifonov, T., Kaminski, A., Dreizler, S., Quirrenbach,

A., Caballero, J. A., Reiners, A., Jeffers, S. V., Anglada-Escudé, G., Ribas, I., Amado, P. J., Barrado, D., Barnes, J. R., Bauer, F. F., Berdiñas, Z. M., Béjar, V. J. S., Coleman, G. A. L., Cortés-Contreras, M., Díez-Alonso, E., Domínguez-Fernández, A. J., Espinoza, N., Haswell, C. A., Hatzes, A., Henning, T., Jenkins, J. S., Jones, H. R. A., Kossakowski, D., Kürster, M., Lafarga, M., Lee, M. H., López González, M. J., Montes, D., Morales, J. C., Morales, N., Pallé, E., Pedraz, S., Rodríguez, E., Rodríguez-López, C., and Zechmeister, M. (2020). The CARMENES search for exoplanets around M dwarfs. Characterization of the nearby ultra-compact multiplanetary system YZ Ceti. *A&A*, 636:A119.

Suárez Mascareño, A., Faria, J. P., Figueira, P., Lovis, C., Damasso, M., González Hernández, J. I., Rebolo, R., Cristiani, S., Pepe, F., Santos, N. C., Zapatero Osorio, M. R., Adibekyan, V., Hojjatpanah, S., Sozzetti, A., Murgas, F., Abreu, M., Affolter, M., Alibert, Y., Aliverti, M., Allart, R., Allende Prieto, C., Alves, D., Amate, M., Avila, G., Baldini, V., Bandi, T., Barros, S. C. C., Bianco, A., Benz, W., Bouchy, F., Broeng, C., Cabral, A., Calderone, G., Cirami, R., Coelho, J., Conconi, P., Coretti, I., Cumani, C., Cupani, G., D'Odorico, V., Deiries, S., Delabre, B., Di Marcantonio, P., Dumusque, X., Ehrenreich, D., Fragoso, A., Genolet, L., Genoni, M., Génova Santos, R., Hughes, I., Iwert, O., Kerber, F., Knusdstrup, J., Landoni, M., Lavie, B., Lillo-Box, J., Lizon, J., Lo Curto, G., Maire, C., Manescau, A., Martins, C. J. A. P., Mégevand, D., Mehner, A., Micela, G., Modigliani, A., Molaro, P., Monteiro, M. A., Monteiro, M. J. P. F. G., Moschetti, M., Mueller, E., Nunes, N. J., Oggioni, L., Oliveira, A.,

Pallé, E., Pariani, G., Pasquini, L., Poretti, E., Rasilla, J. L., Redaelli, E., Riva, M., Santana Tschudi, S., Santin, P., Santos, P., Segovia, A., Sosnowska, D., Sousa, S., Spanò, P., Tenegi, F., Udry, S., Zanutta, A., and Zerbi, F. (2020). Revisiting Proxima with ESPRESSO. *A&A*, 639:A77.

Sullivan, P. W., Winn, J. N., Berta-Thompson, Z. K., Charbonneau, D., Deming, D., Dressing, C. D., Latham, D. W., Levine, A. M., McCullough, P. R., Morton, T., Ricker, G. R., Vanderspek, R., and Woods, D. (2015). The Transiting Exoplanet Survey Satellite: Simulations of Planet Detections and Astrophysical False Positives. *ApJ*, 809:77.

Tayar, J., Stassun, K. G., and Corsaro, E. (2019). Predicting Granulation "Flicker" and Radial Velocity "Jitter" from Spectroscopic Observables. *ApJ*, 883(2):195.

Telting, J. H., Avila, G., Buchhave, L., Frandsen, S., Gandolfi, D., Lindberg, B., Stempels, H. C., Prins, S., and NOT staff (2014). FIES: The high-resolution Fiber-fed Echelle Spectrograph at the Nordic Optical Telescope. *Astronomische Nachrichten*, 335(1):41.

Teske, J. K., Wang, S., Wolfgang, A., Dai, F., Shectman, S. A., Butler, R. P., Crane, J. D., and Thompson, I. B. (2018). Magellan/PFS Radial Velocities of GJ 9827, a Late K dwarf at 30 pc with Three Transiting Super-Earths. *AJ*, 155(4):148.

Thorngren, D. P. and Fortney, J. J. (2018). Bayesian Analysis of Hot-Jupiter Radius Anomalies: Evidence for Ohmic Dissipation? *AJ*, 155(5):214.

Tsiaras, A., Waldmann, I. P., Zingales, T., Rocchetto, M., Morello, G., Damiano, M.,

Karpouzas, K., Tinetti, G., McKemmish, L. K., Tennyson, J., and Yurchenko, S. N. (2018). A Population Study of Gaseous Exoplanets. *AJ*, 155(4):156.

Usoskin, I. G. (2013). A History of Solar Activity over Millennia. *Living Reviews in Solar Physics*, 10:1.

Valenti, J. A. and Piskunov, N. (2012). SME: Spectroscopy Made Easy. Astrophysics Source Code Library.

van Driel-Gesztelyi, L. and Green, L. M. (2015). Evolution of Active Regions. *Living Reviews in Solar Physics*, 12(1):1.

Van Eylen, V., Agentoft, C., Lundkvist, M. S., Kjeldsen, H., Owen, J. E., Fulton, B. J., Petigura, E., and Snellen, I. (2018). An asteroseismic view of the radius valley: stripped cores, not born rocky. *MNRAS*, 479(4):4786–4795.

Van Grootel, V., Gillon, M., Valencia, D., Madhusudhan, N., Dragomir, D., Howe, A. R., Burrows, A. S., Demory, B.-O., Deming, D., Ehrenreich, D., Lovis, C., Mayor, M., Pepe, F., Queloz, D., Scuflaire, R., Seager, S., Segransan, D., and Udry, S. (2014). Transit Confirmation and Improved Stellar and Planet Parameters for the Super-Earth HD 97658 b and its Host Star. *ApJ*, 786:2.

Vandal, T., Rameau, J., and Doyon, R. (2020). Dynamical Mass Estimates of the β Pictoris Planetary System through Gaussian Process Stellar Activity Modeling. *AJ*, 160(5):243.

Vanderburg, A., Latham, D. W., Buchhave, L. A., Bieryla, A., Berlind, P., Calkins,

M. L., Esquerdo, G. A., Welsh, S., and Johnson, J. A. (2016). Planetary Candidates from the First Year of the K2 Mission. *ApJS*, 222:14.

Venturini, J., Guilera, O. M., Haldemann, J., Ronco, M. P., and Mordasini, C. (2020a). The nature of the radius valley. Hints from formation and evolution models. *A&A*, 643:L1.

Venturini, J., Guilera, O. M., Ronco, M. P., and Mordasini, C. (2020b). Most super-Earths formed by dry pebble accretion are less massive than 5 Earth masses. *A&A*, 644:A174.

Vogt, S. S., Allen, S. L., Bigelow, B. C., Bresee, L., Brown, B., Cantrall, T., Conrad, A., Couture, M., Delaney, C., Epps, H. W., Hilyard, D., Hilyard, D. F., Horn, E., Jern, N., Kanto, D., Keane, M. J., Kibrick, R. I., Lewis, J. W., Osborne, J., Pardeilhan, G. H., Pfister, T., Ricketts, T., Robinson, L. B., Stover, R. J., Tucker, D., Ward, J., and Wei, M. Z. (1994). HIRES: the high-resolution echelle spectrometer on the Keck 10-m Telescope. In Crawford, D. L. and Craine, E. R., editors, *Instrumentation in Astronomy VIII*, volume 2198 of *Proc. SPIE*, page 362.

Vogt, S. S., Penrod, G. D., and Hatzes, A. P. (1987). Doppler Images of Rotating Stars Using Maximum Entropy Image Reconstruction. *ApJ*, 321:496.

Vogt, S. S., Radovan, M., Kibrick, R., Butler, R. P., Alcott, B., Allen, S., Arriagada, P., Bolte, M., Burt, J., Cabak, J., Chloros, K., Cowley, D., Deich, W., Dupraw, B., Earthman, W., Epps, H., Faber, S., Fischer, D., Gates, E., Hilyard, D., Holden, B.,

Johnston, K., Keiser, S., Kanto, D., Katsuki, M., Laiterman, L., Lanclos, K., Laughlin, G., Lewis, J., Lockwood, C., Lynam, P., Marcy, G., McLean, M., Miller, J., Misch, T., Peck, M., Pfister, T., Phillips, A., Rivera, E., Sand ford, D., Saylor, M., Stover, R., Thompson, M., Walp, B., Ward, J., Wareham, J., Wei, M., and Wright, C. (2014). APF—The Lick Observatory Automated Planet Finder. *PASP*, 126(938):359.

Waldmeier, M. (1955). *Ergebnisse und Probleme der Sonnenforschung.*

Weiss, L. M. and Marcy, G. W. (2014). The Mass-Radius Relation for 65 Exoplanets Smaller than 4 Earth Radii. *ApJ*, 783:L6.

Weiss, L. M., Rogers, L. A., Isaacson, H. T., Agol, E., Marcy, G. W., Rowe, J. F., Kipping, D., Fulton, B. J., Lissauer, J. J., Howard, A. W., and Fabrycky, D. (2016). Revised Masses and Densities of the Planets around Kepler-10. *ApJ*, 819:83.

Wolfgang, A. and Lopez, E. (2015). How Rocky Are They? The Composition Distribution of Kepler's Sub-Neptune Planet Candidates within 0.15 AU. *ApJ*, 806:183.

Wright, J. T. (2005). Radial Velocity Jitter in Stars from the California and Carnegie Planet Search at Keck Observatory. *PASP*, 117(833):657–664.

Wu, Y. (2019). Mass and Mass Scalings of Super-Earths. *ApJ*, 874(1):91.

Yee, S. W., Petigura, E. A., and von Braun, K. (2017). Precision Stellar Characterization of FGKM Stars using an Empirical Spectral Library. *ApJ*, 836(1):77.

Yeo, K. L., Krivova, N. A., and Solanki, S. K. (2017). EMPIRE: A robust empirical

reconstruction of solar irradiance variability. *Journal of Geophysical Research (Space Physics)*, 122:3888–3914.

Zeng, L. and Sasselov, D. (2013). A Detailed Model Grid for Solid Planets from 0.1 through 100 Earth Masses. *PASP*, 125(925):227.

Zeng, L., Sasselov, D. D., and Jacobsen, S. B. (2016). Mass-Radius Relation for Rocky Planets Based on PREM. *ApJ*, 819(2):127.

Zhao, L. and The EXPRES Team (2019). The Extreme Precision Spectrograph. In *Extreme Precision in Radial Velocity Conference IV*.

Zhou, G., Rodriguez, J. E., Vanderburg, A., Quinn, S. N., Irwin, J., Huang, C. X., Latham, D. W., Bieryla, A., Esquerdo, G. A., Berlind, P., and Calkins, M. L. (2018). The Warm Neptunes around HD 106315 Have Low Stellar Obliquities. *AJ*, 156(3):93.